Muhammad Sohaib Amjad

Towards Low Latency and Bandwidth Efficient Communication in Wireless Systems

Dissertation

05 May 2021

Please cite as:
Muhammad Sohaib Amjad, “Towards Low Latency and Bandwidth Efficient Communication in Wireless Systems,” PhD Thesis (Dissertation), Institute of Telecommunication Systems, Technische Universität Berlin, Germany, June 2021.

TKN Telecommunication Networks Group

Fachgebiet Telekommunikationsnetze
Technische Universität Berlin, Germany

Einsteinufer 25 · 10587 Berlin · Germany

https://www.tkn.tu-berlin.de/

Towards Low Latency and Bandwidth Efficient Communication in Wireless Systems

vorgelegt von
M.Sc.
Muhammad Sohaib Amjad

an der Fakultät IV – Elektrotechnik und Informatik
der Technischen Universität Berlin
zur Erlangung des akademischen Grades

Doktor der Ingenieurwissenschaften
– Dr.-Ing. –

genehmigte Dissertation

Vorsitzender:	**Prof. Dr.-Ing. habil. Falko Dressler**
Gutachter:	**Prof. Dr.-Ing. habil. Falko Dressler**
	Prof. Dr.-Ing. Dr.-Ing. habil. Robert Weigel
	Prof. Dr. Hsin-Mu (Michael) Tsai

Tag der wissenschaftlichen Aussprache: **05. Mai 2021**

Berlin 2021

Abstract

The densely utilized sub-6 GHz spectrum is reaching critical saturation levels due to the growing number of wirelessly connected devices and their increasing demand for high-speed real-time content access. The ubiquitous connectivity and high data rates in the existing wireless architecture are, therefore, struggling, with both limited link-capacity and channel access. In this regard, infrastructure relays have also been considered for maintaining high-speed wireless connectivity and improved user experience. Nevertheless, due to the existing relaying structure's half-duplex nature, higher latencies are typically experienced, especially in multi-hop scenarios.

To address this issue, in-band Full-Duplex Relaying (FDR) has been proposed in the literature, which is still missing standardized implementations for experimentation and evaluation purposes. The first part of the thesis fills this gap and presents an IEEE 802.11 a/g/p compliant FDR implementation in the GNU Radio framework. We first evaluate FDRs' performance in a dual-hop scenario, with simulations and Software-Defined Radio (SDR)-based real-world experiments. We further consider FDR applicability in vehicular platooning and study its potential in sub-6 GHz and 77 GHz mmWave channels. Our results show that FDR substantially reduces the physical layer latency and transmission power requirements in a multi-hop system, provided that the looped self-interference is sufficiently suppressed.

The second part of this thesis explores the spectrum beyond conventional RF for communications and investigate Visible Light Communication (VLC) as an access technology for bandwidth-efficient and low latency communications. We first present a flexible IEEE 802.11 compliant Vehicular-VLC (V-VLC) system, which utilizes commercial off-the-shelf hardware. Our real-time experiments in the outdoors during the daytime confirm that our system prevents the strong impact of daylight and demonstrates reliable communications for distances beyond 75 m, regardless of the time of the day. We then propose a novel indoor visible light-based communication and non-invasive sensing system with applications in industrial automation and Internet of Things (IoT) solutions. Our results show that integrating the two technologies only marginally lowers individual performance; however, the combined system is especially beneficial in radio-hostile and hazardous industrial environments.

Kurzfassung

Aufgrund der wachsenden Anzahl drahtlos vernetzter Geräte mit immer höheren Anforderungen an schnelle Datenübertragungen ist das 6 GHz-Band mittlerweile stark benutzt und erreicht kritische Auslastungswerte. Bestehende Architekturen sind hier durch eine begrenzte Kanalkapazität und durch Probleme beim gleichzeitigen Kanalzugriff vieler Geräte limitiert. Infrastrukturrelays sind ein vielversprechender Lösungsansatz, um auch weiterhin hohe Datenraten bereitstellen zu können. Vorhandene Technologien basieren allerdings auf Halb-Duplex-Weiterleitung, was zu einer signifikanten Erhöhung der Übertragungslatenz führt, insbesondere in Szenarien mit mehreren Relaisstationen.

Um diesen Nachteil zu beheben, wurde in der Forschungsliteratur sogenanntes in-band Full-Duplex-Relaying (FDR) vorgeschlagen, bei dem der Empfang und die Weiterleitung von drahtlosen Signalen gleichzeitig möglich ist. Es gibt dazu aber noch keine standardisierte Implementierung, mit der dieser Ansatz experimentell getestet und evaluiert werden könnte. Im ersten Teil dieser Arbeit wird daher eine auf dem GNU Radio-Framework basierte Implementierung eines IEEE 802.11 a/g/p konformen Full-Duplex-Relais vorgestellt. Die Leistung dieser FDR-Implementierung wird sowohl simulativ als auch experimentell mit einem Software Defined Radio (SDR) untersucht. Des Weiteren wird die Anwendbarkeit der Technik für Fahrzeug-Platooning im sub-6 GHz-Bereich und auf 77 GHz mmWave-Kanälen gezeigt. Die Ergebnisse zeigen, dass die Übertragungslatenzen und die benötigte Sendeleistung mittels FDR deutlich reduziert werden können.

Der zweite Teil der Arbeit befasst sich mit drahtloser Übertragung jenseits der üblichen Funkfrequenzen. Auch sichtbares Licht kann zur Datenübertragung mit hoher Datenrate und niedriger Latenz genutzt werden (Visible Light Communication (VLC)). In dieser Arbeit stelle ich ein flexibles und IEEE 802.11 kompatibles VLC-System für Fahrzeuge vor, das mit handelsüblicher Standard-Hardware gebaut wurde. Unsere Echtzeit-Experimente im Außenbereich bestätigen, dass dieses System trotz starken Tageslichts eine zuverlässige Kommunikation über Entfernungen von mehr als 75 m ermöglicht. Des Weiteren schlagen wir ein neuartiges, auf sichtbarem Licht basierendes Kommunikations- und nicht-invasives Sensorsystem vor, das in der

Industrieautomation und beim Internet der Dinge (IoT) Anwendung findet. Die Integration von Datenübertragung und berührungsloser Messung führt kaum zu einer Beeinträchtigung der einzelnen Funktionen und ist besonders geeignet für gefährliche Industrieumgebungen, in denen normale Drahtloskommunikation nur eingeschränkt nutzbar ist.

Contents

Chapter 1

Introduction

OVER the last few years, the rapid adoption of proliferating mobile devices such as smartphones, tablets, and wearable for fitness and health; has expanded substantially. Naturally, the end-users are expecting for every such device to be connected with a wireless network at all times – for transferring, viewing/monitoring the recorded data. These new technologies come at the expense of more data, video, and content access in real-time. According to Cisco [1], 70 % of the world's population will have mobile connectivity by the year 2023, with a total number of global mobile subscribers reaching 5.7 billion. A similar mobility report from Ericsson [2] foretasted the global total mobile data traffic to grow by a factor close to five and reach 164EB per month by 2025 from 43 exabytes in 2020.

Clearly, the number of communicating devices supporting wireless connectivity are sky-rocketing, which has certainly fueled insatiable demand for higher data rates. To meet the resultant requirement of surging data rates due to this aggressive growth, efficient utilization of the available bandwidth while maintaining a low latency has become a pivotal objective in developing present-day wireless infrastructure(s). The most obvious solution to maintain these growing volumes of wireless traffic is to increase the wireless link capacity, which can be achieved through technological enhancements. Nevertheless, the sub-6 GHz frequency spectrum, essentially the backbone of existing wireless communications, has already reached the critical saturation level because of smaller available bandwidths. Additionally, even with the employment of highly-efficient modulation and coding schemes, the current sub-6 GHz based wireless systems are approaching Shannon's limit for channel capacity, and further advancements are only bringing marginal improvements [3].

In this regard, the introduction of the Heterogeneous Networks (HetNets) concept, which considers micro and pico- or nano-cell coverage to improve bandwidth reusability, has shown the potential to increase the link capacity and throughput per user. However, this comes at the price of secondary parameters, such as more

equipment and higher latency. As the cell size is reduced, the number of deployed cells increases, which establishes more cell edges where; users typically experience a significant increase in failure rates, lower throughput, and added latency due to frequent handovers.

Alternatively, higher channel capacities can also be achieved by deploying more antennas, i.e., the concept of massive MIMO, or engaging larger bandwidth such as in mmWaves radio spectrum. The realization of massive MIMOs is relatively easy with architectures that are already employing mmWaves communications due to the coexistence of both huge accessible spectrum and small antenna dimensions in the mmWave spectrum, which increases the capacity by many folds. The shorter wavelengths associated with mmWaves reduce the coverage areas, especially in indoor scenarios, which intrinsically support the HetNets architecture. Still, they cannot at all be relied-on for wide-area coverage. The fifth-generation (5G) radio standard, in addition to mmWave communications, therefore requires a sub-6 GHz band for reliable wide-area coverage in order to support connectivity for the Internet of Things (IoT) devices and time-critical communications, such as in automotive applications. The intensely utilized sub-6 GHz spectrum with a rather smaller bandwidth limits the capacity, and spectrum sharing is usually exploited to cope-up with the demand, especially in crowded areas. This results in added latency or reduced capacity, which is certainly not desired in safety-critical vehicular applications, such as vehicle platooning, particularly in dense traffic situations.

1.1 Multi-hop Relaying in Wireless Communication

The ubiquitous nature of the futuristic wireless infrastructures incorporating HetNets, such as in 5G communications, are aimed to support multiplying terminals – capable for human communications and legions of connected machines and things. These terminals/connected objects are structured to passively relay the information for maintaining high-speed connectivity and improved user experience [4]. To collectively address the channel capacity and coverage issues, especially in band-limited wireless links, the infrastructure relays have also gained much attention in recent years. These relay architectures are already proposed to be adopted by wireless standards like 3GPP LTE [5] and IEEE WiMAX [6] as they; can substantially improve the capacity gains and increase the coverage at the same time.

The present relays, however, operate in Half-Duplex (HD) mode, i.e., they can not simultaneously receive and forward the signal. This results in inefficient channel utilization, and additional resources are required for interference-free communication. Essentially, with Time Division Duplexing (TDD)-based relays, additional resources in the time domain are needed, which multiplies the end-to-end latency,

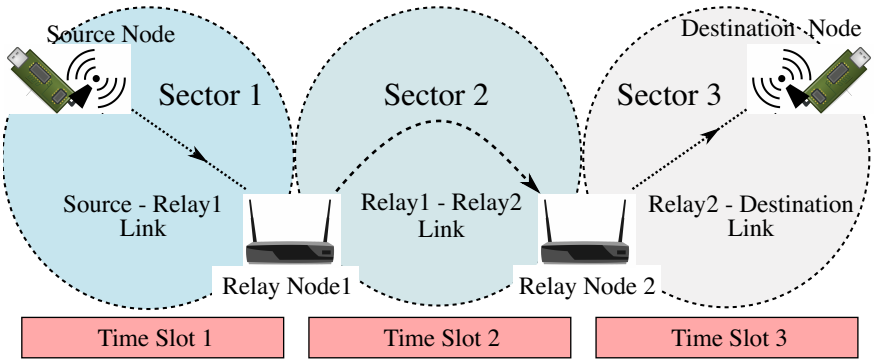

FIGURE 1.1 – Block diagram of a multi-hop transmission link communicating via TDD-based intermediary relaying nodes operating in Half-Duplex mode.

whereas, with Frequency Division Duplex (FDD)-based relays, more resources are required in the frequency domain that incurs spectral losses.

This half-duplex nature of present relaying infrastructures certainly puts a limitation on the efficiency of a network, particularly when the information is relayed (hopped) from source to destination through a larger number of connected things, as illustrated in Figure 1.1. The figure presents a TDD based three-hop relaying network, with two nodes relaying the information from source node to destination node. Now, because of the Half-Duplex Relaying (HDR), in the best case, each node has to wait for at least one-time slot before forwarding the information, and the overall network requires three-time slots just for one-way communication, i.e., from source to destination. This increases the end-to-end latency of the network, which only grows in the case of more relaying nodes or; in the presence of a large number of information sending devices. Hence, both coverage and capacity can certainly be improved but at the expense of higher end-to-end network latencies.

In the last decade, in-band Full-Duplex (FD) wireless communication has attracted significant attention, and a considerable amount of research has been done in this domain [7]. The recent advances in signal processing capabilities and antenna technologies have played a pivotal role in enabling in-band full-duplex wireless transmissions. Different solutions, implementations, and architectures have been proposed, e.g., in [8]–[11], to address the foremost factor impeding in-band FD communications, i.e., the Self-Interference (SI), which intrinsically exists due to radio's own transmissions at the same time and frequency. The capacity of a full-duplex radio to transmit and receive simultaneously primarily helps in recuperating the spectral losses and improving the effective channel utilization of classical half-duplex systems. Additionally, it mitigates the existing hidden terminal problem [12]

and supports primary user detection in cognitive radio, i.e., spectrum sensing for opportunistic spectrum usage [13].

Besides the mentioned advantages, full-duplex communication in relaying can also play a critical role in efficient bandwidth utilization and reducing the end-to-end latency of a multi-hop relay network while offering extended coverage and improved capacity gain at the same time. This can essentially be helpful in multi-hop latency-critical applications such as road traffic platooning, where a leading vehicle coordinates with its followers for effective road utilization and fuel-efficient driving [14]–[16]. The ability of in-band full-duplex relays to simultaneously receive and forward greatly reduces the latency of a multi-hop network, with least channel utilization, i.e., minimum channel engagement by the relaying devices. Additionally, Full-Duplex Relaying (FDR) deployment topologies in different centralized and distributed fashions can further reduce the management complexities and allow efficient spectrum utilization and offload capabilities. Nevertheless, for optimal performance, the suppression of Looped Self-Interference (LSI) (due to simultaneous reception and forwarding) to the receiver's noise floor is crucial in an FDR system. Any residual LSI predominantly worsens the noise floor for the Signal-of-Interest (SoI) arriving from a distant source, resulting in degraded Signal-to-Noise Ratio (SNR) that eventually limits the overall performance.

1.2 Access Technologies for Wireless Communication

In addition to Radio Frequency (RF) communications, complementary technologies such as Visible Light Communication (VLC) in particular has emerged as a potential technology to complement conventional RF-based wireless communications. The present RF technologies in sub-6 GHz primarily support relatively long communication distances, penetrate through objects, and are well matured in terms of optimized performance. Nevertheless, the available radio spectrum limitation and the channel congestion level in medium-to-high density scenarios so far are capping the scalability of RF-based solutions. In this respect, VLC as a complementary technology has gained the interest of both the industry and research community within the last decade, and the literature in the field has grown exponentially [17]–[19].

The fast switching capability of the Light Emitting Diodes (LEDs) has primarily founded the basis for the present-day VLC. A lot of efforts are underway for the standardization of VLC by IEEE [20] and Japan Electronics and Information Technology Industries Association (JEITA) [21]. Meanwhile, companies like Philips Lighting technologies and pureLiFi are already offering VLC supporting front-ends, typically for indoor applications, and they are easily available (in the markets). From the perspective of potential applications, VLC can be utilized for both indoor and

outdoor solutions. Indoor VLC so far has attracted the most attention and growth, which is essentially fueled by the success of the LiFi concept [22]. Outdoor VLC, on the other hand, has advanced at a relatively slower pace, primarily because of more challenging environments and other constraints (such as mobility, daylight, weather, regulations), yet with substantial results.

Today, Intelligent Transportation Systems (ITS) are one of the most promising applications of outdoor VLC. With the rapid adoption of LED-based lighting modules in the automotive industry, VLC is considered as an access technology for ITS. Specifically, for time-crucial vehicular networking applications, the readily available high-power head and tail lights can be economically modified for bidirectional communication purposes [23]. A conjunction of these two technologies, i.e., RF and VLC, can certainly support efficient spectrum usage, renders low latency, and offers improved reliability as well.

As for the indoor VLC applications, the complementary technology can further be integrated with IoT for novel networking solutions [24]. The Line-of-Sight (LoS) communication requirement of VLC supports high-precision indoor positioning, which opens up a wide range of IoT applications [25]. With the proliferating LED usage in indoors, high-density wireless *downlinks* for a large number of IoT elements are now realizable, which can reduce the traffic on the RF communication spectrum [26]. Additionally, VLC can improve communication reliability by complementing RF-based communication systems, especially in safety-critical and radio-hostile industrial environments. Furthermore, visible light has been demonstrated for sensing applications in addition to its predominant utilization for communication purposes. Roy et al. [27], [28] proposed a vision-based approach that uses a strobing light source and a cheap commodity low-Frames Per Second (FPS) camera for the estimation of an object's vibration frequency unobtrusively. This non-invasive vibrations sensing potential of visible light can essentially be used in industrial environments as the first indicator of potential breakdowns/failures of machines and can be integrated with VLC for industrial-automation and IoT applications.

1.3 Structure of the Thesis

Within the scope of this Ph.D. dissertation, we are exploring techniques that contribute towards reduced end-to-end latency and bandwidth-efficient wireless communications. This research study is designed to first provide analytical findings and a form numerical basis for the targeted "low latency and bandwidth-efficient" performance metrics. Later, we present the real-time system-level evaluation from a physical layer perspective in simulations and with Software-Defined Radio (SDR)-based experiments.

The organization of the rest of the thesis is as follows. Chapter 2 covers the fundamentals of Radio Frequency (RF) communication and Visible Light Communication (VLC). Moving onward, the thesis is divided into two parts:

The first part of this study, which includes Chapters 3 & 4, primarily focuses on the infrastructure relays in RF-based wireless systems. It targets the shortcomings of the existing half-duplex based multi-hop relaying. As previously discussed, the multi-hop relaying can extend the link-capacity and wireless coverage but at the expense of increased end-to-end latency and poor spectral usage/channel utilization. With the capacity to simultaneously receive and forward, in-band full-duplex relaying has the potential to overcome these limitations of traditional relaying infrastructures. In Chapter 3, we, therefore, present the in-depth study on dual-hop in-band full-duplex relaying with extensive analytical, simulative, and real-world experimental evaluation. The chapter analytically compares the end-to-end SNR and capacity gain of HDR with FDR while considering the Looped Self-Interference (LSI). It also studies in detail the real-time simulative evaluation of our IEEE 802.11a/g/p compliant GNU Radio-based implementation of Amplify and Forward (AF) and Decode and Forward (DF) relaying schemes in HD mode and; in FD mode under LSI. It additionally reports the real-time system-level evaluation of our standard-compliant implementation via SDRs and outlines; the performance of both HD and FD based relaying systems through SDR-based experiments in indoor environments. Chapter 4 further extends the concept of dual-hop full-duplex relaying into multi-hop relaying for latency-critical application scenario of vehicle platooning and presents our detailed findings on full-duplex multi-hop relaying performance in both sub-6 GHz microwave and 77 GHz mmWave channels.

The second part of this thesis investigates Visible Light Communication as a complementary technology to existing RF communications and includes Chapters 5 & 6. It covers Visible Light Communication (VLC) as a viable access technology for bandwidth-efficient communications in both outdoors and indoors. A free, unlicensed visible light spectrum for wireless communications eases-up the bandwidth struggle in the densely populated sub-6 GHz spectrum, which indirectly solves the channel access and the resultant raising latency issues. From the outdoor VLC perspective, Chapter 5 specifically looks into vehicular communication, i.e., Vehicular-VLC (V-VLC), and explores the possibilities of V-VLC, even in broad daylight with commercially available off-the-shelf hardware. The chapter extends with an IEEE 802.11p compliant system-level implementation supporting SDR-based real-world experiments for evaluation purposes – in a sophisticated lab environment, then in an indoor parking lot, and finally outdoors, under different light conditions. Chapter 6 explores indoor VLC together with the sensing potential of visible light in industrial-IoTs and -automation applications, especially in RF-hostile or RF-populated environments. It first studies

the joint Visible Light Communication and Sensing (VLCS) system analytically and then rigorously evaluates the complete system via real-time simulation experiments.

1.4 Summarizing the Contributions

Having described the research scope of this Ph.D. undertaking, we now present the main contributions of this thesis.

As the first contribution of this Ph.D. thesis, we present the implementation of the GNU Radio-based in-band full-duplex relay system, with a novel core module to suppress the looped-back self-inference in real-time for both simulative and Software-Defined Radio (SDR)-based experimental evaluation. To the best of our knowledge, this is the first work that evaluates the performance of FD relaying via real-world experiments using a General Purpose Processor (GPP)-based software implementation adhering to the IEEE 802.11a/g/p standard for WLAN. Our results show the potential of FDR to substantially reduce the end-to-end physical layer latency in a dual-hop wireless system, provided that the LSI is suppressed close to the noise floor. Additionally, between the two widely adopted relaying strategies, i.e., Amplify and Forward (AF) and Decode and Forward (DF) relays, the DF-based FDR materializes as most viable and outperforms all other relaying strategies.

As the second contribution, we take advantage of the receive and forward (without waiting) capability of in-band full-duplex relaying and, for the first time, use it for vehicular communication, specifically in platooning applications. For a five-vehicle platoon scenario, we show an end-to-end physical layer latency reduction by 6 times with FDR as compared to its HDR counterpart. We explore the potential of Full-Duplex Relaying for both sub-6 GHz channel and 77 GHz mmWave channel where; FDR appears to be more effective in mmWave channel certainly because of its high propagation losses, which as a result offer large passive isolation of the Looped Self-Interference, to begin with.

As the third contribution, we present a flexible Vehicular-VLC system, which utilizes Commercial Off-The-Shelf (COTS) hardware, and supports outdoor distances beyond 75 m for wireless communication, even in broad daylight. The implementation incorporates a variety of Modulation and Coding Scheme (MCS), and it is fully compliant with IEEE 802.11 standards. With the help of extensive outdoor measurement campaigns, we explore the performance of our system under different lighting conditions and show the potentials of V-VLC technology to complement the overly crowded radio frequency spectrum.

As the fourth and final contribution of this Ph.D. thesis, we propose a novel visible light-based system for joint communications and non-invasive vibration sensing – to sense and communicate the health of structures and machines in industrial-IoT

applications. We show the VLCS system' potential to complement the RF spectrum by communicating wirelessly over several meters, which is especially interesting and viable in IoT networks. We further utilize the dark-period of LEDs in the VLCS system to improve communication throughput and, at the same time, investigate its impact on the frequency sensing capacity. We additionally employ preamble-less communication to reduce the packet size, which makes the communication more energy efficient.

1.5 Publications

The research results derived during this Ph.D. study have been published in scientific journals and presented in various international conferences. This section lists the peer-reviewed publications which I have worked on during my Ph.D. thesis.

Publications This Thesis is Based On

Specifically, this thesis is based on the technical content presented in the following publications:

- **M. S. Amjad and F. Dressler, "Experimental Insights on Software-based Real-Time SI Cancellation for In-Band Full Duplex DF Relays," in *IEEE International Conference on Communications (ICC 2019)*, Shanghai, China: IEEE, May 2019.**

  In this conference paper, my contributions were: the first Orthogonal Frequency Division Multiplexing (OFDM)-based Decode and Forward-FDR implementation in GNU Radio, with real-time LSI cancellation monitoring with SDR; the investigation of residual LSI impact on FDR performance and throughput, which increased by two folds when LSI is fully suppressed.

- **M. S. Amjad and F. Dressler, "Software-based Real-time Full-duplex Relaying: An Experimental Study," *IEEE Transactions on Green Communications and Networking (TGCN)*, vol. 4, no. 3, pp. 647–656, Sep. 2020.**

  This Journal article is the extension of my previous paper, additionally focused on: studying LSI impact due to estimation error, both analytically and in real-time simulation environment; channel capacity gain of FDR over HDR; comparison of experimentally obtained results with the simulative and analytical findings.

- **M. S. Amjad and F. Dressler, "Performance Insights on IEEE 802.11a/g Compliant Software-based In-Band Full Duplex Relay Systems," in *IEEE***

***Wireless Communications and Networking Conference (WCNC 2019)*, Marrakesh, Morocco: IEEE, Apr. 2019.**

In this conference paper, my contributions were: the analytical modeling of full-duplex relaying techniques, with closed-form expressions for numerical analysis; implementation of an FDR system that includes a novel core module for LSI cancellation in GNU Radio framework; evaluation and comparison of the IEEE 802.11a/g compliant HDR with FDR systems via an extensive-set of performance results for frequency-selective Rayleigh fading channels in simulations.

- **M. S. Amjad and F. Dressler, "Software-based In-Band Full Duplex Relays for IEEE 802.11a/g/p: An Experimental Study," in *IEEE Wireless Communications and Networking Conference (WCNC 2021)*, Nanjing, China: IEEE, Mar. 2021.**

  This conference submission is the extension of my previous paper, additionally focused on: improving the LSI suppression module of our preliminary implementation of FDR system in GNU Radio, which additionally estimates sampling offset for improved digital domain cancellation of LSI; evaluating the performance of an IEEE 802.11a/g/p compliant FDR system in real-time SDR-based experiments for both LoS and Nonline-of-Sight (NLoS) cases in an indoor environment.

- **M. S. Amjad, T. Hardes, M. Schettler, C. Sommer, and F. Dressler, "Using Full Duplex Relaying to Reduce Physical Layer Latency in Platooning," in *11th IEEE Vehicular Networking Conference (VNC 2019)*, Los Angeles, CA: IEEE, Dec. 2019, pp. 236–239.**

  In this conference paper, my contributions were: to show the feasibility of full-duplex relaying in vehicular networking applications such as platooning in sub-6 GHz communication band; implementation of FDR in vehicle platooning scenario; real-time simulative evaluation of communication performance in all scenarios, i.e., HDR, FDR, and Direct Transmission (DT).

- **M. S. Amjad, M. Schettler, S. Dimce, and F. Dressler, "Inband Full-Duplex Relaying for RADCOM-based Cooperative Driving," in *12th IEEE Vehicular Networking Conference (VNC 2020)*, Virtual Conference: IEEE, Dec. 2020.**

  This conference paper extends the previous work with the following contributions: the first investigative study on RADCOM-based FDR in cooperative driving networks with platooning as a particular use case; the emulation of 77 GHz mmWave channel in GNU Radio framework implementing the platoon-

ing scenario; the evaluation and comparison of RADCOM FDR performance over HDR in vehicular platoons.

- **M. S. Amjad, C. Tebruegge, A. Memedi, S. Kruse, C. Kress, C. Scheytt, and F. Dressler, "An IEEE 802.11 Compliant SDR-based System for Vehicular Visible Light Communications," in *IEEE International Conference on Communications (ICC 2019)*, Shanghai, China: IEEE, May 2019.**

  In this conference paper, my contributions were: the Tx/Rx baseband signal processing implementation in the GNU Radio framework and its integration with COTS hardware; real-time physical layer performance evaluation of the presented IEEE 802.11 compliant Vehicular-VLC prototype, and the analysis of clocking offsets between transmitter and receiver.

- **M. S. Amjad, C. Tebruegge, A. Memedi, S. Kruse, C. Kress, C. Scheytt, and F. Dressler, "Towards an IEEE 802.11 Compliant System for Outdoor Vehicular Visible Light Communications," *IEEE Transactions on Vehicular Technology (TVT)*, 2021, to appear.** DOI: **10.1109/TVT.2021.3075301.**

  This Journal article is the extension of my previous paper, additionally focused on: GNU Radio-based implementation for outdoor V-VLC, which utilizes a high-power LED headlight to supports communication even in broad daylight; the investigation on limited communication bandwidth due to the low pass behavior of COTS devices, driving the performance bottlenecks in V-VLC system; the impact of optics alignment on the receiver's performance and using an external clock to remove the clocking offsets.

- **M. Nabeel, M. S. Amjad, and F. Dressler, "Preamble-Less Diversity Combining: Improved Energy-Efficiency in Sensor Networks," in *IEEE Global Communications Conference (GLOBECOM 2018)*, Abu Dhabi, United Arab Emirates: IEEE, Dec. 2018.**

  In this conference paper, my contributions were: the successful integration of the preamble-less communication with the receive diversity in a distributed antenna system; implementation of the complete system in GNU Radio framework; extensive real-time simulative and experimental evaluation with SDRs supporting the concept, the achievable performance gain, and possible energy conservation.

- **M. S. Amjad and F. Dressler, "Integrated Communications and Non-Invasive Vibrations Sensing using Strobing Light," in *IEEE International Conference on Communications (ICC 2020)*, Virtual Conference: IEEE, Jun. 2020.**

In this conference paper, my contributions were: the analytical study of the proposed novel idea of the integrated system for simultaneous communications and non-invasive vibrations sensing for potential fault/failure detection; the simulative evaluation of both communication and sensing performance; exploring the spatial diversity techniques for improved performance.

- **M. S. Amjad and F. Dressler, "Using Visible Light for Joint Communications and Vibration Sensing in Industrial IoT Applications," in *IEEE International Conference on Communications (ICC 2021)*, to appear, Montreal Canada: IEEE, 2021.**

  This conference paper extended the previous work with the following contributions: the evaluation of the VLCS system as a potential candidate for industrial IoT applications, performing communications and vibrations sensing for structural health monitoring; the utilization of dark-period of the LEDs to further improve the communication throughput; the comparison of joint VLCS system with the individual VLC and Visible Light Sensing (VLS) systems for performance evaluation.

Additional Publications

During my studies, I also co-authored the following publication:

- **M. S. Amjad, G. S. Pannu, A. Memedi, M. Nabeel, J. Blobel, F. Missbrenner, and F. Dressler, "A Flexible Real-Time Software-based Multi-Band Channel Sounder," in *31st IEEE Annual International Symposium on Personal, Indoor and Mobile Radio Communications (PIMRC 2020)*, Virtual Conference: IEEE, Aug. 2020.**

- **M. S. Amjad, H. Nawaz, K. Ozsoy, O. Gurbuz, and I. Tekin, "A Low-Complexity Full-Duplex Radio Implementation With a Single Antenna," *IEEE Transactions on Vehicular Technology (TVT)*, vol. 67, no. 3, pp. 2206–2218, Mar. 2018.**

- **S. Kruse, C. Kress, A. Memedi, C. Tebruegge, M. S. Amjad, C. Scheytt, and F. Dressler, "Design of an Automotive Visible Light Communications Link using an Off-The-Shelf LED Headlight," in *16th GMM/ITG-Symposium ANALOG 2018*, Munich, Germany: VDE, Sep. 2018.**

- **J. Koepe, C. Kaltschmidt, M. Illian, R. Puknat, P. Kneuper, S. Wittemeier, A. Memedi, C. Tebruegge, M. S. Amjad, S. Kruse, C. Kress, C. Scheytt, and F. Dressler, "First Performance Insights on Our Novel OFDM-based Vehicular VLC Prototype," in *10th IEEE Vehicular Networking Conference (VNC 2018), Poster Session*, Taipei, Taiwan: IEEE, Dec. 2018.**

Chapter 2

Fundamentals of Wireless Communications

The first wireless communication occurred in 1880 when Alexander Graham Bell and Charles Sumner Tainter performed wireless conversation via the photophone [44]. The telephone utilized a beam of light to send an audio signal; at that time, it did not seem viable, but today, this principle is the basis for optical communications. Radio communications originated in the late eighteenth century when in 1894, Marconi demonstrated the first long-range radio transmissions over 18 miles between a boat and Isle of Wight in the English Channel [45]. What fascinated the people most was the possibility to communicate without a physical connection. The obvious advantage at that time; was the broadcast nature of the channel, which soon after was utilized for widespread radio and television broadcasting.

Wireless communication revolutionized at the beginning of the 1990s, with the advent of digital communications and wireless networks driven by advances in radio frequency (RF) and microwave engineering, resulting in a social revolution and a paradigm shift from wired to wireless technology [45]. With time, wireless technology evolved rapidly; and within the century, it advanced from basic unidirectional broadcast communications to cellular networks and Wireless Local Area Network (WLAN) for global wireless internet connectivity. In the present era, there are different air interfaces for wireless communications such as Radio Frequency (RF), Optical, and sonic.

2.1 Radio Frequency (RF) Communications

The RF-based wireless communication utilizes radio frequencies for information transfer between two points in space without a physical connection. Radio waves are electromagnetic radiation with particular RF frequencies in the range of 3 kHz

to 300 GHz, and they propagate at the speed of light. In the modern era, RF-based wireless communication is utilized in almost everything, applications ranging in Industries, Medical, Military, Telecom sector, and many more.

The radio waves, while propagating, experience reflection, diffraction, scattering, and even absorption phenomenons, typically from nearby infrastructures and other elements. These phenomenons are mainly responsible for shadowing and multi-path fading in wireless communication, except for absorption, which causes severe propagation attenuation and; it is primarily observed with mmWaves, where the wavelengths are extremely small. Most of the commercial RF-based wireless communication systems are mainly categorized into Sub-6 GHz systems that are feasible for reliable and long-distance communication but have smaller capacities because of smaller available bandwidths and overly crowded spectrum; and the mmWaves systems which support very high data rates because of large available bandwidth, but works only for very short-range communications which can be leveraged for a much better frequency reuse-ability factor.

Almost all the existing RF-based state-of-the-art wireless technologies operate in HD communication mode. An HD radio either requires two time-slots or two frequency channels (one for uplink and downlink each) for reliable and interference-free communication. If the radio operates in Time Division Duplexing (TDD) mode, it needs two time-slots per user for two way communications, whereas, if it operates in Frequency Division Duplex (FDD) mode, it requires two frequency channels as uplink and downlink for decode-able communications. In either mode, additional resources are required, which makes the communication systems temporally or spectrally inefficient. With a significant expansion in demand for high-speed wireless connectivity among end-users, this inefficient resource utilization needed to be addressed, which gave birth to the idea of *in-band full-duplex wireless communications*.

2.1.1 In-band Full-Duplex Wireless Communications

A radio that can perform a bidirectional communication simultaneously at the same time and frequency is classified as full-duplex radio.

2.1.1.1 Problem Statement

Before the last decade or so, the very concept of FD wireless communication was thought to be impossible. As a result, all the designed wireless systems operated in an HD transmission mode that required different resources in time or frequency. The primary obstacle that impedes FD realization is the coupled SI signal that is present at the receiver of an FD radio because of the simultaneous reception of its own transmission. This coupled SI signal can be over a million times stronger than the SoI arriving from a distant transmitter and can consume the whole dynamic

range of the Analog-to-Digital Converter (ADC) at the receiver. This leads to the receiver's saturation, which makes the processing of the SoI impossible. Nevertheless, the implication of FD communications, i.e., the potential to instantly reduce the spectral or temporal requirements by half because of simultaneous transmission and reception, is very alluring. This is precisely the reason which kept the scientists and researchers; to further explore various ideas and techniques to mitigate this strong SI signal.

For a radio, to enable FD transmissions, complete suppression of the SI signal to the receiver's noise floor is the fundamental requirement. To comprehend the degree of SI suppression requirements, let us consider the state-of-the-art WiFi technology, where the average transmission power is 20 dBm, and a receiver noise floor around -90 dBm [8]. Therefore, to enable FD communications with the technology, the radio's self transmissions must be suppressed down to the noise floor, i.e., 20 dBm $-$ (-90 dBm) $=$ 110 dB. Hence, total suppression of 110 dB is required to achieve FD communications for WiFi technology. Now, let us assume that the system fails to meet this suppression requirement by 20 dB, then this leftover 20 dB signal is referred to as residual SI, which is nothing but a raised noise floor for the SoI. This essentially means that the new noise floor for the SoI is -70 dBm instead of the inherent -90 dBm. For an SoI with -60 dBm strength, the received SNR will drop from 30 dB (-60 dBm $-$ (-90 dBm) $=$ 30 dB, half duplex case), to 10 dB (-60 dBm $-$ (-70 dBm) $=$ 10 dB) in the case of FD communications. The above example clearly reflects the crucial requirement of SI suppression to the receiver's noise floor, which, if not achieved, can greatly reduce the overall system performance.

2.1.1.2 Self-Interference (SI) Suppression

Research works such as [8], [9], [46]–[54] have presented various architectures and techniques to suppress the SI signal in order to enable FD communications. The basis for SI mitigation is that in any FD communication system, the received SI at a transceiver is actually a distorted copy of the self transmissions and since these transmissions are already known; therefore, it is possible to remove them at the receiving side. The proposed SI mitigation approaches in the literature are categorized into passive suppression and active cancellation stages. In order to achieve maximum SI cancellation, incorporation of both is typically required.

Passive Suppression

The passive suppression stage isolates the SI signal in the propagation-domain, i.e., before the receiving path. Some of the proposed approaches for passive suppression [49], [51], [53] include isolation of transmitting and receiving antenna by adopting orthogonal polarization or cross-polarization, electromagnetic isolation of

transmitting and receiving antenna using RF absorbers, by adjusting the antenna directivity and position, and employing a three-port circulator isolating the transmit and receive ports.

Active Cancellation

The active cancellation stage typically employs different processing approaches on the known transmitted signal to approximate the SI and then cancel it by subtracting the two, i.e., the received and the approximated SI. Active cancellation is further performed in two stages: analog domain cancellation and digital domain cancellation.

The analog cancellation is performed before the ADC in a receiver chain. It is designed to mitigate the SI signal to a degree that the aggregated received signal (SI + SoI) does not consume the complete ADC's dynamic range. It is typically achieved through analog cancellation boards [8]. The board is designed to tap the transmission chain and obtain a small copy of the transmitted signal before the RF front-end. The advantage of using such boards is that the tapped signal also contains the noise and the nonlinearities introduced by the transmitting chain elements, such as oscillator and power amplifier, which assist in better SI cancellation.

After analog cancellation, the residual SI, which includes the multipath SI components as well, is then removed in the digital cancellation. The digital domain cancellation of the SI signal is realized at the baseband level. To model the wireless channel impairments that basically distort SI signal, the digital domain utilizes the preamble of the received SI and performs signal processing techniques [8], [9], [47], [55] to estimate the SI channel. Once the SI channel is modeled, the known transmitted samples are filtered through the modeled channel to approximate the residual SI signal, which is then subtracted from the actual residual SI. There are other techniques for digital domain cancellation that utilize an ancillary RF chain [9], [56] to produce an antidote signal to mitigate SI.

2.1.2 Orthogonal Frequency Division Multiplexing (OFDM)

OFDM is a multicarrier wideband modulation technique, which is an integral part of several state-of-the-art wireless communication technologies. OFDM is designed to divide the available bandwidth into multiple narrowband partially overlapping subcarriers instead of a single wideband carrier. The classical signal-carrier based systems experience performance challenges, especially when contended for higher capacity. The Shannon's theorem for channel capacity $'C'$ clearly stated the dependence of higher throughput on bandwidth $'B'$ and SNR γ. as

$$C = B\log_2(\gamma + 1). \tag{2.1}$$

With today's highly sophisticated MCS, optimal spectral efficiency close to the capacity bounds has already been achieved; nevertheless, higher bandwidths are still required for further capacity gains. This approach does not scale well for single carrier-based systems, translating onto a higher symbol rate. This essentially means that in the event when signal bandwidth exceeds the channel coherence bandwidth, the receiver is deemed to apply complex estimation approaches [57], [58].

OFDM comprises multiple narrowband subcarriers; this allows a fair trade-off between more subcarriers meaning longer symbol times or fewer subcarriers with shorter symbol times. Essentially, if the channel's coherence bandwidth is small, narrower subcarriers can be utilized; on the other hand, if coherence time is brief, shorter symbols can be used. With a successful realization of the above condition, a single-tap equalizer per subcarrier is sufficient for the equalization process, which substantially simplifies the receiver design [57]. This flexibility to adapt the PHY-layer according to the channel conditions certainly helps overcome the limitation of traditional single-carrier systems, and perhaps, it is one of the biggest advantages of OFDM.

From the spectrum sharing perspective, OFDM has a significant benefit over single-carrier systems as they required a larger guard band between the carriers to prevent the leakage of one signal carrier into the other. In OFDM, the subcarrier frequencies are realized such that; they are orthogonal to one another and have minimum spacing. Although the spectra of an individual subcarrier overlap with other subcarriers, it does not interfere with other subcarriers because of the orthogonality principle, i.e., the impact of an individual subcarrier is zero at the center frequencies of adjacent subcarriers. This orthogonality principle (allowing minimum subcarrier spacing) is the primary rationale for achieving high spectral efficiency with OFDM. This additionally supports the scalability of OFDM towards higher bandwidths, i.e., simply adding more subcarriers. The different IEEE 802.11 releases for WLAN are great examples here, as each release support multiple channel bandwidths that only differ in the number of subcarriers.

In all fairness, OFDM has its drawbacks as well. Unlike single carrier systems, OFDM suffers greatly from high Peak-to-Average Power Ratios (PAPRs). With OFDM, the contribution of different subcarriers having furthest constellation points occasionally adds up in the time-domain samples, which creates peaks that can easily drive the power amplifier into saturation. To address this issue, the low average power is adopted from the transmitter side (to avoid saturation) or tolerate nonlinear behavior. In any case, OFDM requires linear amplifiers with sufficient dynamic ranges. Additionally, OFDM needs a guard interval between successive symbols that prevents the leakage of the current symbol into the useful symbol time of the successive symbol. If not prevented, this leakage introduces Inter-Symbol-Interference (ISI), which severely degrades the performance of OFDM. To avoid ISI, a guard interval

is appended at the beginning of each symbol, the duration of which is determined based on the delay spread of the wireless channel. The guard interval is typically referred to as Cyclic Prefix (CP) and; it is a cyclic extension of the time-domain samples obtained after the Inverse Fast Fourier Transform (IFFT) process.

2.1.2.1 OFDM Generation

From the implementation perspective, OFDM generation is straightforward, and it is efficiently implemented via Fast Fourier Transform (FFT) [59]. The number of subcarriers N are often set to a power of two, i.e., FFT size is determined as $N = 2\text{^}\text{x}$, where per subcarrier bandwidth is calculated as B/N Hz. Each subcarrier is modulated/mapped independently with, e.g., BPSK, 4-QAM, 16-QAM, symbols. After mapping, N-point IFFT is performed to convert the frequency-domain subcarriers into time-domain N samples, which are sent over-the-air interface. The time required to transmit N OFDM samples is called the FFT period or OFDM symbol duration, which is computed as N/B sec. At the receiver side, the OFDM signal is translated back into frequency-domain using FFT, and afterward, each subcarrier is demodulated/demapped.

Overall, the benefits of OFDM have led to a wide adaption of the wideband communication technology in several state-of-the-art wireless standards like WLAN, Long Term Evolution (LTE), digital audio broadcast, and terrestrial/satellite TV.

2.1.3 Wireless Local Area Networks (WLANs)

The widespread success of WLAN, along with the cellular network (3G and 4G), basically revolutionized present day wireless communications. These days, the wireless technologies based on standard specific applications are skyrocketing, and the present focus towards IoT networks has further intensified the standards' utilization such as WiFi, Bluetooth, and Zigbee. The present-day WLAN mostly uses the unlicensed sub-6 GHz Radio Frequency (RF) spectrum, which includes the well-explored 2.4 GHz and 5 GHz bands, where applications range from small in-home to large, campus-sized networks, and many more.

2.1.4 WiFi

Wireless-Fidelity (WiFi) is the most commercial protocol of the WLAN family and is based on the 802.11 standards. The Institute of Electrical and Electronics Engineers (IEEE) has created and maintained the 802.11 standard, which basically provides a set of the physical layer (PHY-layer) and Medium Access Control (MAC-layer) specifications for the implementation of WLAN. These specified protocols are designed to support backward compatibility and interoperability between the upgrades in the

new releases. The 802.11 standard defines the air interfaces between wireless clients and base stations in the frequency bands of 900 MHz, 2.4 GHz, 3.6 GHz, 5 GHz, and 60 GHz.

The OFDM based IEEE 802.11a/g is the most widely utilized release of 802.11 standards. The channel bandwidth defined for 802.11a/g is 20 MHz, with a total of 64 OFDM subcarriers having a 312.5 kHz spacing. From these 64 subcarriers, only 52 are used for communications, engaging a 16.25 MHz of useful bandwidth. In these 52 carriers, 48 subcarriers are used to carry the payload, and the other four are called the pilots, which typically hold pseudo-random symbols for the tracking and correction of phase distortions. The remaining 12 subcarriers, i.e., the five and six guards on both bandwidth edges and one DC component in the middle, are null-subcarriers. They essentially act as guard bands with no information signal. The 802.11a/g have a sensitivity ranging from -82 dBm to -65 dBm [60], which basically helps in deciding the baseband modulation scheme (from BPSK, 4-QPSK, 16-QAM, 64-QAM – paired with a code-rate 1/2, 2/3, 3/4) and the resultant data rate, which ranges between 6 Mbit/s to 54 Mbit/s.

The 64-points IFFT of the subcarriers results in 64 time-domain samples. With 16 CP samples (specified in the 802.11a/g standard), a total of 80 samples per one OFDM symbol are generated. A bandwidth of 20 MHz makes 4 µs symbol duration, i.e., 3.2 µs actual symbol duration and 800 ns for CP. The 802.11g standard operates in the 2.4 GHz band, and it has 3 (in the U.S.) to 4 (in Europe) non-overlapping and 11 overlapping channels in the 2.401 GHz – 2.484 GHz spectrum. On the other hand, the 802.11a standard operates in the 5 GHz band, and it has roughly 23 non-overlapping channels in the 4.915 GHz – 5.825 GHz spectrum. The 802.11a standard undergoes more absorption because of the smaller wavelength, and therefore, its coverage region is relatively less as compared to 802.11g. Nevertheless, 802.11g experiences more interference from other devices operating in the overly crowded 2.4 GHz.

Frame Structure

The frame structure of both IEEE 802.11a and g standards is roughly similar, especially the key fields, and starts with a *Preamble*, which includes four full OFDM

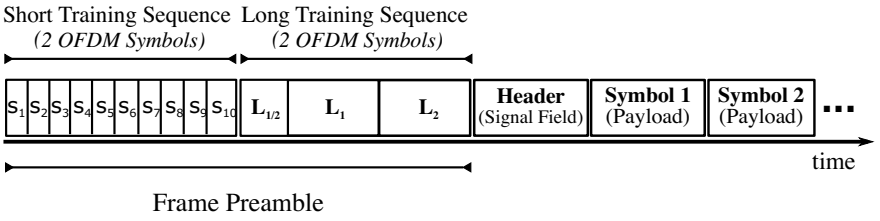

FIGURE 2.1 – IEEE 802.11 a/g standard frame structure.

symbols, each of 4 µs duration as illustrated in Figure 2.1. The *Preamble* is transmitted at a well-defined phase and magnitude, with two Short Training Sequence (STS) and Long Training Sequence (LTS) symbols each. The STS symbols in the frame structure are used for signal detection, diversity selection, timing synchronization, coarse frequency offset correction, and automatic gain control. The following LTS symbols are used for fine frequency offset correction and channel estimation and equalization. Followed by *Preamble* is the *Signal Field*, which is a single OFDM symbol – always transmitted with BPSK, and contains information of payload length, its modulation type, and the transmissions data rate. Afterward, payload symbols encoded with one of the previously mentioned baseband modulation scheme and a code rate are attached. Like the *Signal Field* OFDM symbol, pilots' subcarriers within the payload are also modulated with BPSK.

2.1.5 Automotive WLAN

The automotive WLAN is developed for Wireless Access in Vehicular Environments (WAVE), and it is specifically designed to support ITS application, such as in smart cities. The concept of smart cities forms the fundamental basis for future sustainable urban development and relies heavily on technological innovations. Smart mobility/transport (using ITS) is among the key elements of a Smart City, and it aims for effective, efficient, and safe management systems of transport, bicycle, public transportation, and parking [61].

Inter Vehicular Communications (IVCs) is an essential part of ITS, which include information exchange between Vehicle-to-Vehicle (V2V) and Vehicle-to-Infrastructure (V2I), or in a broader sense as Vehicle-to-anything (V2X) communication. In order to reduce the number of traffic accidents and; to improve the road traffic conditions, a 75 MHz bandwidth in the 5.9 GHz licensed spectrum is allocated specifically to support IVC for ITS [61]. In this regard, Dedicated Short Range Communication (DSRC) is standardized by the IEEE for vehicular communications, i.e., the IEEE 802.11p [62] standard.

IEEE 802.11p

Given the unique characteristics of the vehicular environment, the Vehicular Ad Hoc Network (VANET) for V2V and V2I communication required novel application-specific solutions on different layers of the network stack. Therefore, in order to make WLAN suitable for automotive applications, several adaptations in the basic 802.11 standards were made, and the updated release is referred to as IEEE 802.11p.

802.11p is also OFDM based, and it essentially is derived from 802.11a standard with roughly similar PHY-layer frame structure and operates in the 5.85 GHz – 5.925 GHz spectrum. The primary difference between 802.11p and 802.11a is the

bandwidth reduction from 20 MHz to 10 MHz. This essentially doubles the OFDM symbol duration, especially the CP to 1.6 µs, which makes the signal more tolerant to multipath propagation effects (e.g., the signal reflections from other cars or houses) and increases its robustness against fading in the vehicular communication environments. Nevertheless, the data rates with 802.11p are reduced by half, i.e., 3 Mbit/s to 27 Mbit/s.

Additionally, since it is highly probable that communication links between vehicles or infrastructures exist only for a very short time duration, the 802.11p allows information exchange between vehicles without establishing Basic Service Set (BSS); therefore, no need to wait for association and authentication protocols prior to exchanging information. The 802.11p-enabled stations utilize the wildcard BSS identifier with all 1s in the frame header they exchange and may initiate data frames exchange as soon as they acquire the communication channel. Since these stations are neither associated nor authenticated, the procedures defined by the IEEE 802.11 standard for authentication and data confidentiality cannot be used in 802.11p. Thus, higher network layers are responsible for providing these kinds of functionalities.

Very recently, "in November 2020, the FCC reallocated the lower 45 MHz half of the DSRC spectrum (5.850–5.895 GHz) for Wi-Fi and other unlicensed uses, arguing that the auto industry had largely failed to make use of the DSRC spectrum in its 21 years of existence, with only 15,506 vehicles in the US – 0.0057% of the total – equipped for DSRC"[1], which is quite unfortunate, and a clear sign indicating the need for deeper, concrete, and applicable research in the vehicular communication domain.

2.2 Visible Light Communication

Visible Light Communication (VLC) is a variant of wireless communication that utilizes the visible light spectrum between 400 THz to 800 THz frequencies for communications and; it is a subset of Optical Wireless Communications (OWC) technologies. Even-though VLC is normally considered a recent technology, the idea of message transmission through light dates back to the 1880s when Alexander Graham Bell first demonstrated it with his photophone [44]. VLC as a potential communication technology gathered significant attention after the demonstration of High-Definition video transmission using standard LED lamp in a TED Global presentation by Harald Haas in July 2011, and proposed the term LiFi for the technology. In recent years, VLC is becoming increasingly popular because of the fast switching capability of the LEDs and their proliferating usage almost everywhere [63].

[1] https://arstechnica.com/tech-policy/2020/11/fcc-adds-45mhz-to-wi-fi-promising-supersize-networks-on-5ghz-band/

VLC features an unlicensed and free band with huge available bandwidths. This allows the possibility of having very high data rate communication, and since the visible light spectrum does not overlap with the Radio Frequency spectrum, their electromagnetic interference is non-existent. Unlike RF, visible light cannot penetrate through solid objects such as concrete but can pass through transparent objects, such as glass, with limited attenuation. Also, the visible light is absorbed by dark bodies, whereas the light-colored bodies cause diffused reflections. For operation in outdoor environments, interference sources [64], such as ambient light, sunlight, and possible artificial light, influence as well. Additionally, in contrast to RF communications, VLC heavily relies on the uninterrupted, direct LoS link. This is primarily because of the much shorter carrier wave-lengths in VLC. However, this property of VLC enables efficient spatial diversity and prevents multipath fading, as its effective pathloss is larger, and the received power predominantly arrives through LoS only [61].

2.2.1 Modulation in VLC

Due to the unipolar nature of the light intensities, modulation in VLC is significantly different than RF communications [65] and; requires the light signal to be modulated around a positive DC level. Modulation schemes that are naturally unipolar, such as On-Off Keying (OOK) and Pulse Position Modulation (PPM), can be easily opted for VLC. However, bipolar modulation schemes, such as OFDM, are required to be transformed into unipolar waveform before modulating them onto visible light.

There are various approaches to achieve this transformation. The most straightforward approach is called Direct Current-Biased Optical OFDM (DCO-OFDM) [66], where the bipolar signal is translated onto a positive DC level. As a result of this superposition of a signal onto DC, a VLC transmitter requires a highly linear driver circuit with an optimal bias point to fully utilize the dynamic range without getting saturated. Asymmetrically Clipped Optical OFDM (ACO-OFDM) [67] is another widely studied modulation technique in VLC. In ACO-OFDM, the payload is only loaded on the odd subcarriers, while the even subcarriers forms a bias signal that ensures the requirement of a unipolar signal for intensity modulation.

Both DCO-OFDM and ACO-OFDM have their merits and demerits. In particular, DCO-OFDM can use all the subcarriers, but it is inefficient in terms of optical power because of the large DC bias, which prevents clipping of the negative peaks that exist because of high PAPR in OFDM. Whereas ACO-OFDM can experience the full amplitude, however, it only uses odd subcarriers for communications, which essentially reduces the bandwidth by half. Asymmetrically Clipped DC biased Optical OFDM (ADO-OFDM) is a hybrid technique that combines positive aspects of both DCO-OFDM and ACO-OFDM [68]. It simultaneously transmits ACO-OFDM on the odd subcarriers and DCO-OFDM on the even subcarriers. ADO-OFDM is shown

to be more spectrally efficient than ACO-OFDM and optically power-efficient than DCO-OFDM.

Besides these modulation techniques, there are other schemes as well for VLC, such as Color Shift Keying (CSK) and Wavelet Packet Division Multiplexing (WPDM). The suitability of any one of these modulation techniques often depends on the application domain, type of hardware, and communication distance.

Baseband Signal Processing in VLC

The baseband signal processing of bipolar modulation, such as OFDM, depends on the targeted optical modulation scheme and may require additional processing compared to RF. For instance, in the case of DCO-OFDM, the baseband processing performed in a typical RF system at both the transmitter and receiver side can straightforwardly be used, maybe with minor amplitude adjustment. Whereas, in the case of ACO-OFDM [69], additional processing in the baseband is required to prevent any loss of information due to the clipping of the negative part of the waveform.

2.2.2 VLC Front-end

The information in VLC is modulated in the optical domain that does not allows / transmission of non-negative values. Since, at an optical receiver, it is impossible to collect any electromagnetic power (unlike RF receivers); therefore, Intensity Modulation (IM) and Direct Detection (DD) is a common method adopted in the VLC front-ends for optical transmissions.

2.2.2.1 VLC Driver

As previously discussed, VLC requires intensity modulation. For this reason, the input voltage signal (baseband waveform) is converted into a current signal in order to drive the LEDs. For typical LEDs, in the case of direct connection, the voltage to current ratio is exponential, which results in a highly nonlinear behavior, and it is undesirable, especially for complex modulation schemes, such as OFDM. To compensate for this nonlinear behavior, Transconductance Amplifier (TCA) is normally used in the VLC driver circuits to hold the linearity conditions, which is very much required for distortion-free transmissions of discrete and analog baseband signals. For modulations schemes such as PPM or OOK with only digital levels, this linearity requirement is not essential, as the LED only needs to turn *On* and *Off* for communications. However, spectrally efficient modulation schemes like OFDM are typically considered in wireless systems for higher data rates, and these are naturally prone to the nonlinear behavior. Therefore, linearity of the driver circuit is usually a crucial requirement in VLC [70].

The effective bandwidth of the driver circuit is another important characteristic for bandwidth-efficient VLC. Particularly, a VLC driver is required to have a bandwidth sufficient enough to manage the switching frequency of an LED. Ideally, the driven LED's 3 dB bandwidth and the driving circuit bandwidth must match; for optimal performance. A driver circuit with high linearity and large bandwidth is critically required in VLC.

2.2.2.2 VLC Receiver

The receiving front-ends of VLC typically utilize photo-diodes that absorb the light intensity and generate electric current. These photo-diodes are usually coupled with a Transimpedance Amplifier (TIA), which converts the input current into a voltage signal that is later processed in the baseband to retrieve the sent data. Photo-diodes are quite cheap, with different types available such as avalanche photo-diode, PIN photo-diodes, and PN photo-diodes.

Besides photo-diodes, camera sensors have also been considered for the detection of VLC signals. However, due to higher cost, and lower sensitivity and bandwidth, these detectors have failed to capture the VLC market, and they are rarely used as VLC front-ends [71].

2.2.3 VLC Standardization

Being only a decade old, the standardization of VLC is underway. Several standardization efforts by the IEEE task groups are already made in recent years; in particular, IEEE 80.15.7, IEEE 802.15.3, and IEEE 802.11bb are worth mentioning. In December 2011, the IEEE 802.15.7 VLC task group drafted the Physical and MAC layers standard for outdoor applications. The PHY-layer modulation schemes proposed in the standard included OOK, Variable PPM, and CSK. The IEEE 802.11bb task group on light communication is working on standardizing Light Fidelity (LiFi). The special focus of the task group is to make LiFi and WiFi interoperable. Finally, the task group working on the IEEE 802.15.13 standard aims to achieve data rates up to 10 Gbit/s in the range of 200 m for the LoS link.

2.3 Remarks

To conclude this chapter, we explored Radio Frequency- and Visible Light-based wireless communication. In particular, we learned about the basis for in-band full-duplex wireless communications and discussed OFDM PHY-layer technology. We further look into Wireless Local Area Network (WLAN) and studied WiFi and IEEE 802.11p standards, specification, and utilization. For VLC-based wireless

communications, we learned the necessary requirements to enable VLC and the required optical modulation schemes for distortion-free transmissions. We also looked into the standardization efforts for VLC technology.

Part I: Conventional RF-based Wireless Systems

Chapter 3

In-band Full-Duplex Relaying

RELAYING in wireless networks is one of the most important techniques to improve overall communication performance and increase coverage. The conventional Half-Duplex (HD) relaying, unfortunately, incurs temporal and spectral losses. In-band full-duplex wireless communication has the potential to overcome various system-inherent deficiencies of existing half-duplex infrastructures. In particular, as opposed to traditional Half-Duplex Relaying (HDR) systems, an in-band Full-Duplex (FD) relay can simultaneously receive and forward, which improves the channel utilization and reduces the end-to-end delay in a multi-hop network significantly. Nevertheless, like in typical full-duplex wireless systems, one of the challenges associated with FD relays is the strict requirement of Looped Self-Interference (LSI) suppression. Also, in spite of many theoretical works on FD relaying, there is still no widely available implementation that is compliant with standards such as IEEE 802.11a/g/p, and the existing relaying approaches are still in their prime.

In this chapter, we, for the first time, present an IEEE 802.11 a/g/p compliant full-duplex relay implementation based on the GNU Radio framework. Given the open-source nature of this real-time signal processing software, the implementation is completely transparent and can be studied in all details and modified if needed. We further present performance comparison results with our IEEE 802.11a/g/p compliant relay implementation from a system-level perspective by means of real-time simulations and over-the-air experiments in an indoor setup. The first results demonstrate the potential of our Full-Duplex Relaying (FDR) implementation and the practical performance in comparison to traditional HD relaying in terms of packet delivery ratio, spectral efficiency, and physical layer latency.

The rest of the chapter is based on the following peer-reviewed publications:

- **M. S. Amjad and F. Dressler, "Experimental Insights on Software-based Real-Time SI Cancellation for In-Band Full Duplex DF Relays," in *IEEE In-***

***ternational Conference on Communications (ICC 2019)*, Shanghai, China: IEEE, May 2019.**

In this conference paper, my contributions were: the first Orthogonal Frequency Division Multiplexing (OFDM)-based Decode and Forward-FDR implementation in GNU Radio, with real-time LSI cancellation monitoring with Software-Defined Radio (SDR); the investigation of residual LSI impact on FDR performance and throughput, which increased by two folds when LSI is fully suppressed.

- **M. S. Amjad and F. Dressler, "Software-based Real-time Full-duplex Relaying: An Experimental Study," *IEEE Transactions on Green Communications and Networking (TGCN)*, vol. 4, no. 3, pp. 647–656, Sep. 2020.**

  This Journal article is the extension of my previous paper, additionally focused on: studying LSI impact due to estimation error, both analytically and in real-time simulation environment; channel capacity gain of FDR over HDR; comparison of experimentally obtained results with the simulative and analytical findings.

- **M. S. Amjad and F. Dressler, "Performance Insights on IEEE 802.11a/g Compliant Software-based In-Band Full Duplex Relay Systems," in *IEEE Wireless Communications and Networking Conference (WCNC 2019)*, Marrakesh, Morocco: IEEE, Apr. 2019.**

  In this conference paper, my contributions were: the analytical modeling of full-duplex relaying techniques, with closed-form expressions for numerical analysis; implementation of an FDR system that includes a novel core module for LSI cancellation in GNU Radio framework; evaluation and comparison of the IEEE 802.11a/g compliant HDR with FDR systems via an extensive-set of performance results for frequency selective-Rayleigh fading channels in simulations.

- **M. S. Amjad and F. Dressler, "Software-based In-Band Full Duplex Relays for IEEE 802.11a/g/p: An Experimental Study," in *IEEE Wireless Communications and Networking Conference (WCNC 2021)*, Nanjing, China: IEEE, Mar. 2021.**

  This conference submission is the extension of my previous paper, additionally focused on: improving the LSI suppression module of our preliminary implementation of FDR system in GNU Radio, which additionally estimates sampling offset for improved digital domain cancellation of LSI; evaluating the performance of an IEEE 802.11a/g/p compliant FDR system in real-time SDR-based experiments for both Line-of-Sight (LoS) and Nonline-of-Sight (NLoS) cases in an indoor environment.

3.1 Motivation

Presently, expanding wireless users and strong connectivity are critically bottlenecked by the wireless channel's unpredictable and degrading nature. The sensitivity of wireless signals towards time-varying channel impairments, noise, and other interference sources, poses pressing challenges for reliable communication – with consequential impact on the overall system performance. The amount of Signal-of-Interest (SoI) strength degradation while traveling from the source to destination sets the basis for the following decoding errors at the destination, and this affects not only the data rate but also the coverage area of a wireless system. For instance, in a highly degrading wireless channel, we can increase the coverage area of a wireless system at the cost of lower data rates along with the possible risk of losing the communication entirely, or reduce the coverage region (decreasing the cell size) to maintain the high data rates, which means more equipment. In recent years, to overcome this capacity vs. coverage dilemma, infrastructure relays have been utilized and even considered by wireless standards such as 3GPP LTE [5] and WiMAX [6], as they can greatly improve the system capacity and expand the coverage of a wireless network at the same time.

Nevertheless, these infrastructure relays operate in HD mode, which means they require additional resources typically in the time domain for reliable communication. As illustrated in Figure 3.1, a two-hop Time Division Duplexing (TDD)-based HDR receives the data from a source in time slot T_α and then waits to retransmit the data towards a destination in the next available time slot T_β, where the waiting time depends on the implemented relaying strategy (i.e., Amplify and Forward (AF) or DF scheme). The deployment of typical HDRs in a network increases the end-to-end latency (with such TDD-based relays) and; causes spectral losses (as in Frequency Division Duplex (FDD)-based relays), in addition to inefficient channel utilization.

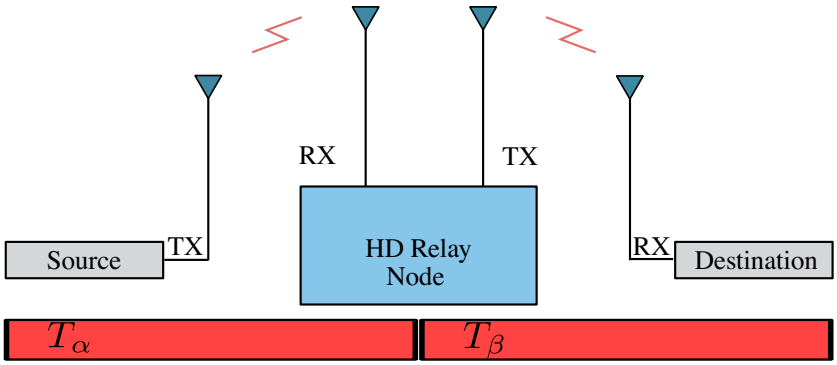

FIGURE 3.1 – A standard two-hop relay system operating in Half-Duplex mode.

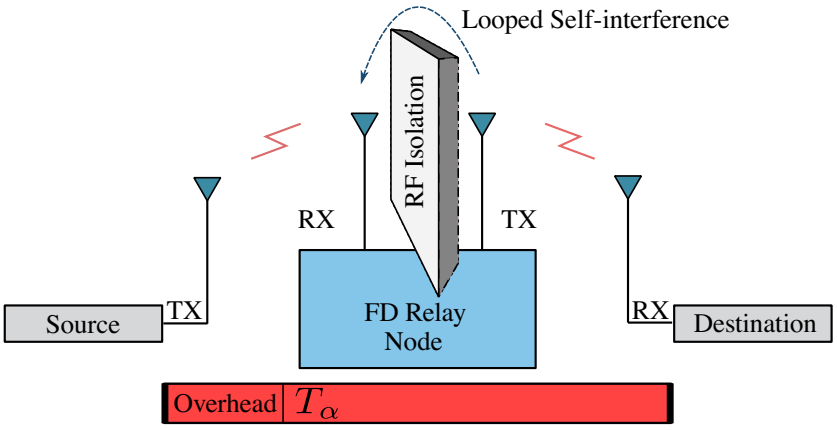

FIGURE 3.2 – A two-hop relay system operating in Full-Duplex mode.

In the past few years, a substantial amount of research has been done on in-band FD wireless systems [7]. Several works [8]–[11] presented different techniques and architectures to address the prime factor impeding FD wireless communications, namely the Self-Interference (SI), which primarily arises due to radio's own transmission at the same time and frequency. The capacity of a full-duplex radio to transmit and receive simultaneously primarily helps in recuperating with the spectral losses and in improving the effective channel utilization of classical half-duplex systems. Additionally, it mitigates the existing hidden terminal problem [12], reduces congestion issues [52], and supports primary user detection in cognitive radio, i.e., spectrum sensing for opportunistic spectrum usage [13].

Yet, while FD communication has gained much attention with a substantial volume of literature available, covering both theoretical and experimental works, full-duplex relaying is still an under-explored topic, with most of the existing studies based on analytical models only. An FDR system can simultaneously receive from the source and forwards towards the destination, as illustrated in Figure 3.2. This necessarily improves the spectral efficiency of FDD-based relays and considerably reduces the end-to-end delay in TDD-based relay systems, especially in a multi-hop network. This is particularly helpful in latency-critical applications such as vehicle platooning, where a leading platoon vehicle coordinates with its followers for effective road utilization and fuel-efficient driving [14]–[16].

The simultaneous reception and forwarding in FDR greatly reduce the end-to-end delay of a multi-hop relay system, with minimal channel utilization, i.e., least channel engagement of the relaying node. Nevertheless, for optimal performance, the suppression of LSI (due to simultaneous reception and forwarding) to the receiver's noise floor is a crucial requirement in an FDR system. Any residual LSI predominantly

worsens the noise floor for the SoI, resulting in degraded Signal-to-Noise Ratio (SNR) and, eventually, limiting the overall performance.

The mitigation of LSI in FDRs can essentially involve passive suppression and active cancellation stages. The passive suppression stage isolates the strong direct/leaked LSI component, thus, preventing the saturation of Analog-to-Digital Converters (ADCs) in the received signal processing path [72]. The active cancellation stage, on the other hand, can be done in the analog domain through RF cancellation circuitry and in the digital domain via modeling of an equivalent discrete system capturing the channel effects. The active cancellation of LSI is rather crucial in *Full-Duplex Relaying systems* as compared to typical *Full-Duplex wireless systems*. This is because, in full-duplex relaying, accumulating LSI via feedback is involved, and if not suppressed precisely, then it can drive the system towards instability and will be discussed more in later sections.

This chapter thoroughly investigates FDR for both AF and DF relaying strategies and compare it with traditional HDR. Here, we first analytically model a dual-hop FDR system, obtain the closed-form expressions for end-to-end SNR, and compare the analytical findings. To gain further understanding, we perform extensive real-time simulations with our IEEE 802.11a/g/p standard-compliant FDR implementation in the GNU Radio framework and compare its performance with HDR. For practical insights, we employ a passive suppression approach and linear digital domain cancellation in the GNU Radio radio framework for real-time system-level evaluation of our standard-compliant implementation via SDRs. To the best of our knowledge, this is the first work that evaluates the performance of FD relaying via real-world experiments using a General Purpose Processor (GPP)-based software implementation compliant to the IEEE 802.11a/g/p standard for WLAN. Our evaluation results demonstrate and underline the potential performance gains offered by FD relays over traditional HD relaying.

The core contributions of this chapter can be summarized as follows:

- We analytically model both AF and DF relaying strategies in HD and FD transmission modes, and obtain closed-form expressions, to numerically study the impact of amplification factor and estimation error in LSI channel on the received SNR.
- We evaluate and compare the performance of IEEE 802.11a/g compliant HDR with emerging FDR systems and present an extensive set of performance results for frequency-selective Rayleigh fading channels.
- For the first time, we evaluate the performance of an IEEE 802.11a/g/p compliant FDR system – primarily focusing on DF relaying – in real-time SDR-based experiments. We present an extensive set of measurement results in an indoor environment for both LoS and NLoS cases.

- We improved the LSI suppression module, which additionally estimates sampling offset for improved digital domain cancellation of LSI for real-world experiments with the SDRs, supporting live signal processing and runtime monitoring of LSI cancellation.

- We investigate the impact of residual LSI on the FDR performance in terms of Packet Delivery Ratio (PDR), spectral efficiency, and Physical Layer Latency (PLL). We also look into its impact on the noise floor relative to Signal-of-Interest (SoI) and the resultant transmit power requirements from the source node.

3.2 Related Studies

In the era of ever-growing wireless traffic and high-speed connectivity, the issue of coverage vs. data rates in a band-limited wireless link has gained significant attention. Infrastructure relays in this regard have effectively addressed the stated issue and have been adopted by many wireless standards. Nevertheless, due to their half-duplex nature, they do have added disadvantages like poor spectral usage and increased latency. The most commonly studied and employed relaying strategies include AF and DF schemes. In the literature, to overcome the added disadvantages of these relaying strategies due to their half-duplex nature, different works have considered approaches such as cooperative decoding for diversity gain [73] and two alternating relay nodes to mimic FD mode [74]. Nevertheless, these approaches have not been able to entirely compensate for the losses these HD relays incur.

In recent years, full-duplex relaying has been studied in quite a detail; after all, the implications of such relaying systems are qualitatively beneficial in terms of both spectral efficiency and network latency. However, most of the research conducted in the domain have presented their analytical findings and considered theoretical approaches to state the gains of FD relaying. For instance, in [75], the authors considered an AF relaying system with low-resolution ADC; and did analytical modeling of LSI and quantization noise to analyze the achievable spectral efficiency. Similarly, in [76], an analytical model has been employed based on Markov chain modeling to analyze the outage probability in FD multi-relay channels. Likewise, in [77], the optimal power allocation in DF based FDRs to effectively handle the residual LSI has been discussed. Other such works include [78], where the RF impairment effects such as nonlinear behavior of power amplifier have been analyzed; and [79], in which the impact of looped-back channel estimation error on the performance of AF-based FD relaying is studied. These studies and other similar works have mostly assumed (often implicitly) that the relay system has the full-duplex capability, and the LSI can be eliminated without any complication. As a

result, they not only lack actual implementation perspective but also make strong assumptions on requirements such as synchronization of estimated LSI and actual LSI for effective real-time cancellation.

Simulation studies, on the other hand, are typically developed to gain more insights and for the further verification of the analytical models, which for FD-based relays are already very limited in the literature. In [80], SC-FDE technique based FD relaying is proposed that utilizes AF scheme and is shown to be robust towards LSI via simulative evaluation. Similarly, an adaptive approach for the cancellation of LSI in AF-based relays that do not require the angle-of-arrival information for the temporal filter has been proposed [81]. Likewise, the work in [82] presented a hybrid design for opportunistic FD / HD relaying with transmit power adaptation and showed performance gain over individual mode based systems.

Apart from simulations, experimental studies offer practical insights. In particular, measurements through hardware show the performance of a real system and presents potential weaknesses in system design. In [83], a complete FDR design, implementation, and performance evaluation have been presented. The work introduced an intelligent class of AF relays and named it as Construct and Forward (CF) relaying, which unlike the naïve forwarding done by a typical AF relay, forwards the relayed signal in such a way that it constructively adds up with the direct signal (coming from source) at the destination. In order to work effectively, the constructive filter used at the relay node requires the Channel State Information (CSI) of all four paths, i.e., S-R, R-R, R-D, and S-D, which is a complex task. Also, the proposed design is still based on AF relaying, and although CF avoids noise amplification by efficiently choosing the amplification factor, this also reduces the power levels of the relayed signal and compromises the system performance. Another work [84] introduced a complete prototype implementation for in-band full-duplex relaying, mainly exploiting the LSI techniques, and proposed a novel wave-trap antenna design for passive suppression and digital domain cancellation stages for LSI suppression to the noise floor.

Apart from the contemporary full-duplex and half-duplex relay systems, an advanced approach, i.e., buffer-aided relaying [85]–[87], for the general two-hop FD relay system is also proposed in the literature. The buffer-aided relaying approach adaptively selects either to receive, transmit, or both transmit and receive simultaneously, in a given time slot based on the quality of the self-interference channel. In [86], the overall throughput rates are shown to be improved with buffer-aided FD relaying compared to conventional FD relaying but only under the assumption that there is residual LSI and as long as source and destination nodes are in communication range. The work in [87] further maximizes the throughput of such buffer-aided FD relaying in fading channels. Nevertheless, these works are numerical and/or

simulative studies under certain assumptions and certainly, lack the perspective of practical performance and challenges.

Contrary to the mentioned works, this study presents real-time GNU Radio-based implementation of an FDR more focused on DF relaying scheme, which eliminates the noise amplification limitation of AF- and CF-based FD relays. Additionally, the existing implementations are Field-Programmable Gate Arrays (FPGA)-based such as WARP Mango board [83], and while these FPGA-based SDRs offer deterministic timing and low latency, nevertheless, they are rather inflexible, and it is often challenging to implement complex signal processing algorithms in them. In-contrast, our proposed FDR implementation is GPP-based, build upon open-source platform GNU Radio, which is easily accessible, and the same code can be used for both simulations and experiments, therefore, offering a seamless switch between theory and real-world. Additionally, the framework supports real-time software signal processing, with high-level programming languages C++ and Python, and it is compatible with a wide variety of SDR radio front-ends such as in [72]. Thus, making it particularly easy to use, modify, and debug.

3.3 Two-Hop Relaying Model

In this work, we consider a two-hop relay system, where a source communicates with a destination via an intermediate relay node, which supports both AF and DF relaying strategies. In our framework, it is assumed that packets from the source cannot reach the destination directly, i.e., a non-cooperative decoding scheme and the relay node in-between can operate in both HD and FD modes, as shown in Figures 3.3 and 3.4, respectively.

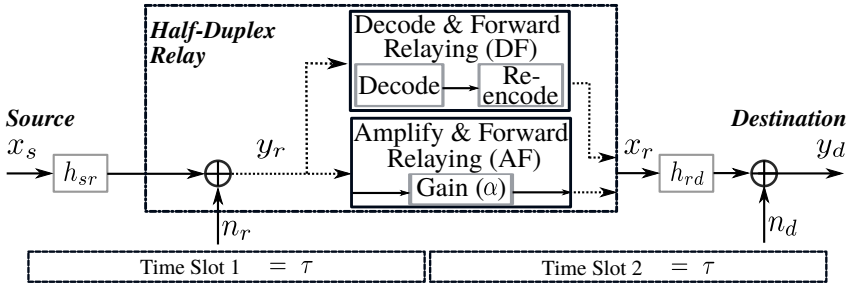

FIGURE 3.3 – Block diagram of a two-hop transmission link communicating via an intermediary relay node operating in HD mode supporting both AF and DF relaying strategies, © 2019 IEEE [88].

3.3.1 Traditional Half-Duplex Relays

When the considered system operates in HD transmission mode, depicted in Figure 3.3, the relay node receives a packet from a source in time slot T_1, and depending on the relaying strategy, either amplifies it by a factor α or decodes and re-encodes it before forwarding the packet towards the destination in the next time slot T_2. The baseband samples at the inputs of a relay (y_r) and destination (y_d) nodes can be written as

$$y_r[i] = x_s[i] * \bar{h}_{sr} + n_r[i], \tag{3.1}$$

$$y_d[i] = x_r[i] * \bar{h}_{rd} + n_d[i], \tag{3.2}$$

where x_s and x_r are the samples generated by source and relay nodes, n_r and n_d are the zero mean AWGN noise samples at the relay and destination ends, and $\bar{h}_{sr}$, $\bar{h}_{rd}$ are the channel impairment coefficients of source-relay and relay-destination channels, respectively. The instantaneous transmitted signal powers in Equations (3.1) and (3.2) can be obtained as $E\{|x_s[i]|^2\} = P_s$ and $E\{|x_r[i]|^2\} = P_r$. Likewise, the noise powers at relay and destination nodes can be calculated as $E\{|n_r[i]|^2\} = \sigma_r^2$ and $E\{|n_d[i]|^2\} = \sigma_d^2$.

3.3.1.1 Amplify & Forward Relaying

In the case of AF relaying strategy, from (3.1) the instantaneous received SNR at relay node (γ_r) can be computed as

$$\gamma_r = \frac{P_s \|h_{sr}\|^2}{\sigma_r^2}, \tag{3.3}$$

where $\|h_{sr}\|^2$ is the inner product of channel coefficients. In-terms of source samples (x_s), Equation (3.2) can be written as

$$y_d[i] = \alpha \cdot (x_s[i-\tau] * \bar{h}_{sr} + n_r[i-\tau]) * \bar{h}_{rd} + n_d[i], \tag{3.4}$$

where τ is the delay of one time slot introduced before forwarding the samples towards destination. This delay basically prevents simultaneous transmission and reception that causes LSI (i.e., the full-duplex mode). Thus, from Equation (3.4) the instantaneous end-to-end SNR ($\gamma_d^{\text{AF-HD}}$) in AF-HDRs can be obtained as

$$\gamma_d^{\text{AF-HD}} = \frac{\alpha^2 \cdot P_s \|h_{sr}\|^2 \|h_{rd}\|^2}{\alpha^2 \cdot \sigma_r^2 \|h_{rd}\|^2 + \sigma_d^2}. \tag{3.5}$$

Using Equation (3.3), $\gamma_d^{\text{AF-HD}}$ in (3.5) can be obtained in-terms of γ_r as

$$\gamma_d^{\text{AF-HD}} = \gamma_r \cdot \frac{\alpha^2 \cdot \|h_{rd}\|^2}{\alpha^2 \cdot \|h_{rd}\|^2 + \sigma_d^2/\sigma_r^2}. \tag{3.6}$$

Hence, in Equation (3.6), $\gamma_d^{\text{AF-HD}}$ not only depends on the SNR acquired at relay node, but also on the amplification factor α, and the ratio between noise powers of destination and relay ends.

3.3.1.2 Decode & Forward Relaying

In the case of DF relaying strategy, from Equation (3.1) the instantaneous received SNR at relay node (γ_r) and destination node (γ_d) can be computed as

$$\gamma_r = \frac{P_s\|h_{sr}\|^2}{\sigma_r^2} \text{ and } \gamma_d = \frac{P_r\|h_{rd}\|^2}{\sigma_d^2}. \tag{3.7}$$

Since, DF relaying protocol decodes and re-encodes each symbol, therefore, the instantaneous end-to-end SNR ($\gamma_d^{\text{DF-HD}}$) can be written as

$$\gamma_d^{\text{DF-HD}} = min\left\{\frac{P_s\|h_{sr}\|^2}{\sigma_r^2}, \frac{P_r\|h_{rd}\|^2}{\sigma_d^2}\right\}, \tag{3.8}$$

i.e., γ_r or γ_d whichever is the worst, benchmarks the overall DF-HDR performance.

3.3.2 Full-Duplex Relaying Model

When relaying is done in FD mode, the relay node receives the samples y_r from sources and simultaneously forwards the processed samples x_r towards the destination. This results in looped-back SI, which is therefore required to be suppressed

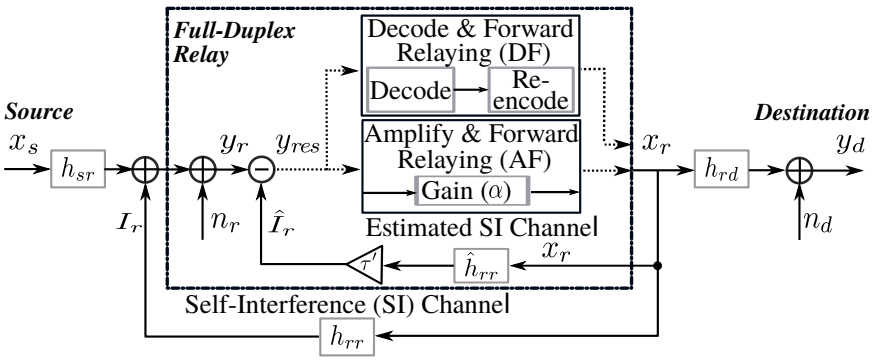

FIGURE 3.4 – Block diagram of a two-hop transmission link communicating via an intermediary relay node operating in FD mode supporting both AF and DF relaying strategies, © 2019 IEEE [88].

before feeding the samples y_r to the amplification or decoding blocks, as depicted in Figure 3.4. Otherwise, the DF protocol will not be able to decode anything, and the AF protocol will amplify and forward everything, including LSI.

The received samples at the input of a relay node after LSI suppression (y_{res}) are obtained as

$$y_{\text{res}}[i] = x_s[i] * \bar{h}_{sr} + n_r[i] + I_r[i-\tau'] - \hat{I}_r[i-\tau']. \tag{3.9}$$

In Equation (3.9), I_r and $\hat{I}_r$ are the actual and estimated looped-back SI samples, and τ' is the delay incurred by the channel and decoding process (DF strategy). Note that if τ' is not acquired correctly, then the subtraction of non-synchronized estimated LSI $\hat{I}_r$ from looped-back SI I_r, can drive the system towards instability. This synchronization of the estimated and received LSI is mostly overlooked (i.e., implicitly assumed to be synchronized) in the available simulation and analytical studies. For real-time systems, however, it is the fundamental requirement in FDR implementations; more details are provided in Section 3.4. The residual signal samples (y_{res}) in Equation (3.9) can be reformulated as

$$y_{\text{res}}[i] = x_s[i] * \bar{h}_{sr} + n_r[i] + x_r[i-\tau'] * (\bar{h}_{rr} - \bar{\hat{h}}_{rr}), \tag{3.10}$$

where $\bar{h}_{rr}$ and $\bar{\hat{h}}_{rr}$ are the actual and estimated relay-relay channel coefficients.

On the other hand, the received samples at the input of destination node (y_d) are obtained as

$$y_d[i] = x_r[i] * \bar{h}_{rd} + n_d[i]. \tag{3.11}$$

3.3.2.1 Looped Self-Interference Regeneration

The regeneration of LSI ($\hat{I}_r[i]$) is a two step process, and in this work it is performed in the time-domain. In the first step, an estimate of the LSI channel ($\bar{\hat{h}}_{rr}$) is obtained. Whereas, in the second step, the known samples $x_r[i]$ are filtered in time-domain with the estimated LSI channel coefficients $\bar{\hat{h}}_{rr}$ as

$$\hat{I}_r[i] = x_r[i] * \bar{\hat{h}}_{rr}. \tag{3.12}$$

The second step enforces channel impairment effects on the forwarded samples x_r in order to generate approximate LSI ($\hat{I}_r$). Thus, the reconstructed self-interference samples $\hat{I}_r[i]$, essentially carry similar channel properties as that held by the received LSI samples $I_r[i]$.

LSI Channel Estimation: for the estimation of LSI channel, we have employed the Least Square (LS)-based time-domain estimation technique. The LS approach

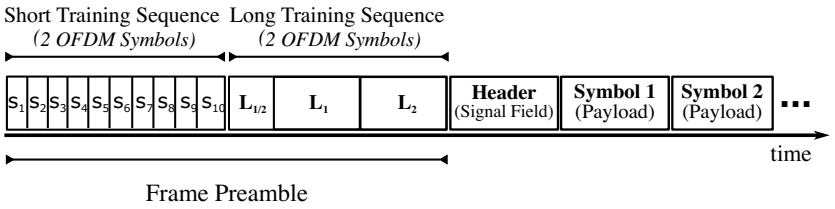

FIGURE 3.5 – Overview of IEEE 802.11 a/g/p standard for WLAN frame structure. Each frame includes two short and long training sequence symbols for coarse and fine synchronization and; for channel estimation purposes. Followed by them is the signal field carrying the information of frame length and payload samples encoding, and then the actual payload symbols.

basically acquires the Channel Impulse Response (CIR) estimate $\hat{\bar{h}}_{rr}$ through the Long Training Sequence (LTS) symbol embedded in the WLAN frame structure shown in Figure 3.5. For the in-band full-duplex communication, this estimation process is typically completed during the training transmissions, i.e., no emissions from the other radio or in-case of FD relaying no transmissions from the source node. From Figure 3.4, the received samples $y_r[i]$ during training transmissions, i.e., $x_s[i] = 0$, can be written as

$$y_r[i] = x_r[i] * \bar{h}_{rr} + n_r[i], \tag{3.13}$$

i.e., only looped-back self-interference samples ($I_r[i]$) are present. Using (3.13), the received LTS symbol samples can be presented as

$$\bar{y}^l_{r\text{-}lts} = \bar{x}^l_{r\text{-}lts} * \bar{h}^P_{rr} + \bar{n}^l_{r\text{-}lts}, \tag{3.14}$$

where l indicates the number of LTS samples (equal to FFT size, i.e., 64 in this case), and P represents the length of channel taps to be estimated, which typically corresponds to selected Cyclic Prefix (CP) length. For predetermined and known (standardized) $\bar{x}^l_{r\text{-}lts}$ samples, the time-domain convolution in (3.14) can be transformed into matrix multiplication as

$$\bar{y}^l_{r\text{-}lts} = \mathbf{X}^{l\times P} \cdot \bar{h}^P_{rr} + \bar{n}^l_{r\text{-}lts}. \tag{3.15}$$

In Equation (3.15), $\mathbf{X}^{l\times P}$ is the Toeplitz matrix of order $l \times P$, constructed (see [10]) using the known sent LTS samples. The time-domain LS channel estimate is thus acquired as

$$\hat{\bar{h}}^P_{rr} = \mathbf{X}^{l\times P^\dagger} \cdot \bar{y}^l_{r\text{-}lts}, \tag{3.16}$$

where $\mathbf{X}^{l\times P^\dagger}$ is the Moore-Penrose (pseudo) inverse of $\mathbf{X}^{l\times P}$ and $\bar{y}^l_{r\text{-}lts}$ are the received LTS samples. Notice that the sent LTS samples ($\bar{x}^{lts}_l$) are fixed and already known, thus the matrix $\mathbf{X}^{l\times P^\dagger}$ can be precomputed and stored in advance, without additional

computational requirement. Additionally, the error magnitude between the estimated and actual LSI channels is obtained as

$$\|\bar{e}_{rr}\|^2 = \|\hat{\bar{h}}^P_{rr} - \bar{h}^P_{rr}\|^2 = \|\mathbf{X}^{l\times P^\dagger} \cdot \bar{n}^l_{r\text{-}lts}\|^2, \tag{3.17}$$

i.e., the main source of error in the estimation of LSI channel ($\bar{h}_{rr}$) is the receiver noise values. Using (3.17), Equation (3.10) can be formulated as

$$y_{\text{res}}[i] = x_s[i] * \bar{h}_{sr} + n_r[i] + x_r[i-\tau'] * \bar{e}_{rr}, \tag{3.18}$$

In Equation (3.18), if $\bar{e}_{rr} = 0$ means that the LSI is completely eliminated, and the resultant samples (y_{res}) only contains the SoI and receiver's noise (n_r). In such a case, the performance of FD relaying is similar to HD relaying. However, error vector $\bar{e}_{rr}$ is never zero in practice, but can be reduced to substantially small values, which essentially enables full-duplex relaying.

3.3.2.2 Amplify & Forward Relaying

In AF relaying, using Equation (3.18), the instantaneous SNR at relay node (γ_r) after LSI suppression is obtained as

$$\gamma_r = \frac{P_s\|h_{sr}\|^2}{\sigma_r^2 + P'_r\|e_{rr}\|^2}, \tag{3.19}$$

where $\|e_{rr}\|^2$ is the inner product of error vector, $E\{|x_s[i-\tau']|^2\} = P'_s$ and $E\{|x_r[i-\tau']|^2\} = P'_r$ are the instantaneous transmitted signal power of the delayed sample, and $E\{|n_r[i]|^2\} = \sigma_r^2$ and $E\{|n_d[i]|^2\} = \sigma_d^2$ are noise powers. Note that the magnitude of residual LSI, i.e., $I_r - \hat{I}_r$, increases with large $\|e_{rr}\|^2$, which eventually reduces the γ_r. From (3.18) and (3.11), the samples forwarded by relay node x_r, and the samples received at destination node y_d can be written as

$$x_r[i] = \alpha \cdot (x_s[i] * \bar{h}_{sr} + n_r[i] + x_r[i-\tau'] * \bar{e}_{rr}) \tag{3.20}$$

$$y_d[i] = \alpha \cdot (x_s[i] * \bar{h}_{sr} + n_r[i] + x_r[i-\tau'] * \bar{e}_{rr}) * \bar{h}_{rd} + n_d[i]. \tag{3.21}$$

Using (3.20), P'_r can be computed as

$$P'_r = \alpha^2 \cdot (P'_s\|h_{sr}\|^2 + \sigma_r^2 + P''_r\|e_{rr}\|^2), \tag{3.22}$$

and from (3.21), the instantaneous end-to-end SNR $\gamma_d^{\text{AF-FD}}$ is obtained as

$$\gamma_d^{\text{AF-FD}} = \frac{\alpha^2 \cdot P_s\|h_{sr}\|^2\|h_{rd}\|^2}{\alpha^2 \cdot \sigma_r^2\|h_{rd}\|^2 + \alpha^2 \cdot P'_r\|e_{rr}\|^2\|h_{rd}\|^2 + \sigma_d^2}. \tag{3.23}$$

Equation (3.23) can be rewritten in-terms of γ_r as

$$\gamma_d^{\text{AF-FD}} = \gamma_r \cdot \frac{\alpha^2 \cdot \|h_{rd}\|^2}{\alpha^2 \cdot \|h_{rd}\|^2 (1 + P_r' \|e_{rr}\|^2 / \sigma_r^2) + \sigma_d^2 / \sigma_r^2}. \tag{3.24}$$

By analyzing Equations (3.19), (3.22) and (3.24), it can seen that the residual LSI due to $\|e_{rr}\|^2$, does not only have a direct impact on $\gamma_d^{\text{AF-FD}}$, but it also affect $\gamma_d^{\text{AF-FD}}$ indirectly through γ_r.

3.3.2.3 Decode & Forward Relaying

In the case of DF relaying strategy, by using Equations (3.11) and (3.18), the instantaneous received SNR at relay node (γ_r) and destination node (γ_d) can be computed as

$$\gamma_r = \frac{P_s \|h_{sr}\|^2}{\sigma_r^2 + P_r' \|e_{rr}\|^2} \text{ and } \gamma_d = \frac{P_r \|h_{rd}\|^2}{\sigma_d^2}, \tag{3.25}$$

and like DF-HDR, the instantaneous end-to-end SNR ($\gamma_d^{\text{DF-FD}}$) in DF-FDR is obtained as

$$\gamma_d^{\text{DF-FD}} = min \left\{ \frac{P_s \|h_{sr}\|^2}{\sigma_r^2 + P_r' \|e_{rr}\|^2}, \frac{P_r \|h_{rd}\|^2}{\sigma_d^2} \right\}. \tag{3.26}$$

From the comparison of Equations (3.8) and (3.26) it can be seen that unlike HD mode, $\gamma_d^{\text{DF-FD}}$ in FD mode is also affected by the residual LSI, i.e., $P_r' \|e_{rr}\|^2$ factor, and when $\|e_{rr}\|^2 = 0$, which in-practice never happens, both HD and FD modes offer same $\gamma_d^{\text{DF-FD}}$.

3.3.3 Analytical Findings

The end-to-end SNR expressions obtained previously for both AF and DF relaying operating in full-duplex mode demonstrate the critical dependence of FDR or amplification factor and error in the LSI channel estimate. The following sections analyze the degrees to which these factors impact the performance of FD relaying.

3.3.3.1 Impact of Amplification Factor

From Equations (3.3) and (3.19), it can be seen that the performance of AF scheme based relays largely rely on the amplification factor (α). Unlike DF relaying scheme, where the relay node decodes and re-encodes each symbol and regenerates noise-free samples entirely, in AF relaying the received samples are simply amplified and forwarded. This results in the magnification of the noise component as well. Thus, for optimal performance, the selection of amplification factor plays a critical role, especially in FD mode, where α has a direct relation with the error vector. Notice

that for $\|\bar{e}_{rr}\| = 0$ in (3.19), both HD and FD modes offer the same end-to-end SNR, i.e., $\gamma_d^{\text{AF-HD}} = \gamma_d^{\text{AF-FD}}$.

Figure 3.6 shows the impact of amplification factor on normalized received SNR for different $\|\bar{e}_{rr}\|$ values. For simplicity, here, we have assumed similar channel conditions, i.e., $\|\bar{h}_{sr}\|^2 \approx \|\bar{h}_{rd}\|^2 \approx 1$, and receiver noise component, i.e., $\sigma_r^2 \approx \sigma_d^2$. Also, the relay transmit power to noise ratio in (3.19) is fixed as 20 dB, i.e., $P_r'/\sigma_r^2 =$ 20 dB. Under the stated assumptions, it can be seen in the plot that for a given $\|\bar{e}_{rr}\|$, α provides an optimum $\gamma_d^{\text{AF-FD}}$ at a certain value, i.e., $\alpha = 7$ for $\|\bar{e}_{rr}\|$ up-to 0.001. Afterward, increasing α degrades the instantaneous SNR $\gamma_d^{\text{AF-FD}}$, and the degradation slope relies heavily on $\|\bar{e}_{rr}\|$. Intuitively, a further higher P_r'/σ_r^2 will lead to an even worse $\gamma_d^{\text{AF-FD}}/\gamma_r^{\text{AF-HD}}$ performance, certainly because of a stronger self-interference component in (3.19). These numerical results clearly show the critical dependence of AF-FDR performance on both amplification factor and error vector magnitude.

3.3.3.2 Impact of Estimation Error

In contrast to HD relaying, where the reception and forwarding are time separated, FD relaying inherently suffers from LSI because of simultaneous reception and forwarding. For the assumed case of equal transmit powers of both source (P_s) and relay (P_r) nodes, and under the assumptions of similar channel conditions (i.e., $\|\bar{h}_{sr}\|^2 \approx \|\bar{h}_{rd}\|^2 \approx 1$) and receiver noise component (i.e., $\sigma_r^2 \approx \sigma_d^2$) as done before, the end-to-end SNR gain G_{AF} can be obtained as a ratio of AF-FDR over AF-HDR as

$$G_{\text{AF}} = \gamma_d^{\text{AF-FD}}/\gamma_d^{\text{AF-HD}} = \frac{\alpha^2 + 1}{\alpha^2 \cdot (\|e_{rr}\|^2 \cdot P_r'/\sigma_r^2 + 1) + 1}. \tag{3.27}$$

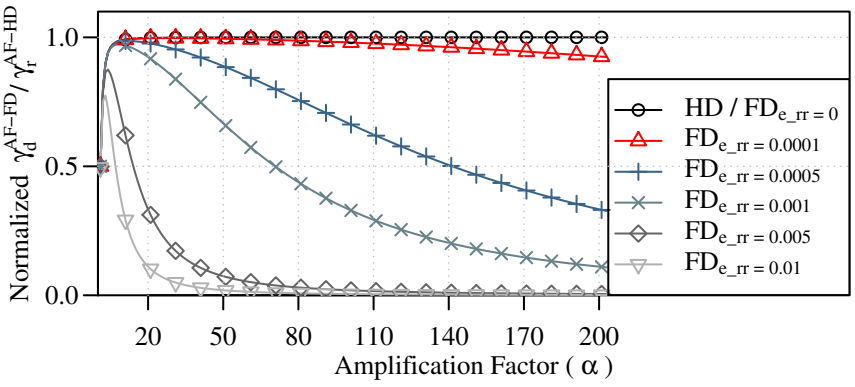

FIGURE 3.6 – Normalized instantaneous SNR $\gamma_d^{\text{AF-FD}}/\gamma_r^{\text{AF-HD}}$ versus amplification factor α for different $\|\bar{e}_{rr}\|$ values.

Likewise, from (3.6) and (3.26), the end-to-end SNR gain G_{DF} in case of DF relaying is computed as

$$G_{\mathrm{DF}} = \gamma_d^{\text{DF-FD}} / \gamma_r^{\text{DF-HD}} = \frac{1}{1 + \|e_{rr}\|^2 \cdot P_r'/\sigma_r^2}. \tag{3.28}$$

From (3.27) and (3.28), it can be seen that the prime SNR depreciating factor in FDRs for some fixed optimum α (in case of AF scheme) and transmit power levels, is the error vector magnitude $\|\bar{e}_{rr}\|$. In this regards, the normalized capacity gain $C_{\mathrm{FD/HD}}$ (in *bits/s/Hz*) of both AF and DF relaying schemes in terms of collective SNR gains (G_{AF} and G_{DF}) of FD mode over their HDR counter part can be calculated as

$$C_{\mathrm{FD/HD}}^{\mathrm{AF}} = log_2\left(1 + \frac{\alpha^2 + 1}{\alpha^2 \cdot (\|e_{rr}\|^2 \cdot P_r'/\sigma_r^2 + 1) + 1}\right), \tag{3.29}$$

$$C_{\mathrm{FD/HD}}^{\mathrm{DF}} = log_2\left(1 + \frac{1}{1 + \|e_{rr}\|^2 \cdot P_r'/\sigma_r^2}\right). \tag{3.30}$$

Figure 3.7a demonstrates the impact of estimation error $\|\bar{e}_{rr}\|$ on the capacity gain for different transmit power levels of the relay node for both AF (with fixed $\alpha = 7$) and DF schemes. To ease putting this graph into context, we plot the relative residual LSI at different transmit power of the relay node for increasing error in the LSI channel estimates in Figure 3.7b. From the comparison of capacity gains in AF and DF schemes, it can be observed that there is a drastic drop in AF performance with increasing error magnitude, especially at higher P_r'/σ_r^2 certainly because of the

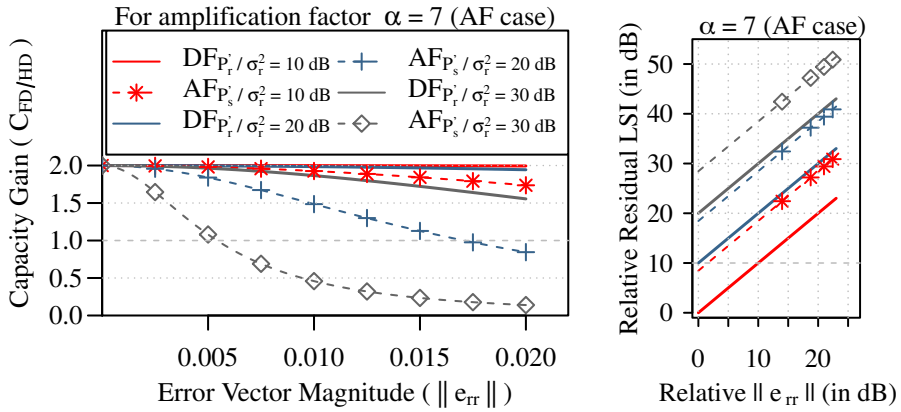

(a) Capacity gain of FD relaying over traditional HD relaying.

(b) Residual LSI.

FIGURE 3.7 – Channel capacity gain of AF and DF relaying schemes and relative residual LSI against increasing error vector magnitude $\|\bar{e}_{rr}\|$ for different transmit power levels. In sub-figure (b), the $\mathrm{DF}_{P_r'/\sigma_r^2=10\,\mathrm{dB}}$ is used as a benchmark to normalize the residual LSI due to higher power and error values.

multiplicative amplification factor α, which further aggravates the self-interference component. Additionally, the performances of both relaying schemes are only comparable for very small error values, which can be hard to ensure. Moreover, these results clearly indicate the crucial dependence of FDR performance on both estimation error magnitude and the relay node transmission power, where, in the presence of estimation error, a large transit power at the relay end substantially depreciate the overall end-to-end SNR γ_d^{FD}. These numerical finding particularly asserts the advantage of DF-FDRs over AF-FDRs in-terms of capacity gain.

3.4 Implementation Details

For simulative and experimental evaluation of both TDD-based HD and in-band FD transmission modes, we implemented the two investigated AF and DF relaying schemes in the GNU Radio signal processing framework. We choose GNU Radio as the implementation platform because of its wide-spread use as a real-time signal processing framework and its ability to do rapid prototyping – meanwhile supporting both simulations and experimental evaluation using SDR. Moreover, the GNU Radio Companion (GRC), a graphical tool for creating flowgraphs, allows to monitor – the real-time received/processed samples through visualization scopes in both time and frequency domains.

For the baseband processing at the source, relay, and destination nodes, we used the GNU Radio-based open-source stack for IEEE 802.11a/g/p WLAN developed by Bloessl et al. [89]. The core of this framework is a modular and flexible OFDM transceiver implementation, which is fully compatible with commercial WiFi cards and has been comprehensively evaluated in [90]. The key physical layer parameters within this transceiver design are listed in Table 3.1. One of the major reason of using this implementation is to later test our FD relaying system with SDR and to possibly evaluate its performance with commercial WiFi cards.

Table 3.1 – Key physical layer parameters of GNU Radio-based open-source stack for IEEE 802.11a/g/p, © 2019 IEEE [88].

Parameters	
Modulations	B-PSK, Q-PSK, 16-QAM & 64-QAM
Code Rates	1/2, 3/4, 2/3
Sampling Frequency [MHz]	10, 20
Data Rates [Mbit/s]	6, 9, 12, 18, 24, 36, 48, 54
FFT/IFFT Size	64 points
Cyclic Prefix Length	16 samples
PLCP (Preamble + Header)	(4 + 1) OFDM Symbols

The implementation of an HD relay node is rather straightforward as it just needs to receive the packet from the source in the first time slot, employ the relaying scheme, and forward the packet towards the destination in the next time slot. For an FD relay node, however, the suppression of LSI is required, for which we have implemented a core module in GNU Radio. It is worth mentioning here that in order to suppress the LSI, it is necessary to feedback the relay forwarded samples for the reconstruction of approximate LSI. The GRC, however, does not support live feedback of the streaming samples within a flow graph. To bypass this bottleneck, all the relay forwarded samples are first converted into a Protocol Data Unit (PDU) message and then fed back to the LSI cancellation module. It is important to mention here that the GRC does not allow direct feedback of the streaming samples in a flow graph, which is the key requirement in FD relaying, necessary for the reconstruction of LSI. For this reason, all the re-encoded samples x_r are first converted into a PDU message and then fed back to the looped SI cancellation module, as illustrated in Figure 3.8.

3.4.1 LSI Cancellation Module

Figure 3.8 shows our LSI cancellation module that we implemented in the GNU Radio framework. It operates in the time-domain and primarily estimates the LSI channel, and processes the known forwarded samples from the relay node to reconstruct an approximate LSI (only linear component). The module initially transmits $C_k + 1$ training packets within the relay node for the estimation of the LSI channel and for stabilizing the sub-blocks such as signal synchronizer. Here, C_k indicates the number of training packets, and k is the frequency of the estimation process. During the transmission of training packets, the transmissions from the source are turned off until the relay switches to full-duplex relaying mode, as shown in Figure 3.8.

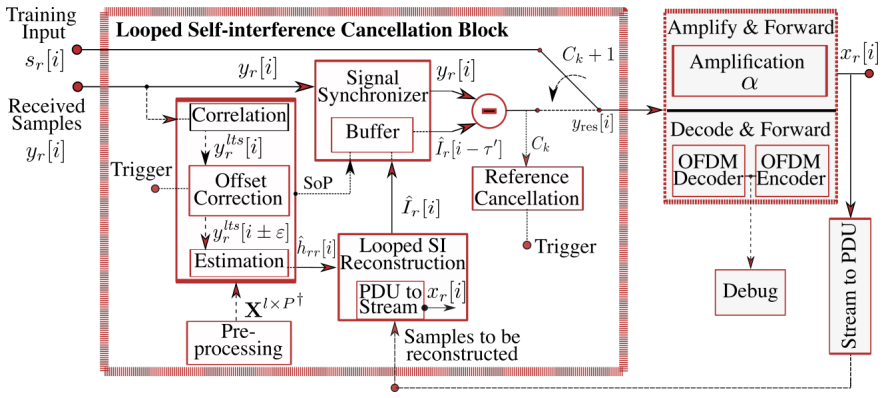

FIGURE 3.8 – Baseband level block diagram of the implemented novel LSI cancellation module for FDR implementation.

3.4.1.1 Preprocessing

The preprocessing block performs the tasks that are independent of real-time processing and utilizes the known parameters for information extraction. It initiates the IFFT of the LTS symbol enclosed in the WLAN packet preamble, hence; converting it into time-domain samples. Later, the obtained samples are used to create Toeplitz matrix $\mathbf{X}^{lxP}$, and finally, to calculate the Moore-Penrose (pseudo) inverse $\mathbf{X}^{l\times P^{\dagger}}$ of the Toeplitz matrix, which is later used with the received LTS samples $y^{l}_{r\text{-}lts}$ to compute the LSI channel estimate. Here, l is same as the number of IFFT points, and P is set to be half of CP; the values of each are listed in Table 3.1, respectively.

3.4.1.2 Estimation

The estimation block operates only during the training transmissions, i.e., C_k packets transmission. It first correlates the received samples y_r with the known LTS samples x^{N}_{LTS} to determine the Start-of-Packet (SoP). Once SoP is determined, it then extracts the received LTS samples $y^{l}_{r\text{-}lts}[i]$, which later undergoes the process of iterative FFT offset correction. The degree of FFT offset is computed using the reference cancellation module in Figure 3.8, which stores the offset value with the highest cancellation as reference. For offset correction, each iteration evaluates the averaged cancellation, compares it with the reference value, and overrides the previous cancellation and FFT offset values ($y^{lts}_{r}[i \pm \varepsilon]$) only if the current one is offering better results. The typical offset (ε) value varies between 8 samples. Figure 3.9 demonstrates the

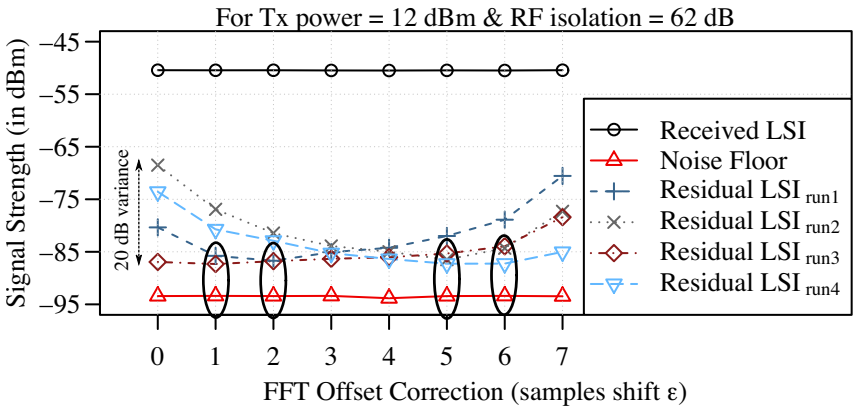

FIGURE 3.9 – Residual signal strength with different FFT offset correction values. These measurements are obtained with Ettus B210 USRP SDR and; for a fixed 12 dBm transmit power of source node and an RF isolation ≈ 62 dB at the relay node. In each run, for an optimal offset value ε, the received signal around −50 dBm is suppressed close to −87 dBm, roughly 7 dB above the receiver's noise floor (−94 dBm). With the worst offset correction value, the residual signal strength can go as high as −67 dBm, roughly 20 dB more than the maximum achievable digital domain suppression values.

impact of offset correction on the residual LSI signal. It is worth mentioning here that the offset calibration is only done once, and the task is completed during the training transmissions. Afterward, the estimated offset does not change, and thus, the employed iterative calibration does not contribute towards additional overhead.

3.4.1.3 LSI Reconstruction

The reconstruction block first converts the PDU message containing re-encoded samples x_r into streaming samples and then filters them with the obtained LSI channel estimate $\hat{\bar{h}}_{rr}[i]$ to produce approximate looped SI samples $\hat{I}_r[i]$.

3.4.1.4 Signal Synchronizer

The synchronizer block synchronizes the reconstructed LSI samples $\hat{I}_r[i]$ with the received samples $y_r[i]$ (which in-fact are the received LSI samples) during training transmissions, and compensates for any delay τ'. Since the fed back known samples $x_r[i]$ arrive earlier compared to the received LSI samples, the synchronizer starts buffering the reconstructed samples and waits for an SoP indicator to release them. Also, the synchronizer block computes the required buffer length during the training session, i.e., no transmissions from the source. Once the buffer length is determined it does not change because the delay from relay Tx to Rx remains the same.

After synchronization, the reconstructed relay forwarded samples $\hat{I}_r[i-\tau']$ are subtracted from the received samples and pushed to the relaying module, given that the training period is finished. The relaying module implements both AF and DF schemes, and a debugger is also there to acknowledge both the packet reception and decoding at the relay node. Figure 3.10 shows the implemented LSI cancellation and the DF modules in GNU Radio.

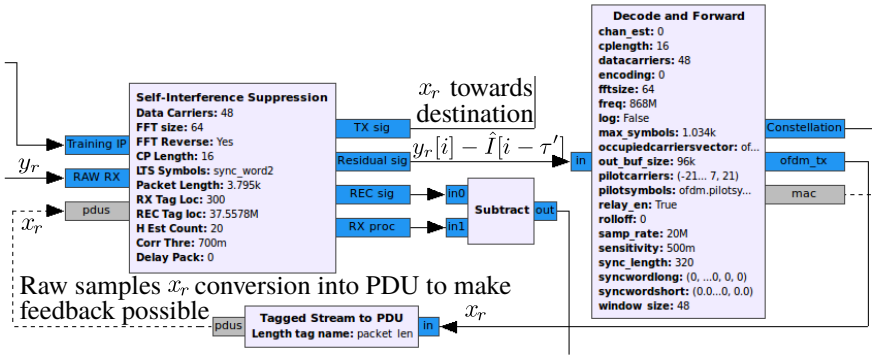

FIGURE 3.10 – Most relevant modules of our FDR implementation for the DF scheme in GNU Radio Companion, © 2019 IEEE [88].

3.4.2 Passive Suppression

In our FDR systems, passive suppression is employed to suppress the direct/leaked SI signal, shown in Figure 3.2. As both Tx and Rx front ends are quite close, the looped-back SI signal is significantly stronger than the SoI arriving from a distant source, and if not suppressed to an extent, it can occupy the whole dynamic range of ADCs in the received signal process path. Therefore, the passive suppression stage is quite crucial. Different designs have been proposed for passive suppression [47], [49], [91], where an RF isolation of up to 73 dB is shown to be achieved.

In this work, to achieve passive suppression of the direct/leaked LSI component at the relay node, we have employed the fundamental antenna isolation approach, which provides a passive suppression of approx. 62 dB. We placed an aluminum foil wrapped Balsa foam between the receiving and forwarding dipole antennas for the isolation of on-board Tx–Rx front-ends within a USRP, as shown in Figure 3.11. Even though the approach does not sound efficient but, considering the available resources, it has worked well enough to test, validate and evaluate the performance of our GNU Radio-based IEEE 802.11a/g/p compliant real-time FDR implementation. It is important to mention here that the employed passive suppression technique in this thesis provides the lower bound of the achievable performance and can be very easily replaced with high-end and sophisticated passive suppression and active analog cancellation approaches such as [72], [84], [91], and; it is certainly not the primary focus of this thesis.

FIGURE 3.11 – Very simple passive suppression approach that isolates the Tx–Rx front-ends.

3.5 Simulative Performance

To draw a performance comparison between AF and DF relaying schemes in both HD and FD modes, we conducted an extensive set of real-time simulations. We investigated the impact of key parameters, i.e., the amplification factor and residual LSI, on the performance of our relaying system. The work focuses more on the DF relaying scheme, as we have already seen the poor performance of AF relaying both analytically and in simulation. Thus, we additionally analyzed the impact of residual LSI on both spectral efficiency and physical layer latency and obtained a performance comparison with traditional DF-based HDRs.

3.5.1 Simulation Setup

In our simulation setup, we transmitted 100 packets for each Modulation and Coding Scheme (MCS) as listed in Table 3.1, and measured the PDR based on received SNR. Each packet comprises of 250 B payload, 3 B header, and 4 B Cyclic Redundancy Check (CRC). For each SNR point, the packets transmission is repeated 20 times to obtain a 95 % confidence interval, which for the sake of clarity, is not shown in the plots. For fair comparison in both transmission modes, we empirically chose the optimum value of amplification factor ($\alpha \approx 10$) and; kept the average transmit power for path relay-destination same, i.e., $P_{\text{avg}}^{\text{AF}} \approx P_{\text{avg}}^{\text{DF}}$, in both relaying strategies.

3.5.2 Evaluation Results

The following sections present our real-time simulation results obtained using GNU Radio for frequency selective fading channels.

3.5.2.1 Packet Delivery Ratio (PDR): HDR vs. FDR

Figures 3.12 and 3.13 shows the PDR plots for each MCS at both relay and destination nodes for the two considered relaying strategies in HD and FD transmission modes, respectively. In all the plots, a PDR of 100 % means that all packets have been correctly detected and decoded, and the horizontal dashed line marks 90 % PDR. Here, it is important to mention that the PDR plots in Figure 3.13 (FD transmission mode) are obtained with non-negligible residual LSI.

From the comparison of Figure 3.12 (plots a & c) and Figure 3.13 (plots a & c), it can be seen that the 90 % PDR performance of each MCS at the relay node in both AF and DF relaying strategies is roughly similar. There is a slightly degraded PDR performance in FD mode as compared to HD mode, certainly because of non-negligible residual looped-back SI in the FD case. Additionally, within FD mode, the PDR performances with AF strategy is marginally lower than the DF strategy. This is

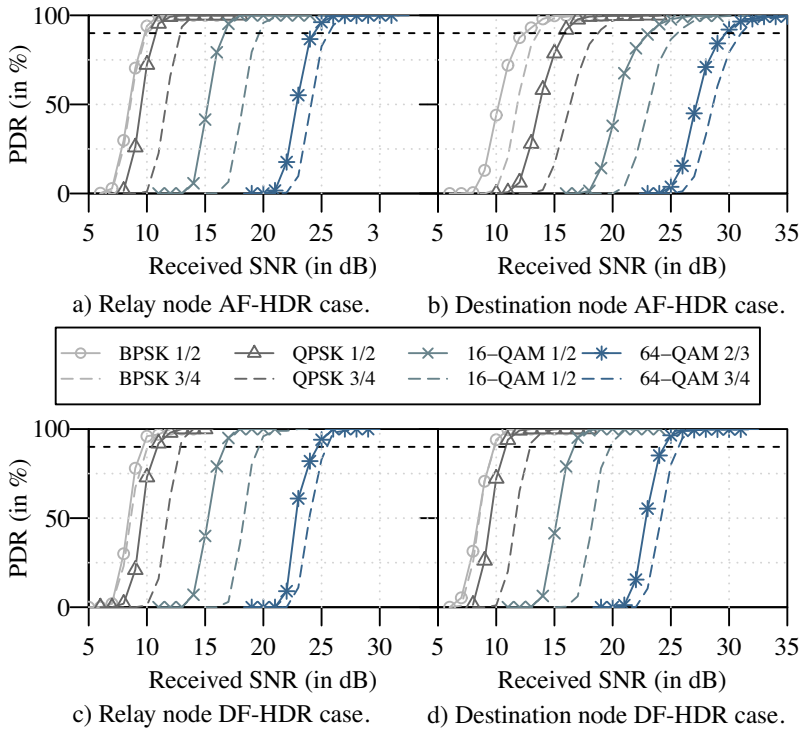

FIGURE 3.12 – PDR versus received SNR at both relay and destination nodes, for $\alpha \approx 10$ in Half-Duplex transmission modes.

due to the negative impact of the amplification factor on the relay node received SNR, as studied in Section 3.3.3.1.

Likewise, by comparing the PDR performances of each MCS at the destination node, Figure 3.12 (plots b & d) and Figure 3.13 (plots b & d), we see that the AF relaying is performing roughly 6 dB – 7 dB worse compared to DF relaying strategy. Even though the PDR performance with AF at the relay node is rather similar to DF in both transmission modes, this is not the case at the destination node. This performance drop is expected with AF relays because of their inherent dependence on amplification factor, which not only requires a critical selection, especially in the FD case, but it also forwards the amplified noise component in the signal received at the relay node.

3.5.2.2 Impact of Amplification Factor in AF Relaying

In Figure 3.14, the impact of the amplification factor on the PDR of each MCS is plotted for the AF-FDR case. It can be seen that for $\alpha > 15$, the PDR of each MCS starts decreasing drastically, and it more or less follow the same trend that we have already seen in the numerical plot shown in Figure 3.6. This is due to the reason that large α intensifies the impact of residual looped SI, which not only reduces the

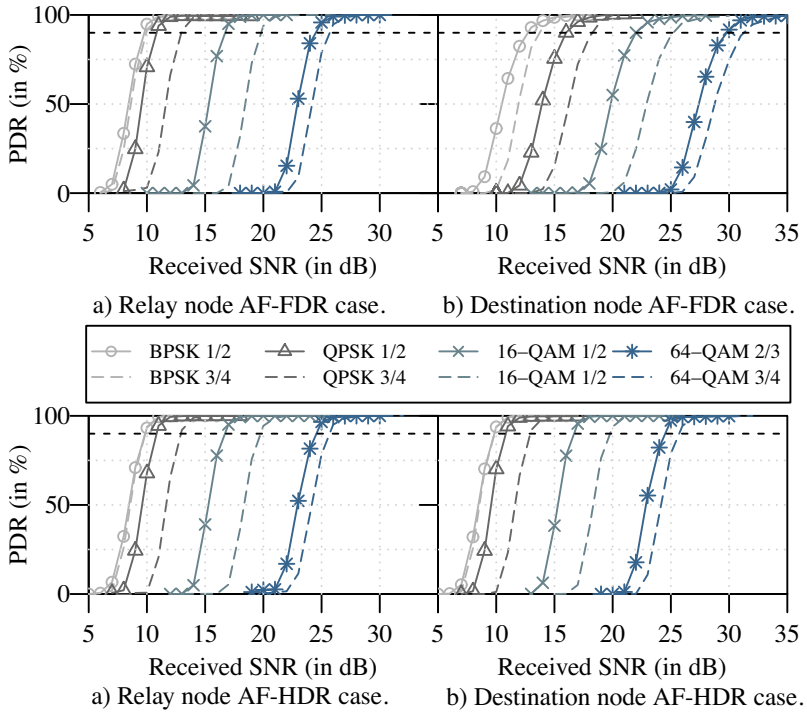

FIGURE 3.13 – PDR versus received SNR at both relay and destination nodes, for $\alpha \approx 10$ and residual LSI ≈ -22 dBm in Full-Duplex transmission modes.

SNR at the destination node but it also negatively affects the SNR at the relay node, as explained in Section 3.3.3.1. Moreover, the PDR of lower-order MCS seems to be affected more at larger α, e.g., for BPSK $1/2$. This is intuitive since the lower-order MCS requires low effective SNR to achieve high PDR and a large amplification factor

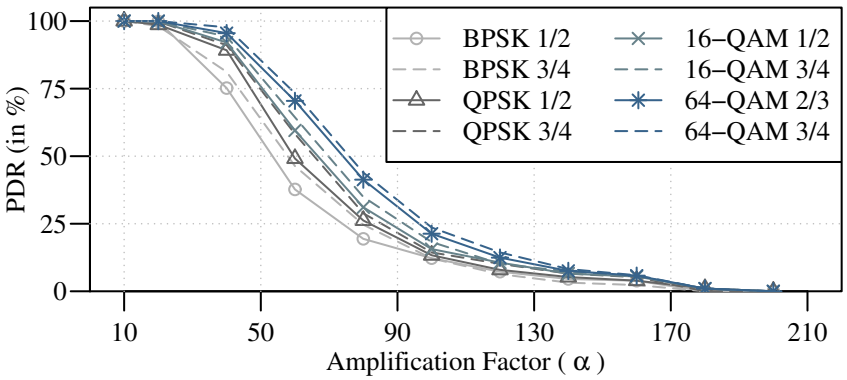

FIGURE 3.14 – PDR versus amplification factor in AF-FDR case, with fixed relay SNR (γ_r) and destination noise power (σ_d^2), © 2019 IEEE [88].

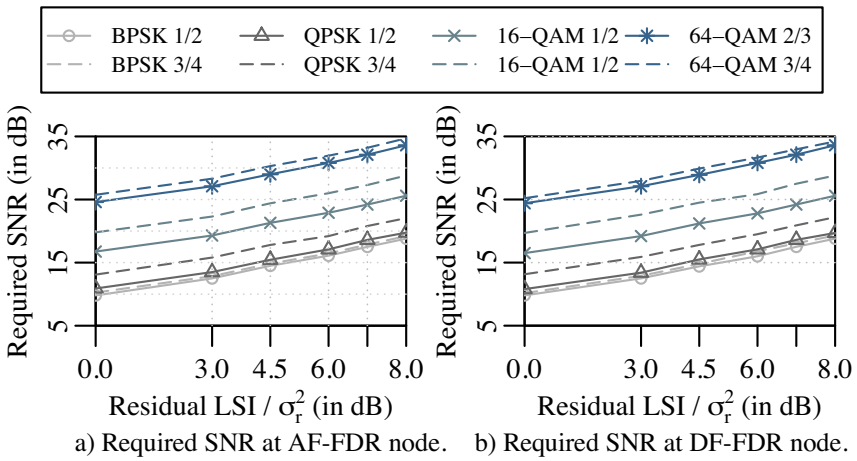

FIGURE 3.15 – Required SNR level for each MCS to maintain 90 % PDR with increasing levels of residual looped-back SI (for $\alpha \approx 10$) at FDR node.

has a more adverse effect on already low γ_r and γ_d, which further aggravates the MCS performance.

3.5.2.3 Impact of Residual Looped SI

Figure 3.15 illustrates the impact of residual looped-back SI on the performance of each MCS in both AF and DF full-duplex relaying. The vertical-axis in the plot shows SNR levels required to maintain a 90 % PDR at the relay node for exceeding residual LSI levels over the noise floor. In the figure, we observe that when residual LSI surpasses the noise floor, more SNR is required to retain the 90 % PDR. This is rather expected since looped-back SI is nothing but interference for the SoI, which means any residual LSI above the noise floor basically reduces the desired signal's SNR. Thus, in order to maintain the PDR performance, more SNR is required. Additionally, it can be noticed that the relation between required SNR and residual LSI is almost linear; take 64-QAM 3/4 as an example, where the required SNR raised from 25.5 dB – 34.5 dB for an 8 dB gain of residual LSI over noise floor. This is due to the reason that the implemented LSI channel (h_{rr}) has linear behavior, and therefore, the resultant LSI and the residual LSI after suppression are also linear in nature.

3.5.2.4 Achievable Spectral Efficiency: HDR vs. FDR

Figure 3.16 compares the achievable spectral efficiency in both HDR and FDR systems with increasing received SNR. In a typical IEEE 802.11a/g based HD system, the maximum achievable spectral efficiency is 2.7 bps/Hz with 54 Mbit/s links. In our HDR implementation for IEEE 802.11a/g standard, the spectral efficiency improves with SNR, and it gets saturated at 2.7 bps/Hz with 64—QAM 3/4 MCS, i.e., 54 Mbit/s

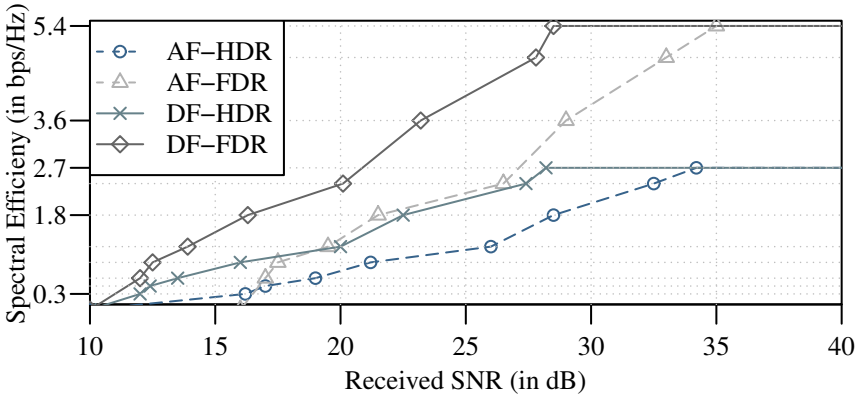

FIGURE 3.16 – Spectral efficiency comparison with both AF and DF relaying strategies, operating in HD mode and; in FD mode with non-negligible residual LSI, © 2019 IEEE [88].

link, in both relaying strategies. Nevertheless, the AF relaying strategy requires roughly 6 dB – 7 dB more SNR to attain similar bps/Hz compared to DF relaying strategy.

In contrast, because of the simultaneous reception and transmission capability of our FDR system, it is providing a two-fold increase in achievable spectral efficiency, i.e., 5.4 bps/Hz, with both relaying strategies. However, the AF strategy needs an additional 7 dB SNR to reach the same bps/Hz performance compared to the DF strategy. Additionally, it can be gathered from the figure that for SNR levels up to 28 dB, it is better to use the DF-HDR system because of its rather similar performance and relaxed processing requirements than the AF-FDR system. Moreover, if AF relaying is an absolute requirement, even then, the deployment of AF-HDR is economically and performance-wise more beneficial for low data-rate links such as 6 Mbit/s and 9 Mbit/s as compared to the AF-FDR system. In conclusion, the DF-based FDR system seems to be the ultimate choice with the best bps/Hz performance, provided that the residual LSI is close to the noise floor.

3.5.2.5 Physical Layer Latency (PLL): HDR vs. FDR

Figure 3.17 indicates the physical layer latencies introduced by each relaying strategy in HD and FD transmission modes. Here, PLL is the time interval a payload engages while traversing from source to destination. In our relay system implementation, the AF strategy does not introduce any delay in both HD and FD mode. However, due to the decoding and re-encoding process involved in the DF strategy, a 150 ns delay is introduced in both modes, which is negligible compared to the considered payload size, as can be seen in Figure 3.17.

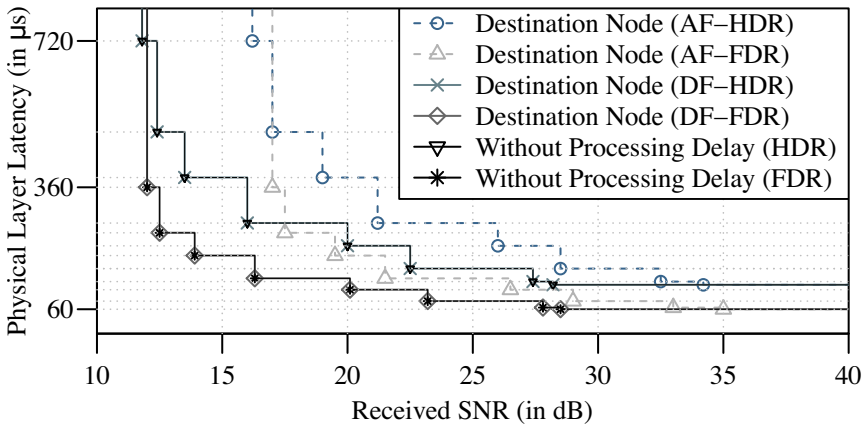

FIGURE 3.17 – Physical layer latency comparison with both AF and DF (with and without decoding delay) relaying strategies, operating in half-duplex and full-duplex modes, © 2019 IEEE [88].

Additionally, it can be noticed in the figure that AF relaying strategy in both HD and FD modes requires roughly 7 dB more SNR to offer similar PLL performance as compared to its DF counterpart. Moreover, unlike the case of spectral efficiency, AF-FDR seems to completely outperform AF-HDR in-terms of low latency requirements. Nevertheless, DF-HDR is still offering better PLL compared to AF-FDR at lower SNR levels of up to 16.5 dB. In essence, DF-FDR outclassed all other relay implementations. For a 250 B payload, it landed-with the maximum latency of 360 µs with the least SNR of 12.3 dB supporting 6 Mbit/s link only and offered the best latency of 60 µs at 28 dB SNR with a 54 Mbit/s link.

3.5.2.6 Impact of Residual LSI: Only DF Relaying

Figure 3.18 illustrates the impact of residual LSI on the performance of each MCS in DF-FDR. The vertical-axis in the plot shows SNR levels required to maintain a 100 % PDR at the relay node for exceeding levels of residual LSI over the noise floor. In the figure, we see that when residual LSI (starting from 0 dB) surpasses the noise floor (maximum by 8 dB), more SNR is required to retain the 100 % PDR at the relay node. This is rather expected since LSI is nothing but interference for the SoI, which means any residual LSI above the noise floor basically reduces the desired signal's SNR. Thus, in order to maintain the PDR performance, more SNR is required. Additionally, it can be noticed that the relation between the required SNR and residual LSI is almost linear. Take 64-QAM 3/4 as an example, where the required SNR raised from 27.5 dB – 36 dB for an 8 dB gain of residual LSI over the noise floor. This is due to the reason that the implemented LSI channel (h_{rr}) has linear behavior, and

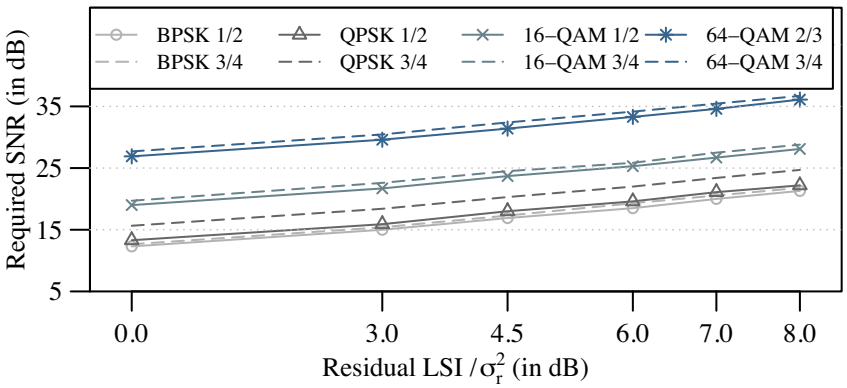

FIGURE 3.18 – Required SNR for each MCS to maintain 100 % PDR with increasing levels of residual LSI in DF-based FDR.

therefore, the resultant LSI and the residual LSI (after suppression) are also linear in nature.

3.5.2.7 Achievable Spectral Efficiency: Only DF Relaying

Figure 3.19 compares the achievable spectral efficiency in both HDR and FDR systems with increasing received SNR. For a typical IEEE 802.11a/g/p based HD systems, the maximum achievable spectral efficiency is 2.7 bps/Hz, which, depending on the sampling frequency, translates to a 54 Mbit/s link for 802.11a/g and a 27 Mbit/s link in the case of 802.11p. In the figure, it can be seen that the spectral efficiency improves with SNR and gets saturated at 2.7 bps/Hz with 64-QAM 3/4 MCS for both HD and FD relays. However, in FDR, with exceeding levels of residual LSI over the

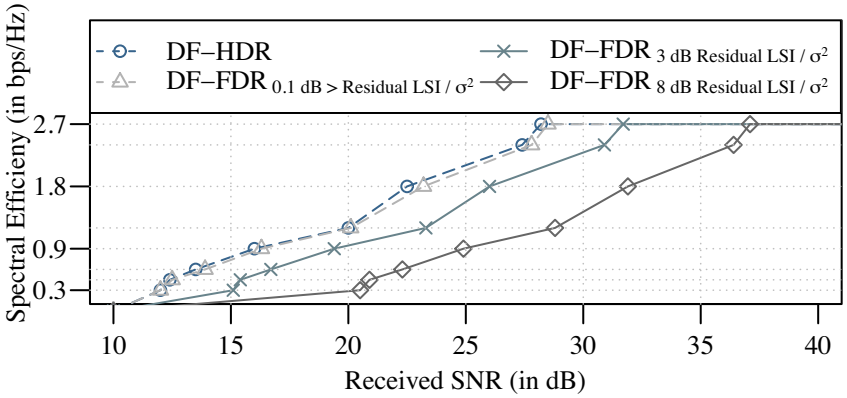

FIGURE 3.19 – Spectral efficiency with the DF relaying scheme, operating in both HD and FD modes. However, for FD mode, different magnitudes of residual LSI over the noise floor are considered.

noise floor (i.e., 3 dB and 8 dB), higher SNR is required to reach a similar bps/Hz performance as compared to DF-FDR $<$ 0.1 dB case. In conclusion, the DF-based FDR is offering roughly similar bps/Hz as DF-HDR, provided that the residual LSI is close to the noise floor, and these results are in line with what has been reported in the literature. It is also worth mentioning here that since a relay node receives and forwards the same information, therefore, there are no relative spectral gains with full-duplex relaying, as opposed to basic FD systems that can transmit and receive different information at the same time and frequency. This maximum relative spectral efficiency an FD relay can achieve is the same as an HD relay.

3.5.2.8 Physical Layer Latency (PLL): Only DF Relaying

Figure 3.20 indicates the physical layer latency introduced by DF relaying scheme in both HD and FD transmission modes. Here, PLL is the time interval a payload engages while traversing from source to destination. A DF relay has to decode the frame header, which is required for the decoding and re-encoding of the entire packet. In standard IEEE 802.11 frame structure (see Figure 3.5), the frame header is the fifth symbol. This means that the relay node has to wait for 400 samples (80 samples per symbol) for the decoding and re-encoding process, which translates to a fixed delay of 20 µs with a 20 MHz sample rate. This delay exists regardless of FD or HD mode, and therefore its impact is not evaluated.

In the figure, it can be seen that even though the bps/Hz performance in FDR with higher residual LSI levels, i.e., 3 dB and 8 dB, is much worse compared to HDR, the computed PLL is much lower. It is because of the simultaneous reception and transmission capability of an FDR, which, as a result, reduces the end-to-end latency of the system. For the received SNR over 15 dB and 25 dB, even the 3 dB

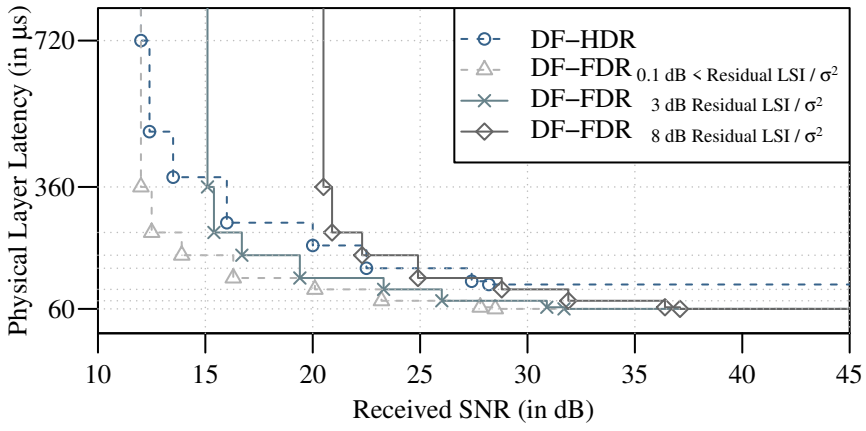

FIGURE 3.20 – Physical layer latency with the DF relaying schemes for different magnitudes of residual LSI over the noise floor.

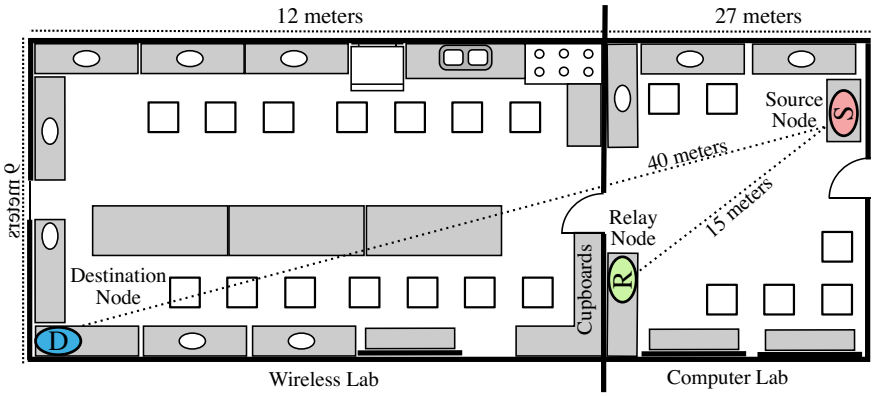

FIGURE 3.21 – Indoor NLoS experimental settings floor plan. For LoS experiments (floor plan not shown here), all three nodes were placed in the wireless lab.

and 8 dB residual LSI cases are outperforming DF-HDR, respectively. These results demonstrate the superior performance of FD relaying in terms of end-to-end latency, even for higher levels of residual LSI.

3.6 Experimental Performance

3.6.1 Experimental Setup and Discussion

We have conducted detailed indoor experiments for real-world performance evaluation of the presented IEEE 802.11a/g/p standard-compliant FDR implementation. We used three B210 USRP–SDRs in the experiments as the source, relay, and destination nodes. The floor plan for the indoor experimental setup is illustrated in Figure 3.21. The presented FDR implementation is evaluated in two types of experimental settings, i.e., NLoS and LoS. Unless mentioned explicitly, the discussion mainly focuses on the NLoS results as the channel conditions are more complex and degrading – providing better insights. The source node transmits 100 packets per transmission, where every individual packet contains 3 B header, 250 B payload, and 4 B CRC. For each case, the transmissions are repeated 10 times for every MCS and with different transmit power levels. The most relevant parameters for the measurements are listed in Table 3.2.

In our experiments, 20 training packets (i.e., $C_k = 20$ transmissions) are used to estimate the relay node LSI channel and for FFT offset correction simultaneously. These training packets only contain Short Training Sequence (STS) and LTS symbols embedded in the WLAN packet structure for estimation. How frequently such training transmissions are needed largely depends on a fully functional MAC protocol, and they basically define the additional overhead due to training. Nevertheless, these

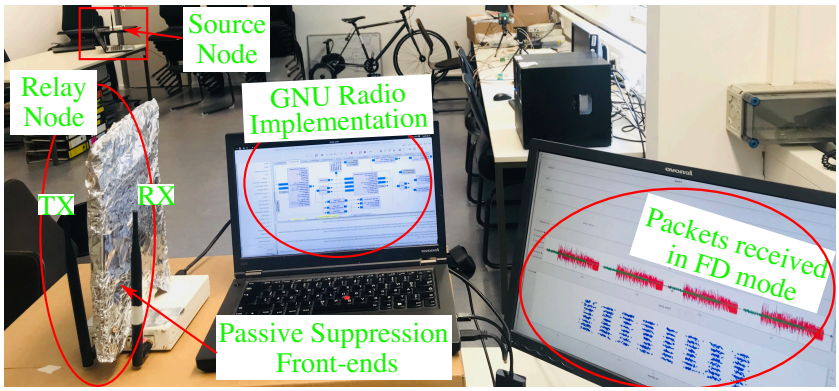

FIGURE 3.22 – Image of our working indoor experimental setup.

overheads are typically small. For example, an IEEE 802.11 standard compliant training packet (see Figure 3.5) includes two STS and LTS symbols each, i.e., $80 \times 4 \times 20 = 6400$ samples are required. For a naive assumption of 10 ms training frequency and 20 MHz standard sample rate, the gross overhead due to training transmissions is only 3.2 %. If the training is required every 100 ms, then the overhead is only 0.32 %. As stated before, the exact overhead calculations depend on the considered MAC protocol and lie outside the scope of this thesis.

Additionally, in the experimental study, we have evaluated FDR with Decode and Forward (DF) scheme only. We dropped measurements for Amplify and Forward (AF) scheme because of its degraded analytical and simulative performance; and due to the feedback loop instability at higher amplification factors. At this point, it is worth stating that since decoding delay in DF relaying scheme is the same regardless of HD or FD transmission mode; therefore, its impact is not studied here. The working hardware setup for FDR evaluation is shown in Figure 3.22. The setup image indicates the transmitting source node, the relay node, the executed GNU Radio implementation, and the real-time SoI in green (after LSI suppression) with the resultant decoded constellation for 64-QAM 3/4 MCS.

Table 3.2 – Hardware specific parameters in the case of NLoS experiments.

Carrier Frequency	868 MHz
Sampling Frequency	2 MHz (limited CPU processing power)
Receiver's Noise Floor	−94 dBm
S–R Distance	15 m
S–D Distance	40 m
RF Isolation	approx. 62 dB
Digital LSI Suppression	up-to 39 dB
Receiver Gain	30 dB

Finally, as discussed previously, GNU Radio is a GPP-based framework; this essentially means that the supported real-time bandwidth of USRPs is directly dependent on the CPU compute power. The results obtained here are with a 4^{th} generation Intel® core i5 processor and 8 GB memory. Here, it is also worth pointing out that two RF chains were working in parallel for receiving and forwarding because of FD relaying mode, i.e., twice the amount of data to be processed. With this setup, we can achieve 2 MHz of real-time bandwidth with the USRPs instead of established 10 MHz or 20 MHz in IEEE 802.11a/g/p standard. This constraint on the USRPs' operational frequency is due to the limited processing power of the used fixed-architecture-based 4-core GPP CPU and the capacity of the USB 3.0 port that translates the samples from GNU Radio to the USRP. This is very much unlike FPGAs, which have a dynamic architecture and inherent parallelism [92], and where a typical Xilinx Virtex-7 FPGA is about 4.2 times faster than a 16-core GPP [93].

This real-time bandwidth can certainly be improved by using a powerful machine and assigning dedicated memory and CPU cores to the GNU Radio framework by tweaking with the Linux Kernel and by twiddling with the GNU Radio scheduler. It is worth pointing out here that in the real-time experiments, to avoid interference from WiFi devices and other wireless systems operating in the ISM band, we have used the 868 MHz frequency band instead of the defined 2.4 GHz and 5 GHz bands.

3.6.2 Evaluation Results

The following sections present and discuss our real-time experimental results with SDRs in an indoor environment for both LoS and NLoS cases.

3.6.2.1 Real-time Cancellation: NLoS Case

A screenshot of real-time LSI cancellation with 8 dBm transmit power level of the relay node is shown in Figure 3.23. The figure shows the cancellation performance during training transmissions, i.e., no transmissions from the source node. For clarity, we only show the cancellation performance with real samples, i.e., the in-phase component. The signals in red, blue, and green represent received LSI, reconstructed LSI, and residual LSI (in mV), respectively.

Likewise, the screenshot shown in Figure 3.24 presents the real-time LSI cancellation during the reception of both the Signal-of-Interest (SoI), i.e., transmissions from the source node, and LSI due to relay node forwarding. Again, for visibility reasons, cancellation with only real samples, i.e., the in-phase component, is presented. The signals in red, blue, and green are received (LSI & SoI), reconstructed LSI, and (residual LSI & SoI), respectively.

The hardware setup in Figure 3.22, also demonstrates the real-time cancellation performance at the relay node while receiving SoI from the source node, and the

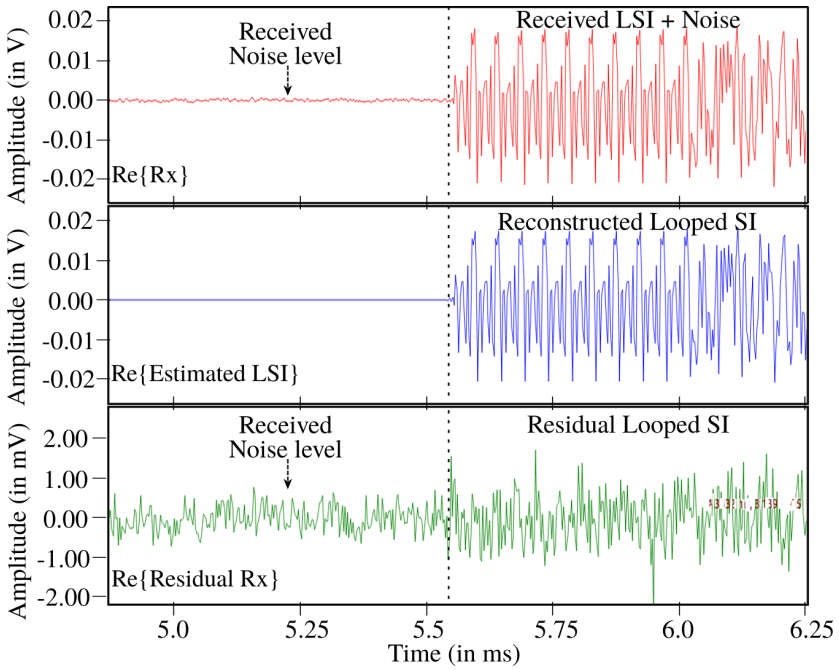

FIGURE 3.23 – Snapshot of real-time LSI cancellation performance of our relay node in FD relaying mode during training transmissions, i.e., no transmissions from the source node.

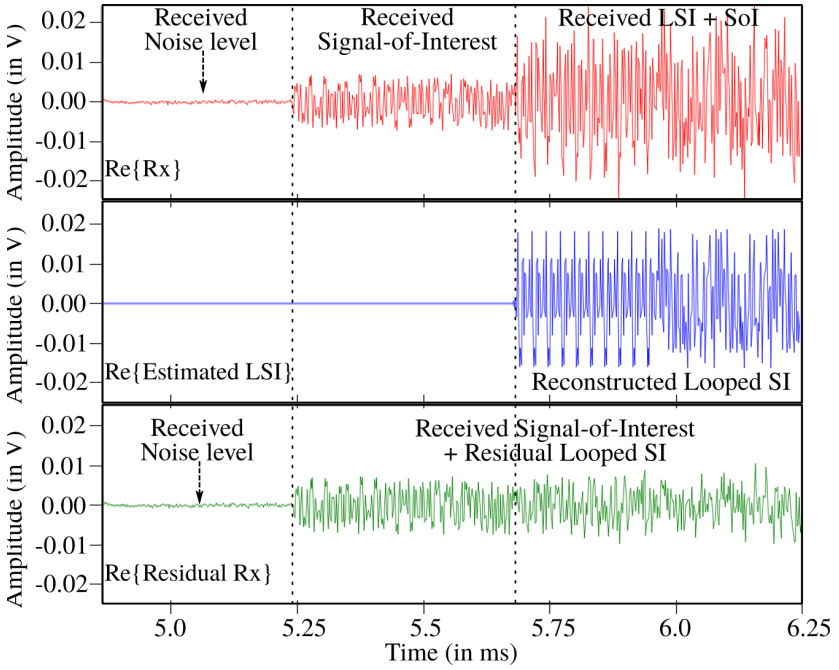

FIGURE 3.24 – Snapshot of real-time LSI cancellation performance in FD relaying mode, during relaying operation, i.e., in the presence of SoI from the source node and LSI.

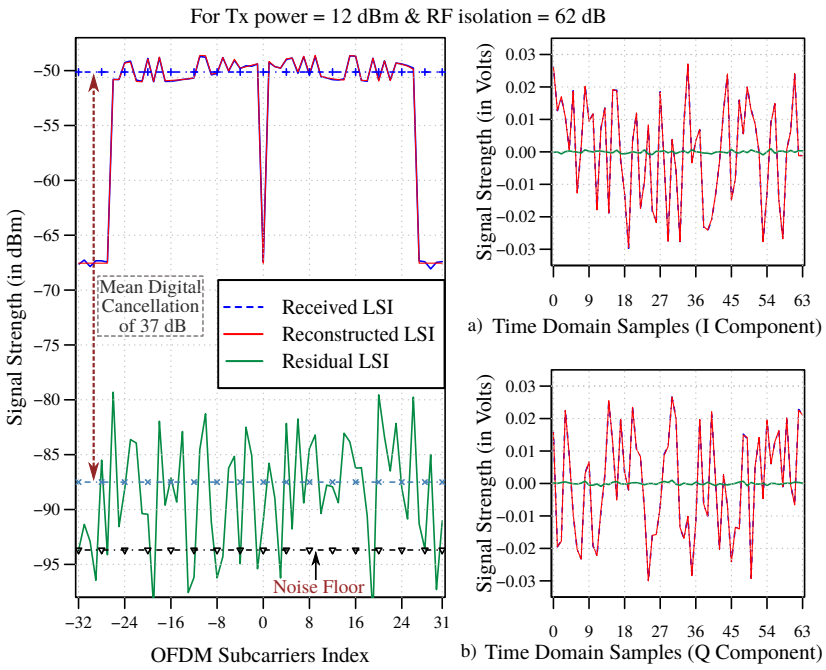

FIGURE 3.25 – Cancellation per OFDM symbol: (a) In the frequency domain, (b) & (c) In the time domain, I–Q samples.

resultant received constellation of 64-QAM 3/4 packets after LSI suppression at the relay node. The signal in red is the combined received LSI and SoI, and the signal in green is the SoI, including the residual LSI after suppression.

Similarly, Figure 3.25 presents the per OFDM symbol cancellation plot at the relay node for a transmit power of 12 dBm and an RF isolation of approx. 62 dB. The received LSI symbol in Figure 3.25(a) of approx. −50 dBm mean strength is suppressed close to −87 dBm, i.e., approx. 37 dB mean digital cancellation and roughly 7 dB above the noise floor. In the plot, the waveforms in blue, red, and green are received the LSI symbol, reconstructed LSI symbol, and residual LSI, respectively.

3.6.2.2 LSI Suppression at Relay Node: NLoS Case

The achieved digital domain LSI cancellation with our FDR implementation is presented in Figure 3.26 for increasing transmit power levels. For B-210 USRP SDRs, the noise floor measured at a sampling frequency of 2 MHz is close to −94 dBm, i.e., the red plot. From the figure, it can be gathered that with low power transmissions (up to −12 dBm), the received LSI is suppressed very close to the receiver's noise floor. At the same time, a non-linear increase in the residual LSI strength is measured at high power transmissions because of the following reasons.

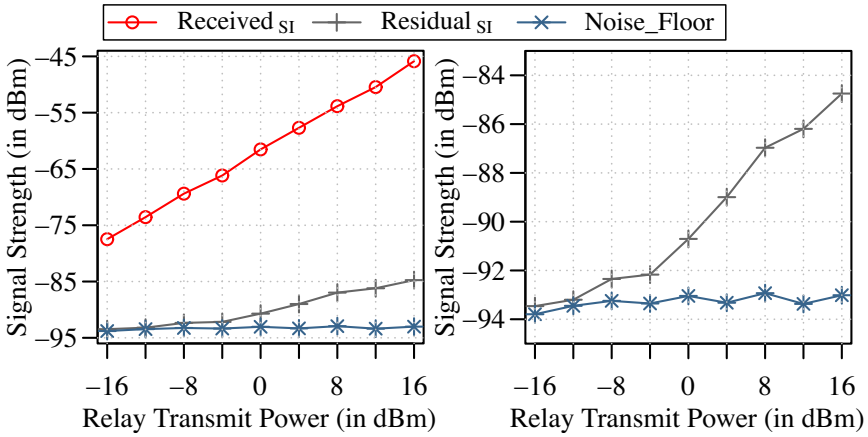

FIGURE 3.26 – The digital domain LSI suppression performance of the presented FDR implementation for increasing levels of transmit power at the relay node.

Firstly, at higher power transmission, the non-linear factor incurred by the transmit chain amplifier becomes more significant, resulting in increased strength of the non-linear LSI component. Secondly, the obtained 62 dB RF isolation is not insufficient (reported as high as 73 dB in the literature), and with higher power transmissions, this inadequate isolation becomes more evident. By further incorporating the non-linear LSI component modeling and introducing sophisticated passive suppression approaches, such as dual-port dual polarized slot coupled antenna, this residual LSI can be mitigated even for higher transmit power levels at the relay node.

3.6.2.3 Packet Delivery Ratio (PDR): NLoS Case

The PDR obtained in our measurement campaign for each MCS at the relay node – operating in both FD and HD modes is demonstrated in Figure 3.27. In the figure, the title of each plot lists the operational mode and the transmit power level (more relevant for FD case) of the relay node. In every plot, a PDR of 100 % means that all packets have been correctly detected and decoded. The horizontal dashed line specifies the 90 % PDR level. For clarity reasons, the 95 % confidence intervals are not shown in the plot.

The PDR plots in the figure are relatively similar for HD and −4 dBm FD modes. There is a small difference of approx. 1 dB in the performance for each MCS, certainly because of the non-negligible residual LSI discussed previously. The PDR performances for each MCS at 0 dBm and 4 dBm FD modes, however, are more degraded. In both cases, comparatively higher source transmit power levels are required to achieve 100 % PDR. This degradation in the performance is due to the fact that a higher transmit power at the relay node intensifies the residual LSI, which raises the noise-plus-interference level for the SoI arriving from the source node.

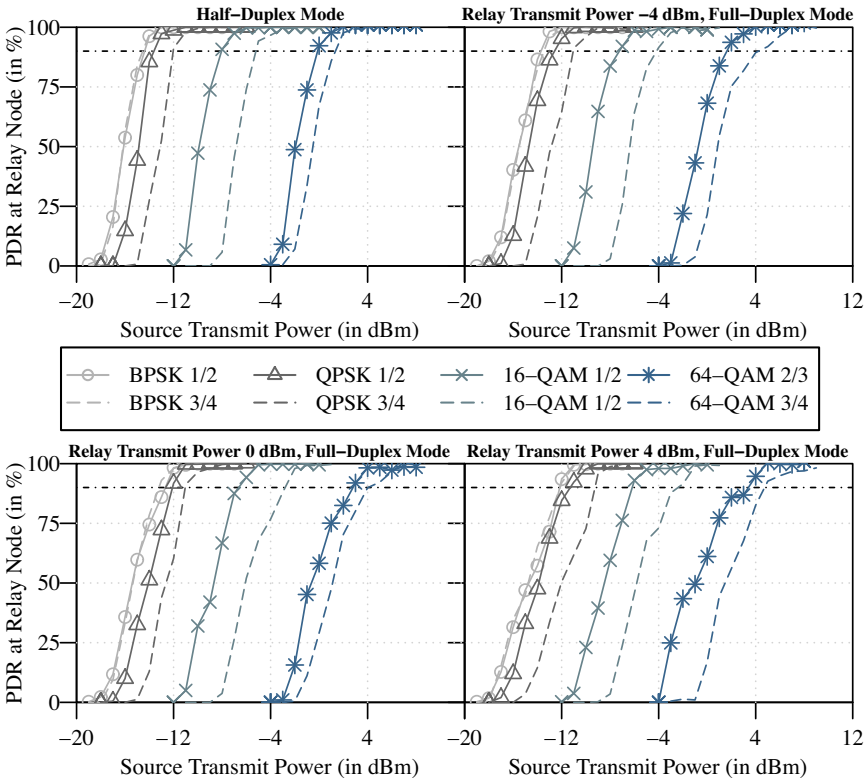

FIGURE 3.27 – Experimentally measured PDR performances for each MCS with DF-based IEEE 802.11 a/g/p compliant HDR and FDR implementations at different relay node transmit power levels.

Therefore, more power is required from the source node such that the SoI overcomes the increased interference level, and 100 % PDR is still maintainable. Additionally, it is worth observing here that the linear-SNR vs. residual LSI behavior, which we measured in simulative evaluation Section 3.5.2.6, is no longer valid, essentially due to the non-linear nature of the residual LSI, as depicted in Figure 3.26.

Furthermore, if we look into the relative sensitivity levels obtained for each MCS by choosing BPSK 1/2 as a reference scheme, it can be seen that these relative sensitivity levels meet the levels provided in the 802.11.[2] For example, considering the sensitivity level provided in the *802-11ac-receiver-minimum-input-sensitivity-test* for BPSK 1/2 as a reference, the additional gain required by 64-QAM 3/4 is $(-65\,\text{dBm} - (-82\,\text{dBm}) = 17\,\text{dB})$. Now, in our results (Figure 3.27), it can be seen that roughly 17 dB more power is required from the source node for 64-QAM 3/4 to achieve similar PDR performance as that obtained with BPSK 1/2, regardless of the residual LSI that is effecting all the modulation and coding schemes rather equally. Here, it is worth stating that the precise sensitivity levels depend on the receiver's

[2] `https://uk.mathworks.com/help/wlan/examples/802-11ac-receiver-minimum-input-sensitivity-test.html`

noise floor, which is influenced by the receiver's noise figure and SDR front-end calibration, and it is rather hard to achieve exact minimum sensitivity. Nevertheless, the relative sensitivity values with our implementation meet the 802.11 standard requirements.

3.6.2.4 Impact of Residual LSI on PDR: NLoS Case

Figure 3.28 demonstrates the required transmit power from the source node to maintain a 100 % PDR at the relay node for each MCS. In the plot, the dashed vertical line separates the FDR and HDR performances. Ideally, with full LSI suppression, the transmit power requirement from the source node in the FDR case should match HDR power requirements. However, the non-linearly increasing demand for more source power (in FDR) at higher relay node transmission power is because of the growing residual LSI. This, as a result, increases the noise-plus-interference level for the SoI, and a higher transmit power is required from the source to maintain the 100 % PDR. These results are also in-line with the simulation study (Figure 3.15); the only difference is that in simulations, the SNR requirements are linear (due to linear residual LSI), whereas, with hardware experiments, the source power demand is non-linear because of the already mentioned reasons in Section 3.6.2.2. We would like to point out here that the presented system utilizes a straightforward RF isolation approach, and no cancellation in the analog domain is implemented. The results presented here essentially show the lower bound of the system's performance.

Also, the required source transmit power to maintain 100 % PDR at the relay node directly relates to the residual LSI indicated in Figure 3.26. Since the implementation is based on an open-source framework, further research with more sophisticated

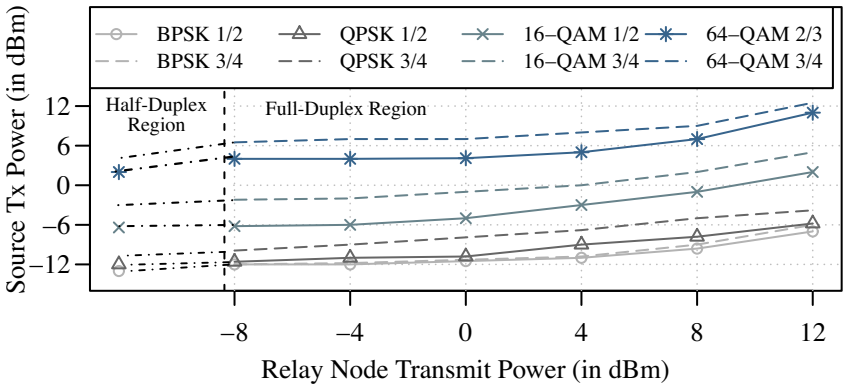

FIGURE 3.28 – Required source transmit power levels to maintain 100 % PDR with each MCS at the relay node for a given relay transmit power in NLoS scenario. The half-duplex PDR performance is independent of relay transmit power levels due to time separate transmissions and receptions.

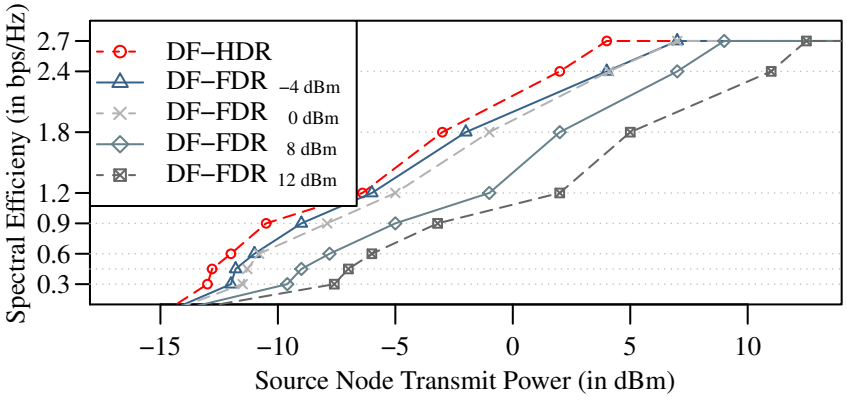

FIGURE 3.29 – Spectral efficiency comparison of HD relaying with FD relaying for various transmit power levels of the relay node in FD case.

suppression approaches can easily be built upon the current implementation to optimize the system's performance.

3.6.2.5 Achievable Spectral Efficiency: NLoS Case

Figure 3.29 compares the measured spectral efficiency of HD and FD relaying in our experimental setup. The four FDR plots in the figure are obtained with different transmit power levels of the relay node. It can be seen that the achievable spectral efficiency gets worse at higher relay transmit power. This necessarily is because of the increased magnitude of residual LSI at higher power. Also, the bps/Hz performance degrades non-linearly from low to high power levels of the relay node, certainly because of the non-linear nature of residual LSI. Additionally, these results follow a similar capacity degrading trend with increasing residual LSI as observed previously in the analytical and simulative study.

Furthermore, the results here clearly demonstrate that the presented implementation achieves the maximum bps/Hz performance established for IEEE 802.11a/g/p with 64-QAM 3/4 MCS in both HD and FD relaying modes. At the same time, they also confirm that for optimal performance and to fully utilize the entire dynamic range of the relay node transmit power in full-duplex mode, the residual LSI needs to be suppressed close to the receiver's noise floor.

3.6.2.6 Physical Layer Latency (PLL): NLoS Case

Figure 3.30 outlines the minimum achievable PLL comparison with HD and FD relaying in our experimental measurements. It is important to mention here that the delay due to the software-to-hardware translation of samples, the Tx–Rx front-ends, and the propagation is the same regardless of HDR and FDR implementation;

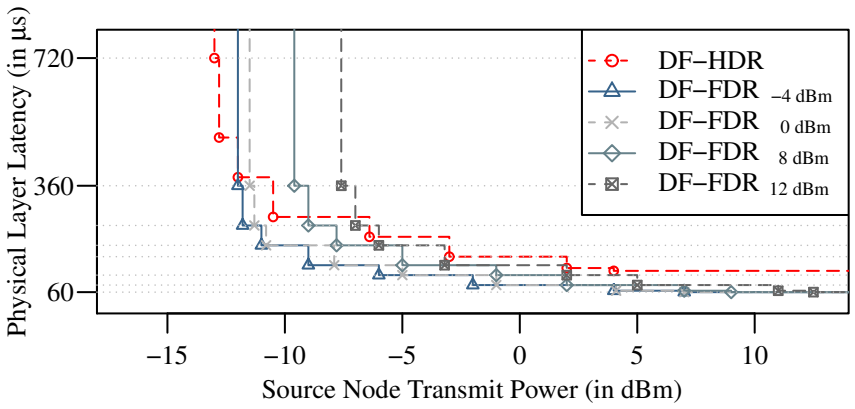

FIGURE 3.30 – Achievable physical layer latency over the two-hop relaying system in HDR and FDR configurations, with different relay node transmit power levels in the FDR case.

therefore, they are not considered here. From the figure, it can clearly be seen that the PLL decreases with higher transmit power from the source node. The PLL depends on the packet size, or more precisely, the number of samples sent per packet, and the decoding delay of the DF scheme. The hardware delay (in the order of a few samples) is not evaluated here. With a higher Tx power resulting in a better received SNR, higher-order modulation-coding schemes defined in the IEEE 802.11 standard (from BPSK 1/2 to 64-QAM 3/4) can be adopted. This means the same number of bytes (the original packet) can be encoded in fewer symbols and, therefore, fewer samples to transmit (i.e., a reduced transmission time). This reduces the physical layer latency, but at the expense of more transit power.

Additionally, It can be gathered from the figure that although HDR starts receiving the packet roughly 1 dB before FDR, i.e., −12.1 dBm; however, the minimum PLL drops down much faster with FDR. Even at higher relay node transmit power with most residual LSI magnitude, take DF-FDR$_{12\text{ dBm}}$ as an example, where for the same source transmit power (−6 dBm and above), FDR has lower PLL as compared to HDR. These results conclusively highlight the possible gains with full-duplex relaying in-terms of lower end-to-end latency, which further improves with better LSI suppression.

3.6.2.7 Packet Delivery Ratio (PDR): LoS Case

To conclude our experimental evaluation, these final results present the real-time performance of our standard-compliant FD relaying in the LoS scenario. Here, all the three nodes, i.e., source, relay, and destination nodes, are placed in the same Wireless Lab with floor plan shown in Figure 3.21. Low transmission powers are used in these measurements at both source and relay nodes due to the shorter

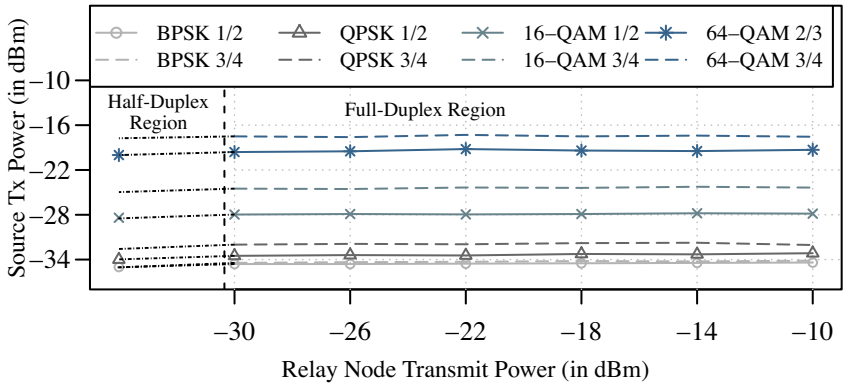

FIGURE 3.31 – Packet Delivery Ratio (PDR) performances of all MCS at the relay node for different transmit power levels in LoS scenario. The half-duplex PDR performance is independent of relay transmit power levels due to time separate transmissions and receptions.

distance between the nodes (S–R distance 12 m, S–D distance 27 m). The rest of the experimental settings are the same as the NLoS case.

Figure 3.31 outlines the transmit power required from the source node for all the IEEE 802.11 defined MCS to maintain 100 % PDR against increasing relay node transmit power. In the figure, it can be seen that due to low transmit powers at the relay end, the impact of LSI is reduced to insignificant. The excessive transmit power required from the source node in the case of FD relaying is roughly 0.5 dB only as compared to traditional HDR. The results obtained here have clearly indicated that in the case of total suppression of LSI, FD relaying can offer the optimal performance.

Additionally, from these results, it can be gathered that in terms of achievable spectral efficiency, the experimental performance of FD relaying in such a setting is very close to HDR, certainly because of close to negligible residual LSI. Intuitively, this has a direct impact on reducing the PLL further as well. These real-world experimental results confirm the simulative findings of the previous works that FD relaying can improve the channel utilization and considerably reduce the PLL as opposed to existing HD-based relaying, provided that the residual LSI is suppressed to the receiver's noise floor.

3.7 Concluding Remarks

Infrastructure relays have the potential to effectively address both the capacity and coverage issues of existing wireless systems. The traditional Time Division Duplexing (TDD)-based Half-Duplex (HD) relay architectures have the added disadvantage of increasing end-to-end delays in a multi-hop relaying system. An in-band full-duplex

relay has the capacity to simultaneously receive and forward, which improves the channel utilization and reduces the latency in a multi-hop network significantly. With many theoretical works available on Full-Duplex Relaying (FDR), standard-compliant implementations for experimentation and evaluation purposes are not widely available, and the existing FDR solutions are still in their prime.

In this chapter, we present the first IEEE 802.11 a/g/p standard compliant GNU Radio-based FDR implementation. Contrary to the earlier works, the proposed FDR implementation supports both real-time simulation and Software-Defined Radio (SDR)-based real-world experimental. We experimentally evaluated the performance of the presented FDR system, in particular, focusing on Decode and Forward (DF) relaying. Even though there is a need for more advanced RF isolation between the two antennas, our system is able to achieve considerably good performance results in an indoor setup. Our results show the potential gains offered by Full-Duplex (FD) relays in-terms of efficient channel utilization and reduced physical layer latency from the system level's perspective. In particular, given that the LSI is sufficiently suppressed, DF-based FDR outperformed the HD relaying systems.

The employed GNU Radio framework supports real-time signal processing, and the same code can be used for both simulations and real-world experiments. The presented IEEE 802.11 compliant FD relaying implementation can also be evaluated in full capacity within the real-time simulation mode, under different channel conditions and impairment sources. Thus, different algorithms to deal with changing channel conditions can be tested in full detail. Furthermore, different Medium Access Control (MAC) layer implementations for FD relaying can also be built upon the current system within GNU Radio and can be coupled with Wireshark (another widely used open-source platform) for analyzing the network protocol at a microscopic level, and that is all in simulations before purchasing expensive hardware. In summary, our system provides the basis for a much-needed toolchain for a complete evaluation of FD relaying from packet-level to physical layer.

Chapter 4

In-band Full-Duplex Relaying Application in Vehicle Platooning

THE Intelligent Transportation Systems (ITS) are changing the way cars will drive in the future and have the primary aim of improving the safety and efficiency of road traffic. Platooning is one of the considered applications of ITS, helping cars to drive with very short safety gaps to improve road traffic capacity and to reduce air drag. A basic building block for such cooperative driving solutions is fast and reliable wireless communication. Typically in vehicle platoons, the information from platoon leader is required to be received at all the following members reliably and with the least communication delays.

In the previous chapter, we thoroughly investigated in-band Full-Duplex Relaying (FDR); and explored its potential in a dual-hop scenario, where the main takeaway is the reduced end-to-end communication delay. Here, we introduce the FDR for use in platooning applications in order to address the fundamental challenge, i.e., additional delays due to multi-hop Half-Duplex (HD)-based relaying via each intermediary vehicle or large interference domains in the case of direct dissemination of messages from leading vehicle.

The rest of the chapter is based on the following peer-reviewed publications:

- **M. S. Amjad, T. Hardes, M. Schettler, C. Sommer, and F. Dressler, "Using Full Duplex Relaying to Reduce Physical Layer Latency in Platooning," in *11th IEEE Vehicular Networking Conference (VNC 2019)*, Los Angeles, CA: IEEE, Dec. 2019, pp. 236–239.**

  In this conference paper, my contributions were: to show the feasibility of full-duplex relaying in vehicular networking applications such as platooning in the sub-6 GHz communication band; implementation of FDR in vehicle platooning scenario; real-time simulative evaluation of communication performance in

all scenarios, i.e., Half-Duplex Relaying (HDR), FDR, and Direct Transmission (DT).

- **M. S. Amjad, M. Schettler, S. Dimce, and F. Dressler, "Inband Full-Duplex Relaying for RADCOM-based Cooperative Driving," in *12th IEEE Vehicular Networking Conference (VNC 2020)*, Virtual Conference: IEEE, Dec. 2020.**

  This conference paper extends the previous work with the following contributions: the first investigative study on RADCOM-based FDR in cooperative driving networks with platooning as a particular use case; the emulation of 77 GHz mmWave channel in GNU Radio framework implementing the platooning scenario; the evaluation and comparison of RADCOM FDR performance over HDR in vehicular platoons.

4.1 Motivation

Platooning is an ITS application that addresses multiple issues in today's road traffic [94], [95]. Vehicles in a platoon autonomously follow each other by keeping a small safety gap (down to only a few meters) with the preceding vehicle. By using such small inter-vehicle gaps, platooning not only increases the effective road utilization and traffic flow; but also reduces the air drag.

To ensure an inter-vehicle gap of only a few meters, platooning requires a reliable wireless communication channel for vehicles to exchange their messages. Presently, sub-6 GHz based technologies, such as WLAN IEEE 802.11p or 4G/5G Cellular V2X, are so far considered for vehicular platooning. A platoon's beacons essentially contain messages providing current status information of a vehicle, e.g., acceleration or speed. The exchange of such messages between vehicles enables the design of Cooperative Adaptive Cruise Control (CACC) systems and allows cooperative driving. The control principle of the CACC exploits the data received from other vehicles within a platoon to conserve the consistent behavior of the platoon as a whole while keeping small inter-vehicle gaps. A periodic message transmission is required for the CACC to work effectively, and the transmission frequency is typically in the order of 10 Hz [96].

RADCOM is an emerging communication method that is also proposed for use in ITS [97]. By dual-purposing existing RADAR detection and ranging systems that operate in the mmWave frequency bands, high bandwidth, and low latency communication is enabled between vehicles on the road. Since such RADAR systems are already common in modern vehicles, the adaptation for communication would be significantly less complex and cheap than integrating additional communication methods. Vehicular platooning can particularly benefit from RADCOM, where,

beyond the basic operation of the platoon, high-bandwidth applications, such as 4k video streaming of the leaders' front cameras to the other platoon members ('see-through' concept), are additionally possible.

A Reliable and low end-to-end latency communication is rather crucial in platooning. The delayed and outdated information about kinematics of preceding vehicles is essentially less useful or even disadvantageous to the safety of the system as the reaction time of the underlying control system increases. Particularly, the properties of the electromagnetic waves in the mmWave spectrum (high directionality, strong Line-of-Sight (LoS) component, and substantially increased available bandwidth) differ from more established ones, i.e., the sub-6 GHz frequencies. This potentially allows the complementary use of both resources, improving the efficiency and reliability of the overall system.

Related studies for platooning [95], [96] use the IEEE 802.11p stack as the fundamental basis for communications. Segata et al. [95] showed that especially real-time safety-critical applications like platooning suffer from high packet loss due to the unreliable Radio Frequency (RF) channel. This packet loss results in a lower update rate of the CACC and leads to an unstable platoon, which can cause vehicle collisions.

To guarantee reliable packet reception, especially at the furthest vehicle in a platoon, very high power transmissions are required from the vehicle leading because of large propagation losses, particularly in mmWaves. This certainly results in an expanded interference domain, affecting the neighboring vehicles on the road, which are not part of this platoon. An alternative to high power transmissions is the use of multi-hop relaying to transport the data from the leading vehicle to the last vehicle. Existing Time Division Duplexing (TDD)-based relays, which have been considered by the wireless standards such as WiMAX and LTE, are half-duplex in nature and require additional resources in the time-domain for reliable communication. Inevitably, such HDR increases end-to-end latency that gets even worse in multi-hop relay scenarios such as in platooning.

Recent works, for example [7], [8], [16], [88], have demonstrated the practicability of Full-Duplex (FD) wireless systems and have shown the potential gains of FD communications. As opposed to HDR, FD relays can receive and forward at the same time and frequency, which essentially reduces the end-to-end latency in a multi-hop relay network. The major bottleneck in FDR is the Looped Self-Interference (LSI), which exists as a result of simultaneous reception and forwarding, illustrated in Figure 4.3. Nevertheless, with the advancements in LSI cancellation techniques, FD communications have become more realistic, and it is even more effective in RADCOM because of high propagation losses in mmWaves that leads to weak reflected LSI and high passive (RF) isolation due to directionality.

In this chapter, we propose FDR in vehicular platooning. The FDR capability to simultaneously receive and forward can further reduce the end-to-end delays in platoons, which essentially means reliable and fast delivery of the time-critical messages that are necessary to keep the desired inter-vehicle gap and to ensure safety. We build upon our GNU Radio-based implementation [88], which is compliant with the IEEE 802.11p standard, and consider a prototypic scenario of a five-vehicle platoon, exchanging messages by means of HDR, FDR, and DT approaches. For evaluation purposes, we consider and compare both the sub-6 GHz channel and 77 GHz mmWave channel. Our first results show the achievable Packet Delivery Ratio (PDR) and Physical Layer Latency (PLL) at the last vehicle for the three use cases.

The core contributions of this chapter can be summarized as follows:

- We investigate full-duplex relaying in vehicular networks and show its feasibility in platooning.
- We further investigate RADCOM-based FDR in cooperative driving networks and show its potential in vehicular platoons.
- We conduct real-time simulations in the open-source GNU Radio framework with both HDR and FDR using an NYUSIM [98]-based 77 GHz mmWave channel model and standard sub-6 GHz channel
- Our results demonstrate the significant gain of FDR over the traditional HDR and DT approaches in both Physical Layer Latency (PLL) and Packet Delivery Ratio (PDR).

4.2 Related Studies

This chapter relies on platooning as one of the most challenging applications in ITS. A considerable amount of research studies are focused on communication protocols for exchanging beacon messages within platoons. Most of these protocols do not operate on the PHY or MAC layer and are instead designed for higher layers.

Segata et al. [95] proposed an approach called *slotted beaconing* that uses a Time Division Multiple Access (TDMA) like approach to synchronize vehicles within the same platoon. The time slot to transmit a beacon is dependent on a vehicle's position in the platoon. The proposed protocol has been compared with generic approaches like Dynamic Beaconing (DynB), showing that it is highly beneficial when used in combination with Transmit Power Control (TPC).

Fernandes et al. [99] proposed different application layer-based strategies to address communication delays within a platoon. Based on the number of vehicles in a platoon, the channel is divided into different time slots according to the position of

the vehicle in the platoon. This TDMA like approach has been considered by Campolo et al. [16] to analyze the protocol while using FD communication. Simulations show that the delay is almost halved, allowing high-density platoon scenarios and higher update rates of the platoon controller.

Platooning vehicles use controllers to compute their accelerations based on the information of other platoon members. The dynamic, unreliable nature of vehicular communication poses a significant challenge to such a distributed controller [95]. Several proposals have been published to deal with these dynamics, e.g., controllers making use of shared consensus on the available information [100]. Also, different message dissemination strategies have been envisioned to provide frequent and recent updates to the vehicles of a platoon without overloading the channel. Some studies explore the use of Long Term Evolution (LTE) Device to Device (D2D) communications, enabling spatial reuse of the communication channel [101]. Other researches have focused on data exchange using Dedicated Short Range Communication (DSRC), e.g., by using multi-channel FD communication among vehicles [102]. Still, the latency is a major factor in the performance of the platooning system, in particular in sub-6 GHz frequencies due to the limited available bandwidth.

The concept of RADCOM, which combines sensing and communication, has been investigated only recently. For example, Dwivedi et al. [103] demonstrate such a system, which is capable of joint sensing and communication in the vehicular 77 GHz mmWave band. Other approaches aim to use Orthogonal Frequency Division Multiplexing (OFDM), which necessitates finding waveforms that are suitable to both sensing, and communication, in the frequency selective automotive radar band [104]. Nevertheless, the direct dissemination of messages from the leading vehicle to all the preceding vehicles in mmWaves is even worse because of high propagation losses, and thus, more power-hungry.

As an alternative to direct transmission of messages from the lead car to all platoon members, relaying the packets along within the platoon can be used to allow for better spectral efficiency (spatial reuse). However, even though infrastructure relays have been a key research domain for a couple of decades now, the literature on Full-Duplex Relaying (FDR) in both sub-6 GHz and mmWaves is still mostly based on analytical findings. For example, Lee et al. [105] experimentally demonstrated that the analog cancellation is not sufficient to suppress the reflected Self-Interference (SI) in mmWave and suggest an opportunistic full-duplex scheme to combat the impact of SI channel. Jiao et al. [75] are building an analytical model of LSI to analyze the effect of an Amplify and Forward (AF) relaying system in terms of spectral efficiency. Likewise, an analytical model based on Markov chains is proposed in [76], which analyzes the outage probability in FD multi-relay channels. López-Valcarce et al. [106] proposed a beamformer design for AF-based FDR in mmWave and analytically investigated the achievable upper bounds of spectral efficiency. Ma et al.

[107] considered FDR in D2D communications for mmWave-based 5G networks and proposed an algorithm that reduces the required transmit power levels and improves throughput results.

Bharadia et al. [83] presented the first complete FDR design, implementation, and experimental evaluation. They introduced the AF scheme based *construct and forward relaying*, which, unlike typical AF relays, avoid noise amplification by efficiently choosing the amplification factor. More recently, we studied Decode and Forward (DF)-based FDR by comparing it with HDR and presented FDR performance results in terms of PDR and throughput [88], [108]. In [32], we experimentally demonstrated the potential gains of FDR in terms of packet reception ratio, spectral efficiency, and end-to-end delay, measured at the physical layer. Simulative evaluation is also performed with GNU Radio-based implementation for both the AF and DF relaying strategies.

The aforementioned studies illustrate that the Full-Duplex Relaying (FDR) is a hot topic in research currently. Yet, while FD communication has gained significant attention with a substantial volume of literature available, covering both theoretical and experimental works, FDR is still an unexplored topic, with most of the existing studies commonly based on analytical models without considering real application scenarios. Especially the consideration of cooperative and mobile networks is completely out of scope right now. In this thesis, we take a first step towards closing this gap by providing a GNU Radio based simulation of an FDR system considering platooning as an example application with low latency requirements for both sub-6 GHz and mmWaves channels.

4.3 Communications in Vehicular Platoons

In platooning, timely and reliable communication is critical to transport the information for CACC controllers. Typically, every platoon member's controller requires information from both the platoon's leader and the immediately preceding vehicle (the *front vehicle*). The front vehicle's beacon messages can leverage TPC and a strong Modulation and Coding Scheme (MCS) due to the short distance, which greatly reduces the interference for uninvolved vehicles [95]. However, this is typically not the case for the leading vehicle, as illustrated in Figure 4.1.

The beacon messages from the platoon's leader are required to be received by all the following vehicles. In existing approaches, this is usually achieved via Direct Transmission (DT). When doing so, a relatively strong transmit power and a weak MCS has to be utilized for two reasons: Firstly, transmitted beacons are not repeated to maintain tight timing constraints and low jitter. Accordingly, conservative assumptions are made to ensure their delivery. Secondly, all vehicles within the

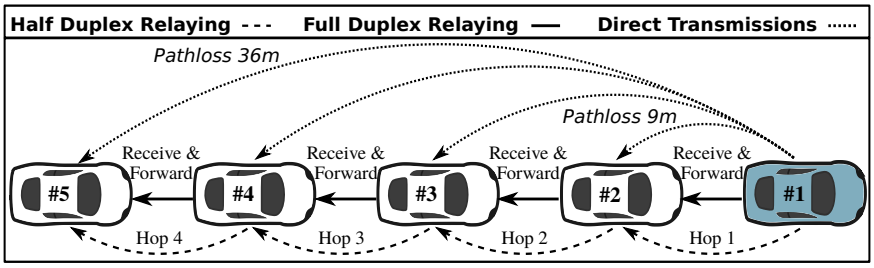

FIGURE 4.1 – Overview of our five-vehicle platoon model. The figure illustrates the three considered communication scenarios of Half-Duplex Relaying (HDR), Full-Duplex Relaying (FDR), and Direct Transmission (DT), for beaconing in platooning, © 2019 IEEE [33].

platoon have to be reached. In particular, the last vehicle is the furthest away and the most affected by pathloss (illustrated in Figure 4.1), as well as shadowing introduced by the other platoon members. Consequently, the interference domain of the transmissions due to strong transmit power is large. This can be problematic in high vehicle densities as many vehicles are influenced by the transmission.

4.3.1 Half-Duplex Relaying in Platooning

The formation of a platoon involves a leading vehicle and the following platoon members (cf. Figure 4.2). The currently practiced direct transmission approach would be needing high power transmissions and/or a weak MCS [15] in order to reliably and timely communicate with vehicles on either end of a platoon. These strong transmissions will produce a large interference domain, which can especially be problematic in high vehicle density highways, where many vehicles are expected to be affected by these transmissions. By adopting an HDR approach, the leading vehicle now only needs to send the packet to the immediately following vehicle. This vehicle relays the packet to its preceding vehicle and in a successive manner, such that eventually, the entire platoon receives the message.

Specifically, in RADCOM-based HDR, the highly directional antennas qualify the leading vehicle to use even less transmit power along with a higher-order MCS for the transmission of packets. Consequently, less interference (confined within the platoon region due to directionality of the antenna) is observed at ambient vehicles. Nevertheless, such HDR introduces excessive delays as each vehicle receiving the packet has to wait before forwarding to avoid the looped back SI at the same vehicle. In the best case of receiving the packet in the first time slot and forwarding it in the following slot, linearly incremental delays (depending on the platoon size) are to be anticipated. Moreover, for the channel access schemes such as CSMA/CA, which are subjected to randomized behavior, it is impossible to fully predict the introduced

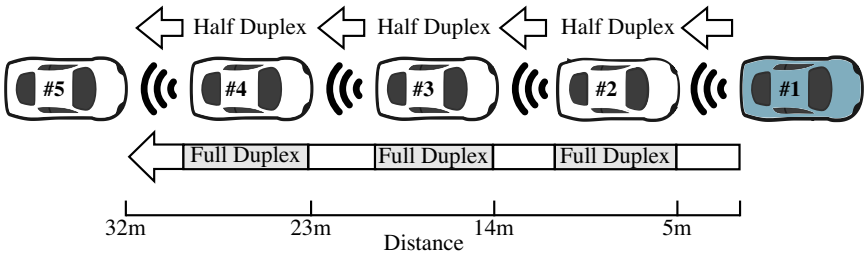

FIGURE 4.2 – The simulation scenario: A platoon of five vehicles, which uses either HDR or FDR. Arrows indicate transmissions. With HDR, four individual transmissions are needed, while FDR relaying only requires one. The bottom scale indicates vehicle distances from the leading vehicle, © 2020 IEEE [34].

transmission delays. Therefore, higher latency and more jitters are expected in this multi-hop HDR.

4.3.2 In-band Full-Duplex Relaying for Vehicular Platoon

Full-Duplex Relaying, on the other hand, has the ability to simultaneously receive and forward the packet (cf. Figure 4.2). This property makes FDR an attractive alternative to overcome the latency issues with the traditional HDR while maintaining its merits of low transmit power requirements along with a stronger MCS. Moreover, the simultaneous reception and forwarding allow the relaying vehicles to not wait for channel access while relaying. The only factor, however, that limits the performance of FDR is the Looped Self-Interference (LSI). For optimum performance, it is essential to reduce it to the receiver's noise floor.

The LSI illustrated in Figure 4.3 appears as a consequence of simultaneous reception and forwarding of the packet by the FDR vehicle at the same time and frequency. As a result, the packet forward by the leading vehicle experiences interference unless the LSI is suppressed to the receiver's noise floor. Recent advances in mitigating the LSI [7] have shown to suppress the interference caused by LSI substantially, such that only a small-to-negligible amount of residual LSI power is experienced. LSI suppression is typically realized in three stages: passive suppression, analog domain cancellation, and digital domain cancellation [7].

In the RADCOM case,the mmWave link already introduces high propagation losses. Moreover, the use of highly directional antennas, which are placed at the two ends of the vehicle for reception and forwarding, provides additional benefits in the case of RADCOM-based FDR. First, the interference domain is reduced as most of the power is confined within a platoon's communication region. Second, and most importantly, a huge passive suppression (antenna isolation) is introduced with no direct path for the Looped Self-Interference. As a result, the only possible source of

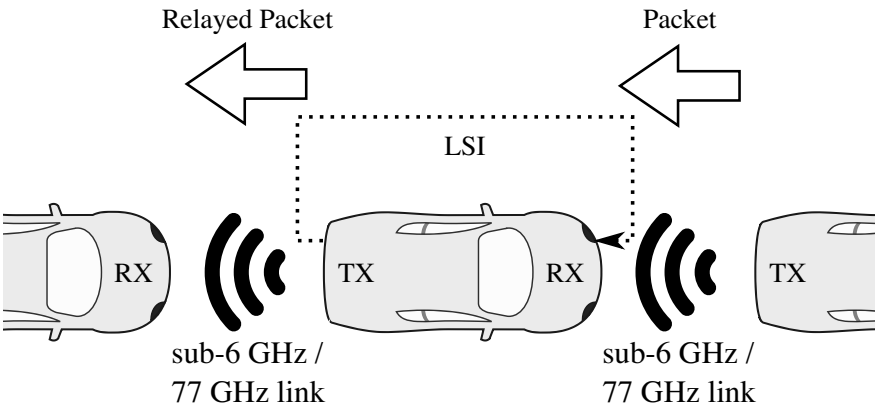

FIGURE 4.3 – FDR in a platoon: The first vehicle transmits a packet; the signal is received by the intermediate vehicle and forwarded to the preceding vehicle. However, because of simultaneous reception and forwarding, LSI is introduced, © 2020 IEEE [34].

LSI is through multi-path reflections, which in the case of RADCOM mmWave links, are even less because of high propagation losses. These LSI reflections can be easily suppressed in the digital domain using cancellation at the baseband level. Although the implementation of digital domain cancellation brings in more complexity at the relay node, there is no need for analog domain cancellation because of huge passive suppression.

In summary, we expect FDR to circumvents the channel access delays to timely deliver the packets to all platoon members while maintaining the high reliability of classic HDR. At the same time, the interference-domain for the neighboring vehicles is reduced.

4.4 LSI Modeling between Platooning Vehicles

With the antennas placed furthest apart, i.e., at the front and rear ends of the vehicle, maximal passive isolation of the looped back self-interference can be achieved. Also, as opposed to sub-6 GHz frequencies, the LSI typically observed in the case of RADCOM at the relaying vehicle is largely due to multi-path reflections and can be easily modeled in the baseband. Additionally, due to high propagation loss, no interference is assumed from the transmissions of the vehicle preceding the relaying vehicle. Consider the model shown in Figure 4.4 as an example, the transmissions from the *Leading Vehicle* are expected to not reach the *Following Vehicle X1* because of extreme propagation losses occurring as the result of the Nonline-of-Sight (NLoS) link between the two vehicles. The resultant multi-hop relay network can thus

operate in a non-cooperative manner, which eventually reduces the signal processing requirements at each relaying vehicle.

To model the LSI at each relaying vehicle in the platoon, consider the system model shown in Figure 4.4 where; the leading vehicle is forwarding the information to *Vehicle X*, operating in FD relaying mode. The *Vehicle X* receives the information, applies either AF or DF relaying scheme, and at the same time forwards it to the *Following Vehicle X1* over the sub-6 GHz or 77 GHz mmWave links. This simultaneous reception and forwarding; results in looped back self-interference at *Vehicle X*, as illustrated in the figure.

The baseband signal at the input of *Vehicle X* can be written as

$$y_{\mathrm{x}} = y_{\mathrm{lx}} + I_{\mathrm{X}} + n_{\mathrm{x}}, \tag{4.1}$$

where y_{x} is the combined received signal, y_{lx} is the signal from the leading vehicle, I_{X} is the LSI signal, and n_{x} is the receiver's noise.

The aim here is to model the LSI component (I_{X}) and eliminate it from the combined signal, which exists because of simultaneous reception and forwarding by the vehicle and can be obtained as

$$I_{\mathrm{X}} = s_{\mathrm{x}} * h_X. \tag{4.2}$$

Here h_X is the LSI channel between the relaying vehicle Tx and Rx ends, and s_{x} is the signal forwarded by the *Vehicle X*.

Since s_{x} is already available at the relaying vehicle, therefore, by acquiring an estimate of the LSI channel $\hat{h}_X$, an approximate looped SI signal ($\hat{I}_X$) can be

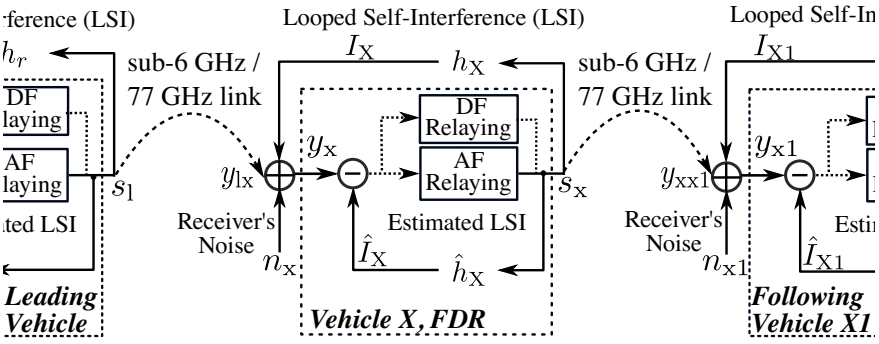

FIGURE 4.4 – Block diagram for modeling the LSI in vehicle platoons. The model here shows three vehicles, i.e., leading vehicle, vehicle X, and following vehicle X1, in a multi-hop FD relaying network. Each relaying vehicle is capable of performing both AF and DF relaying schemes, © 2020 IEEE [34].

reproduced as

$$\hat{I}_{\mathrm{X}} = s_{\mathrm{x}} * \hat{h}_{\mathrm{X}}. \tag{4.3}$$

This regenerated LSI $\bar{I}_{\mathrm{X}}$ can then be subtracted from Equation (4.1) to extract the desired signal y_{lx} from the *Leading Vehicle* as

$$y_{\mathrm{x}} - \hat{I}_{\mathrm{X}} = y_{\mathrm{lx}} + I_{\mathrm{X}} - \hat{I}_{\mathrm{X}} + n_{\mathrm{x}}. \tag{4.4}$$

Using (4.2) & (4.3) Equation (4.4) can be rewritten as,

$$y_{\mathrm{x}} - \hat{I}_{\mathrm{X}} = y_{\mathrm{lx}} + s_{\mathrm{x}} * (h_{\mathrm{X}} - \hat{h}_{\mathrm{X}}) + n_{\mathrm{x}}. \tag{4.5}$$

The residual useful signal in Equation (4.5), after the subtraction can be transformed in terms of error vector as

$$y_{\mathrm{x}} - \hat{I}_{\mathrm{X}} = y_{\mathrm{lx}} + s_{\mathrm{x}} * e_{\mathrm{X}} + n_{\mathrm{x}}. \tag{4.6}$$

In Equation (4.6), e_X represents the error between estimated and actual LSI channels. Note that if this error is close to negligible, i.e., $e_{\mathrm{X}} \approx 0$, then the residual LSI is maximally suppressed, and the expression is reduced to

$$y_{\mathrm{x}} - \hat{I}_{\mathrm{X}} = y_{\mathrm{lx}} + n_{\mathrm{x}}, \tag{4.7}$$

i.e., only the signal of interest, which is fed to the relaying scheme (AF or DF) module. Also, the right-hand side of (4.7) is the equivalent form of a typical HD receiver.

In practical full-duplex systems, e_X can be forced to a significantly small number, but it is never zero. This error magnitude certainly quantifies the performance of an FDR node, and for optimal performance, it is required to negligible. Nevertheless, because of the inaccuracies in LSI channel estimates, oscillator noise, and amplifier's non-linear behavior at the forwarding relaying vehicle, it is hard to force this error close to zero. This is the very reason why, at best, a full-duplex relay can achieve performance similar to a half-duplex relay, given that the error is close to negligible.

4.4.1 Looped Self-Interference Channel Estimation

To estimate the linear component of the LSI channel, we have considered the time-domain based least square estimation approach for error minimization. The least-square technique utilizes the Long Training Sequence (LTS) symbol attached in the IEEE 802.11p OFDM frame structure, shown in Figure 4.5, to acquires the Channel Impulse Response (CIR) estimate $\hat{h}_X$. For most accurate estimates, the LSI channel estimation is performed only during the training transmissions period, when leading

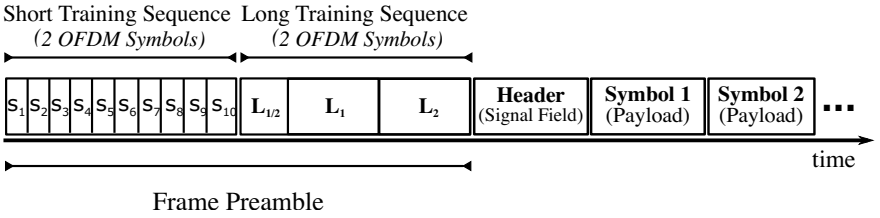

FIGURE 4.5 – The packet structure of the employed OFDM-based IEEE 802.11p compliant standard. Each packet starts with two short training sequence (STS) symbols and two long training sequence (LTS) symbols for coarse and fine synchronization of the incoming stream and; for channel estimation purposes. Followed by them is the packet header and then the actual payload symbols.

vehicle is in idle mode, i.e., $y_{\mathrm{lx}} = 0$. The received samples y_{x} under the stated condition can be obtained using Equations (4.1) and (4.2) as

$$y_{\mathrm{x}} = s_{\mathrm{x}} * h_X + n_{\mathrm{x}}, \tag{4.8}$$

i.e., only looped self-interference signal I_{X}. For a fixed and predefined LTS in s_{x}, the time-domain convolution in Equation (4.8) can be transformed into matrix multiplication as

$$y_{\mathrm{x}} = \mathbf{S}_{\mathrm{x}} \cdot h_X + n_{\mathrm{x}}, \tag{4.9}$$

which reduces the signal processing complexity of the estimation task. In (4.9), $\mathbf{S}_{\mathrm{x}}$ is the Toeplitz matrix, formed using the transmitted LTS symbol as detailed in [10]. Using Equation (4.9), the least-square based LSI channel estimate is obtained as

$$\hat{h}_X = \mathbf{S}_{\mathrm{x}}{}^{\dagger} \cdot y_{\mathrm{x}}, \tag{4.10}$$

where $\mathbf{S}_{\mathrm{x}}{}^{\dagger}$ is the Moore-Penrose (pseudo) inverse of $\mathbf{S}_{\mathrm{x}}$ and y_{x} is the received signal. Also, this inverse Toeplitz matrix $\mathbf{S}_{\mathrm{x}}{}^{\dagger}$ can be precomputed and stored prior to the beginning of training transmissions, which reduces the computational complexity of the overall estimation process. From Equations (4.9) and (4.10) mean square error can be calculated as

$$\|e_{\mathrm{X}}\|^2 = \|\hat{h}_{\mathrm{X}} - h_{\mathrm{X}}\|^2 = \sigma_x^2 \cdot \|\mathbf{S}_{\mathrm{x}}{}^{\dagger}\|^2. \tag{4.11}$$

By comparing (4.6) and (4.11), it can be concluded that the main source of residual LSI is the noise component σ_x^2 at the receiver. The lower this value is, the smaller error magnitude is there in the estimates, which reduces the LSI strength and improves the performance of the relaying vehicle.

4.4.2 Looped Self-Interference Regeneration

The regeneration process of the looped self-interference is equivalent to the equalization process. However, here, instead of equalizing the received signal y_{lx} at the relaying vehicle, the known forwarded signal s_{x} (as illustrated in Figure 4.4) is equalized with the estimated LSI channel $\hat{h}_{\text{X}}$. To force the channel impairment effects on the regenerated LSI signal I_{X}, the forwarded signal s_{x} is filtered with the estimated CIR, as expressed in (4.3). The regenerated looped self-interference signal $\hat{I}_{\text{X}}$, as a result, inherits the same channel characteristics as that contained by the received LSI signal I_{X}.

4.5 Performance in Sub-6 GHz Channel

To compare the performance of multi-hop Full-Duplex Relaying with the existing DT and possible TDD-based HDR for a vehicle platooning application, we conducted real-time simulation experiments in the GNU Radio framework. The framework is widely utilized because of its real-time signal processing and rapid prototyping capabilities, supporting not just simulation but real-world experiments via Software-Defined Radios (SDRs) as well. The simulation results shown here are built upon the implementation presented in the previous chapter, and since we have already seen a very degraded performance with AF-FDR in the sub-6 GHz channel because of noise amplification, therefore, here we only consider the DF scheme for the evaluation.

4.5.1 Simulation Setup

Figure 4.1 describes our simulation model with a five-vehicle platoon. Our simulative evaluation investigates the impact of key parameters, i.e., the residual LSI (in FDR) and the pathloss, on the PDR and PLL. For the channel modeling, we have implemented 4-taps frequency-selective Rayleigh fading channels for individual sub-paths between two vehicles within the platoon. Also, a linear 3-taps fading channel is implemented to model the LSI channel within a vehicle for the FDR case. It is worth pointing out here that the LSI channel resides within the same vehicle, i.e., both Tx and Rx are on the same vehicle. Therefore, it does not suffer from the Doppler shift, as the relative speed between Tx and Rx is zero. Hence, the basic least square estimation approach can be used for the LSI channel estimation. Additionally, to keep the LSI channel more realistic, among the three taps first one is kept strongest to maps the LSI through the direct path, and the remaining paths model the weak multi-path environment. In the scenario of Direct Transmission, the further pathloss impact due to the additional distance between the second and last vehicle is also included in the simulation setup.

For the baseband modulation/demodulation, we have used the GNU Radio-based Open Source stack for IEEE 802.11p standard for Wireless Access in Vehicular Environments (WAVE). The core of this framework is a modular and flexible OFDM transceiver implementation, which is fully compatible with commercial WiFi cards, and has been developed and comprehensively evaluated by Bloessl et al. in [90]. Additionally, the cancellation of LSI in the FDR case for simultaneous reception and forwarding is achieved via the implemented core module for LSI suppression. The details of the complete implementation can be studied further in [88].

In our simulation setup, we have transmitted 100 packets for each MCS defined in the IEEE 802.11p standard and measured the PDR based on the received Signal-to-Noise Ratio (SNR). Each packet comprises a 250 B payload, a 3 B header, and a 4 B CRC. Each run of packets is repeated 20 times to obtain a 95 % confidence interval, which for the sake of clarity, is not shown in the plots. Table 4.1 lists the key parameters of our simulation setup.

4.5.2 Evaluation Results

The following section presents and discusses the performance evaluation results of vehicular platooning for the sub-6 GHz channel.

4.5.2.1 Packet Delivery Ratio (PDR)

Figure 4.6 demonstrates the PDR performances at the last vehicle in the platoon for the HDR, FDR, and DT scenarios. For clarity reasons, the PDR for the intermediate MCS is not shown here; they also demonstrated similar performance behavior in the three considered scenarios. From the comparison of the HDR with the FDR approach, it can be seen that the PDR performance is roughly 1 dB worse with FDR for both

Table 4.1 – Key parameters of our simulation setup, © 2019 IEEE [33].

Modulations	BPSK, Q-PSK, 16-QAM & 64-QAM
Code Rates	1/2, 3/4, 2/3
Sampling Frequency [MHz]	10
Carrier Frequency [GHz]	5.9
Data Rates [Mbit/s]	3, 4.5, 6, 9, 12, 18, 24, 27
FFT/IFFT Size & Cyclic Prefix (CP) Length	64 & 16
PLCP (Preamble & Header)	(4 + 1) OFDM Symbols
Payload Size	250 B
Platoon Size	5 Vehicles
Inter-Vehicle Distance	5 m
Vehicle Length	4 m
Pathloss Second Vehicle (9 m)	67 dB
Pathloss Last Vehicle (36 m)	79 dB
Transmit Power	0 dBm

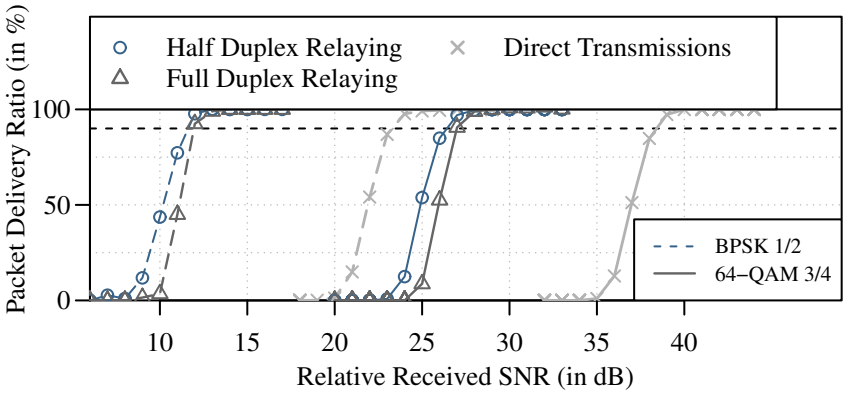

FIGURE 4.6 – Packet Delivery Ratio (PDR) performances (last vehicle) with the lowest (BPSK 1/2) and highest (64–QAM 3/4) Modulation and Coding Scheme (MCS) in the three considered scenarios, i.e., Half-Duplex Relaying (HDR), Full-Duplex Relaying (FDR), and Direct Transmission (DT), for vehicular platooning. The horizontal dashed line marks 90 % PDR, with 100 % indicating that all the packets have been correctly detected and decoded. For visual clarity, the plot is showing the data for the lowest and highest MCS.

BPSK 1/2 and 64-QAM 3/4 MCS. This 1 dB lower performance with FDR compared to HDR is because of the residual LSI, which basically raised the noise floor for the Signal-of-Interest (SoI) or leader beacons in this case, resulting in slightly reduced performance. It is worth mentioning here that for higher magnitudes of residual LSI, the performance with FDR could further worsen, as studied in [88]. Therefore, maximum suppression of LSI is a critical requirement for the optimal performance with FDR.

Similarly, the PDR performance with the DT scenario is roughly 11 dB poorer than FDR and over 12 dB worse as compared to HDR for both BPSK 1/2 and 64-QAM 3/4 MCS. This degraded performance with DT is intuitively due to the additional pathloss from the second to the last vehicle, which does not exist in HDR and FDR cases. Since the DF scheme regenerates noise-free packets at each intermediary vehicle, therefore, the relaying cases only suffer from the pathloss between two adjacent vehicles. Thus, the PDR performances with HDR and FDR (with sufficient LSI suppression) are anticipated to always outperform the DT case, especially for longer-size platoons.

4.5.2.2 Achievable Spectral Efficiency

Figure 4.7 demonstrates the achievable spectral efficiency for the last vehicle in the three considered scenarios. In a typical IEEE 802.11p standard, the maximum achievable spectral efficiency is 2.7 bps/Hz with a 27 Mbit/s link. The three considered scenarios are achieving this maximum possible spectral efficiency; however, the DT approach requires 11.5 dB more SNR as compared to FDR, and approx. 12.5 dB

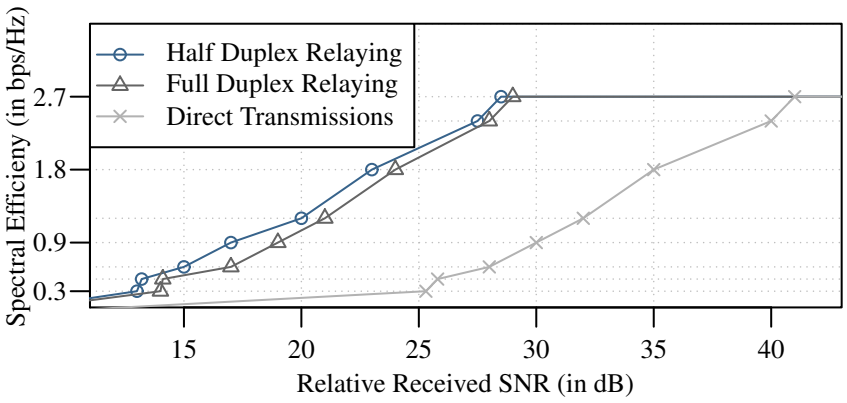

FIGURE 4.7 – Achievable spectral efficiency in the considered Half-Duplex Relaying (HDR), Full-Duplex Relaying (FDR), and Direct Transmission (DT) scenarios, © 2019 IEEE [33].

additional SNR in contrast to HDR. This is essentially due to the further pathloss between the second and last vehicle, thus demanding more relative SNR to obtain similar bps/Hz performance. Additionally, the bps/Hz performance with FDR is roughly 1 dB lower than HDR, intuitively because of the residual LSI, as already discussed in previous sections.

4.5.2.3 Physical Layer Latency (PLL)

Figure 4.8 shows the observed end-to-end delays at the last vehicle in each scenario. Here, PLL is the time interval a payload takes to traverse from source to destination, and it hugely varies with the considered MCS. The plot here is for a 250 B payload and indicates that the PLL introduced by HDR is the largest, even though it outperformed the other two in terms of PDR. This is because of the 4 hops involved with HDR in our simulation model (of a five-vehicle platoon), and in HDR, each vehicle has to wait for at least one-time slot (to avoid Looped Self-Interference) for reliable forwarding of the beacons.

Additionally, although there are no hops involved with DT still, the PLL experienced in this scenario is significantly larger compared to FDR. This is due to the inherent precondition of additional pathloss in DT and requires close to 12 dB more relative SNR; just to start receiving the packets with the lowest MCS, i.e., 3 Mbit/s, where (with the same SNR) FDR is already supporting an 18 Mbit/s link for communications. In essence, the ability of FDR to simultaneously receive and forward collectively transcends both the HDR and the DT approach, especially in terms of Physical Layer Latency (PLL), provided that the LSI is significantly suppressed.

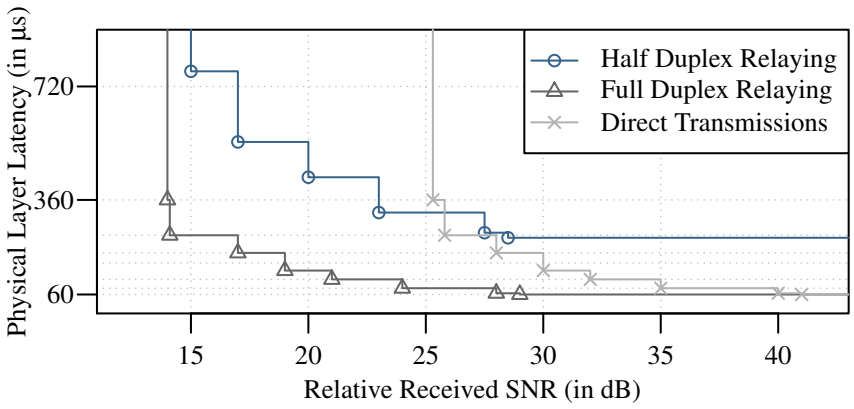

FIGURE 4.8 – Computed Physical Layer Latency (PLL) in the considered scenarios of Half-Duplex Relaying (HDR), Full-Duplex Relaying (FDR), and Direct Transmission (DT), © 2019 IEEE [33].

4.6 Performance in mmWave-77 GHz Channel

In this section, we evaluate the performance of RADCOM-based FDR platooning. We first discuss the emulated mmWave channel model and then present the simulation setup and performance results.

4.6.1 mmWave Channel Model

To model the 77 GHz mmWave channel, we have considered the NYUSIM [98], which is a MATLAB-based open-source mmWave channel simulator developed by the NYU WIRELESS. The simulator uses a statistical spatial channel model build upon measurements conducted at frequencies from 28 GHz – 140 GHz in various outdoor environments such as urban microcell (UMi), urban macrocell (UMa), and rural macrocell (RMa). It supports a wide range of center frequencies from 500 MHz to 100 GHz and RF bandwidth up to 800 MHz [109].

The 3D channel model generates omni-directional and directional CIRs and Power Delay Profile (PDP). The temporal and spatial statistics are divided by utilizing the time cluster spatial lobe (TCSL) approach. In NYUSIM, a time cluster is formed by a group of Multi Path Components (MPCs) arriving from different angles and traveling close in time. In contrast, a spatial lobe is composed of MPCs traveling in the same direction over a longer time period, which can reach up to several hundreds of nanoseconds. The aforementioned approach is driven by the measurements and gives a slightly different definition of the time cluster compared to the concept of the cluster in the other existing channel models such as WINNER and 3rd Generation Partnership Project (3GPP) models.

Furthermore, NYUSIM comprises two modes [109], the drop based mode and the spatial consistency mode. Under the drop based mode, subsequent simulation runs generate independent CIRs. However, in reality, a user moving in a local area or multiple users in the vicinity experience a similar scattering environment, which can not be captured by such a model. For this reason, recently, the simulator has been extended by the feature of the spatial consistency for generating correlated CIRs as the receiver moves in a local area. Spatial consistency and other components such as human blockage and outdoor-to-indoor penetration loss have been acknowledged in the 3GPP Release 14 and, therefore, are crucial for the mmWave communication systems.

For the evaluation of full-duplex relaying in RADCOM-based platooning, we have used this spatial consistency model in NYUSIM to obtain the CIRs and PDPs. The simulator is utilized to model the channel between every vehicle in the platoon for LoS scenario. Additionally, in the case FDR, it models the LSI channel between the transmitter and receiver of the same vehicle as well for NLoS case. The primary source of LSI in the mmWave-based platooning scenario are multi-path reflections, as there is a huge RF isolation of the direct component (leakage) between TX and RX front-ends because of antennas separation and their directionality. The channel coefficients between every vehicle and the LSI channel within a vehicle (shown in Figure 4.4) from the NYUSIM are imported into the GNU Radio framework, where the complete baseband system is implemented for real-time signal processing and evaluation.

4.6.2 Simulation Setup

For the performance evaluation of the traditional HDR and the novel FDR for the RADCOM communication link between vehicles in a platoon, we conducted a series of real-time simulations in the GNU Radio framework. GNU Radio is a widely utilized open-source platform that allows rapid prototyping and supports real-time signal processing – not just in simulations but also for real-world experiments using SDRs. At this point, it is worth mentioning that due to the poor performance of Direct Transmissions (DTs) even in the sub-6 GHz channel, we have not considered DT in RADCOM platooning, essentially because of very high propagation losses in the mmWaves.

Figure 4.2 shows our simulated scenario of a five-vehicle platoon. Our simulations investigate the impact of the 77 GHz mmWave channel and the residual looped-back SI in FDR on PDR, link capacity, and physical layer latency. The vehicles in the considered platooning scenario have a length of 4 m, and the inter-vehicle distance is 5 m. Each vehicle accommodates two highly directional antennas on the rear and front ends of the vehicle for transmission and reception, respectively. The Half Power

Beam-Width (HPBW) of each antenna is 10° with an antenna gain of 24.6 dBi. The communication channel bandwidth is 800 MHz in the 77 GHz band, which generates a noise floor of −73.9 dBm for RF front-ends with an expected noise figure of 11 dB.

To perform baseband modulation/demodulation in both HDR and FDR, we have built upon the GNU Radio-based open source stack for the IEEE 802.11p standard developed by Bloessl et al. [90]. The core of this framework is a modular and flexible OFDM transceiver implementation, which is fully compatible with commercial WiFi cards. We implemented both AF and DF relaying schemes for a comprehensive evaluation in the mmWaves channel (we have used this approach already for sub-6 GHz channels in the previous chapter). Additionally, in the FD relaying case, the LSI suppression is realized through an implemented core module for LSI cancellation. The LSI suppression module first estimates the LSI channel using the least square time-domain based estimation approach discussed in Section 4.4 and then uses the estimated channel coefficients to regenerate an approximate LSI signal at every vehicle; to mitigate the LSI.

In our simulation, we transmitted 100 packets through the 77 GHz channel and measured the PDR, link capacity, and physical layer latency at each of the following vehicles in the platoon. The packet structure includes training sequences, 3 B header, 250 B payload, and 4 B CRC. The transmissions were repeated 20 times for each MCS and transmit power to obtain a 95 % confidence interval. Table 4.2 lists the most important parameters of our simulation settings.

Table 4.2 – Key parameters of our simulation setup, © 2020 IEEE [34].

OFDM Tx / Rx Settings	
FFT Size	64 points
Data Carrier / Pilots / Nulls	48 / 4 / 12
Modulations	BPSK, Q-PSK, 16-QAM & 64-QAM
Code Rates	1/2, 3/4, 2/3
PLCP (Preamble & Header)	(4 & 1) OFDM Symbols
Carrier Frequency	77 GHz
Bandwidth	800 MHz
Achievable Link Rates	0.24 Gbit/s–2.16 Gbit/s
Antenna Gain (Tx & Rx)	24.6 dBi directional antennas
Antenna HPBW (Tx & Rx)	10° AZ, 10° EL
Receiver Noise Floor	−73.9 dBm
Residual Looped-SI	−72.7 dBm
Platoon Configuration	
Platoon Size	5 vehicles
Inter-Vehicle Distance	5 m
Vehicle Length	4 m

4.6.3 Evaluation Results

4.6.3.1 Packet Delivery Ratio (PDR)

Figure 4.9 shows the transmit power required by the leading vehicle to maintain a 100 % PDR at each preceding vehicle in the platoon, for both AF and DF relaying schemes in HD and FD modes. For visual clarity, the plot only shows the transmit power requirements with the lowest (BPSK 1/2) and highest order (64–QAM 3/4) MCS. It is worth mentioning here that the performance results with FDR are obtained with a non-negligible residual LSI of approx. 1.2 dB.

First, it can be seen in the plot that the 64–QAM 3/4 requires roughly 16 dB more transmit power as compared to BPSK 1/2 to achieve 100 % PDR at each vehicle. This would certainly increase the interference domain for the neighboring vehicles. Nevertheless, 64–QAM 3/4 carries 9 times more information than BPSK 1/2, which maps to a 9× reduction in physical layer latency because of the reduced packet size. Additionally, with highly directional antennas, this interference domain can be confined mostly within a platoon's communication region.

Secondly, with AF-HDR, the transmit power requirements increase from Vehicle-2 to Vehicle-5, whereas for DF-HDR, the power requirements remain almost the same regardless of the vehicle number. At the last vehicle in the considered scenario (Vehicle-5), AF-HDR requires roughly 5.5 dB more power to achieve similar performance. This degrading performance with AF-HDR is because of the simple forwarding of the received packet to the preceding vehicle, which gets further degraded (due to amplified noise) as it hops from vehicle to vehicle. On the other hand, the DF-HDR regenerates noise-free packets at every vehicle. Thus, there are

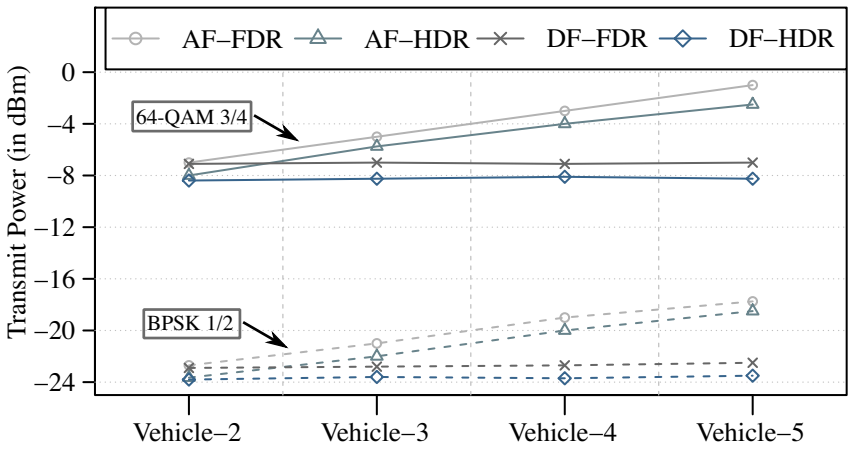

FIGURE 4.9 – Required transmit power from the leading vehicle for the considered AF and DF relaying schemes to maintain a 100 % PDR using a 77 GHz mmWave link, operating in both HD and FD mode. For visual clarity, the plot only shows the lowest and highest MCS results at each relaying vehicle.

no noticeable performance losses regardless of the vehicle number, but there is a cost of added-up decoding delays. Intuitively, the performance of AF relaying will get worse in platoons with more members.

Finally, the transmit power requirements with AF-FDR and DF-FDR are showing a similar behavior as we have seen in the case of HD relaying, i.e., DF is outperforming AF but at the cost of decoding delay. Also, from the performance comparison of FDR with HDR (regardless of the relaying scheme), it can be seen that there is a performance drop of roughly 1 dB at every relaying vehicle with FDR. This 1 dB reduced performance with FDR is due to the residual-LSI, which essentially increased the noise-floor for the packets arriving from the leading vehicle; and thus, more transmit power is required to achieve similar performance. Nevertheless, the benefit of simultaneous reception and forwarding of FDR, i.e., no waiting for channel access before forwarding, should not be overlooked here.

Intuitively, with higher residual LSI, the transmit power requirement with FDR will further increase, which could lead to bigger interference domains. Thus, for optimum performance with FDR, maximal mitigation of the LSI is a crucial requirement. By establishing this requirement, FDR potentially solves the existing issues of reliability and better coverage without causing additional channel access delays, not just in cooperative driving applications but for wireless communications in general.

4.6.3.2 Achievable Link Rates

Figure 4.10 shows the achievable link rate at the last vehicle in the considered platooning scenario. In our simulations, a maximum link rate of 2.16 Gbit/s is achieved with 64–QAM 3/4 for the 77 GHz mmWave channel of 800 MHz bandwidth.

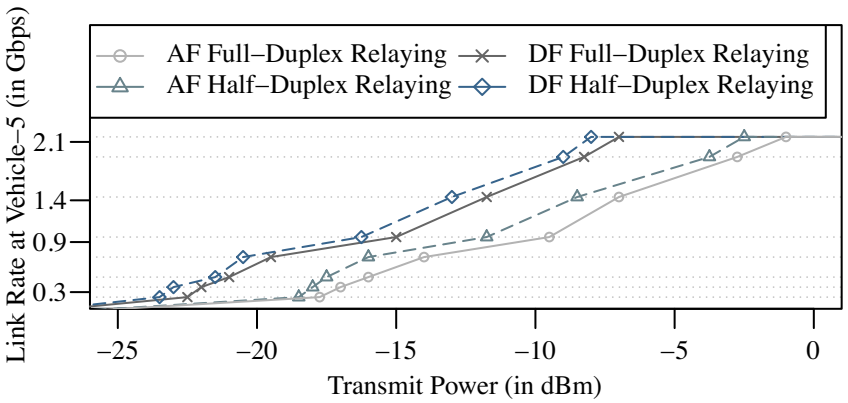

FIGURE 4.10 – Achievable bit rates at the last vehicle (Vehicle-5) for 77 GHz mmWave link with 800 MHz bandwidth, in the considered Half-Duplex Relaying (HDR) and Full-Duplex Relaying (FDR) approaches in the vehicular platoon.

The other link rates are listed in Table 3.1. Both AF and DF relaying schemes in HD and FD modes acquire this link rate; AF-FDR, however, is performing the worst and reaches 2.16 Gbit/s link rate at -1 dBm transmit power, whereas DF-FDR establishes a similar link rate with a transmission power of -7 dBm, i.e., a performance difference of 6 dB. This degraded performance with AF-FDR and AF-HDR is essentially because of the further channel distortion added while coursing through each relaying vehicle until the last vehicle (as AF relaying simply amplifies and forwards the received packet). Additionally, the link rate performance with DF-FDR is roughly 1 dB lower than DF-HDR, intuitively because of the residual LSI, as already discussed in the previous section.

4.6.3.3 Physical Layer Latency (PLL)

Physical layer latency is the time for which a packet engages the channel while traveling from the leading vehicle to Vehicle-5, and it varies based on the chosen MCS. The plot shown in Figure 4.11 indicates the reduction in packet size when a higher level modulation and coding scheme is employed. A higher-order MCS basically encodes more information per sample; as a result, less number of samples are required to send the same payload, and thus less occupancy of the actual physical channel duration while forwarding the packet. Nevertheless, to employ a higher-order MCS, higher received SNRs are required, and under similar receiver parameters, more transmit power is required to improve this received SNR. Therefore, the packet size is directly dependent on the transmit power levels.

Figure 4.12 presents the normalized physical layer latency estimated at the last vehicle with AF and DF relaying schemes in both FD and HD modes. The plot demonstrates that the physical layer latency introduced by HD relaying is the largest, even with the DF scheme, which outperformed all others in terms of PDR. This

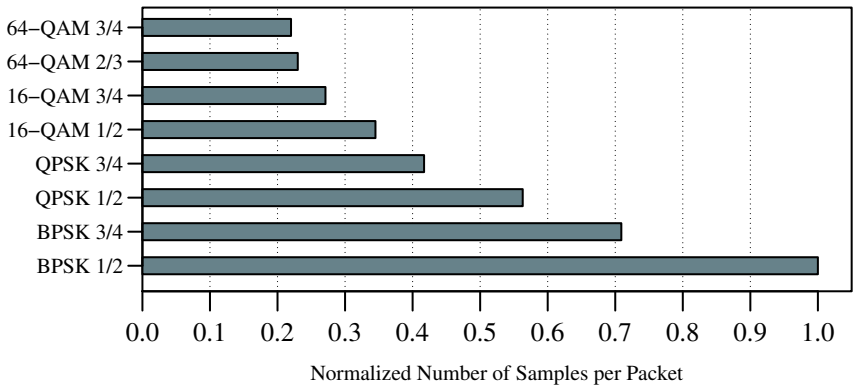

FIGURE 4.11 – Normalized packet length for sending the same payload with different modulation and coding schemes.

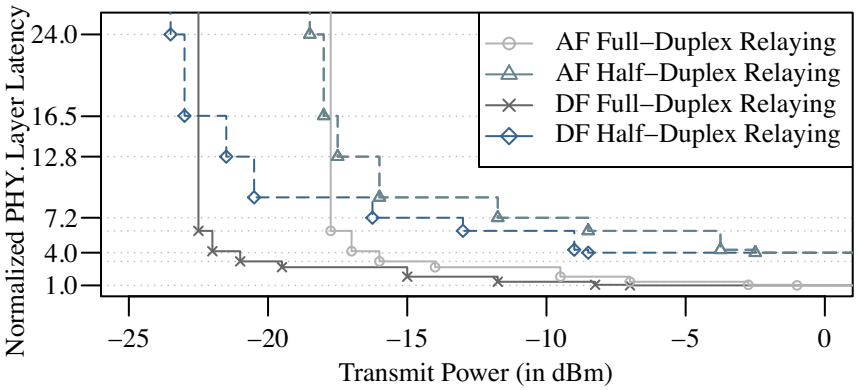

FIGURE 4.12 – Normalized physical layer latency at the last vehicle (Vehicle-5) for 77 GHz mmWave link with 800 MHz bandwidth in the considered platooning scenario.

is absolutely because of the waiting period involved in HDR for channel access to forward reliably. Also, these results are obtained for the most optimistic case of receiving and forwarding in the consecutive time slots; still, the latency with DF-HDR for similar transmit power levels can be approx. 4 times higher than DF-FDR.

Additionally, although in AF-FDR, there is no hops/waiting involved, still the physical layer latency experienced until −17.5 dBm transmit power level is more as compared to DF-HDR. This is due to the inherent precondition of accumulated channel distortion in AF relays imposed on the signal as it transverses through each relaying vehicle and requires roughly 8 dB more transmit power, just to start receiving the packets with the lowest MCS, i.e., BPSK 1/2. In essence, DF-FDR transcends all other relaying approaches in terms of physical layer latency. Even though there are decoding delays and complexity involved in DF-FDR, its better PDR performance at low transmit powers allows to support a higher-order MCS, reducing the packet size and, consequently, lowering the physical layer latency.

4.6.3.4 Energy and Channel Busy-Time Comparison

Figure 4.13 compares the energy requirements and the channel busy-time of each relaying scheme in both FD and HD relaying operation. We first analyze the energy requirements in each case for optimal performance, i.e., maintaining the maximum link rate (2.16 Gbit/s) with 64–QAM 3/4, between every vehicle until the very last vehicle (Vehicle-5). In the figure, it can be seen that the AF-FDR scheme requires the most energy for optimal communication performance until the last vehicle. This is due to both noise amplification and residual LSI in AF-FDR and can also be deduced from the previous results and discussions. The percentage energy reduction compared to this worst case, i.e., AF-FDR, is also shown in the plot, with DF-HDR demanding the least energy for optimal performance. The DF-FDR requires roughly

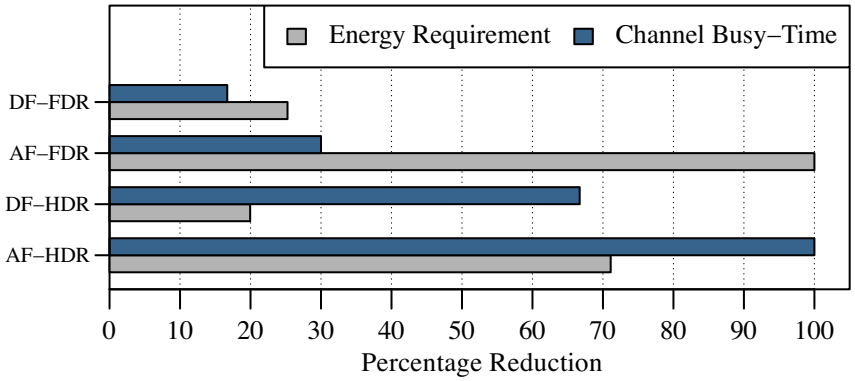

FIGURE 4.13 – Reduction in the energy requirements and the channel busy-time in each employed relaying scheme under both FDR and HDR modes.

5 % more energy as compared to DF-HDR, quite evidently to overcome the residual LSI that slightly increases the noise floor (by approx. 1.2 dB) for the incoming SoI. Additionally, since the AF-HDR does not have to deal with residual LSI; therefore, its energy requirement is lower (71 %) than AF-FDR. However, it is still higher than the DF schemes, intuitively because of the noise amplification factor introduced in each relay-hop until Vehicle-5 of the platoon.

In Figure 4.13, the percentage reduction in the channel busy-time of each case is obtained referencing the point when DF-FDR reaches its optimal performance, i.e., 2.16 Gbit/s with 64–QAM 3/4 MCS, until the last vehicle. The plot shows that with AF-FDR, the channel busy-time is 13 % more as compared to DF-FDR. This is due to the fact that when DF-FDR has adopted the highest MCS, the AF-FDR is still engaged with a relatively lower order MCS. Intuitively, AF-FDR, as a result, has a larger packet size to communicate, thus more channel busy-time. Likewise, the channel busy-time of DF-HDR and AF-HDR are far more, 51 % and 83 %, respectively. These large channel engaging durations are primarily because of the waiting period involved in HDR before forwarding the packet at every relaying vehicle in the platoon. From these percent reduction plots, DF-FDR is by far the superior choice in terms of both less energy requirement and reduced channel busy-time.

4.7 Concluding Remarks

Intelligent Transportation System (ITS) is an advance-application that aims to improve road traffic conditions. Inter Vehicular Communication (IVC) is among the primary component of ITS, which changes the way future cars will drive. Vehicular platooning is one of the ITS applications domain, in which groups of wirelessly connected vehicles are controlled automatically to follow each other at short inter-vehicle distances. The safe operation of a platoon relies on the frequent exchange

of information about kinematics of preceding vehicles, putting a high load on the communication network. The currently practiced approach of direct dissemination of messages from the leading vehicle to the last vehicle requires high power transmission for reliable delivery of messages. This, as a result, expands the interference domain with neighboring vehicles. Although the alternative approach of message relaying through intermediary vehicles compensates for this high power requirement, it increases the channel busy time and end-to-end delays in platoons.

In this chapter, we, for the first time, introduced Full-Duplex Relaying (FDR) in vehicular communications and showed its feasibility in platooning application. FDR has the advantage of significantly reducing the latency of communication while maintaining optimal data rates. For the first time, we compared the performance of the existing Direct Transmission (DT) approach and traditional Half-Duplex Relaying (HDR) with the proposed FDR approach for the sub-6 GHz WLAN technology stack (e.g., IEEE 802.11p), in particular for vehicle platoons. We further proposed acFDR use in RADar based COMmunication (RADCOM) systems operating in the 77 GHz mmWave band. The huge available bandwidths in the mmWaves support cooperative driving applications, such as sensor data transmissions with very low delays and high data rate 4k video streaming that would allow 'see-through' applications that ease the drivers' driving experience. Our results demonstrated significant performance gain with FDR over classical HDR in both sub-6 GHz and mmWave channels. Additionally, both types of channels exhibited similar (relative) performance, suggesting RADCOM FDR as a potential complementary technology to assist the existing sub-6 GHz system. Conclusively, the results presented here clearly indicated a substantial reduction in physical layer latency with FDR compared to traditional half-duplex relaying operation while maintaining optimal link capacity.

Part II: Visible Light Communication for Wireless Systems

Chapter 5

Vehicular-Visible Light Communication

IN Part I, our focus was Radio Frequency (RF)-based communication for bandwidth-efficient and low PHY-layer latency wireless communication. We specifically explored the idea of *in-band full-duplex relaying* and investigated the concept in both simulations and with Software-Defined Radio (SDR)-based real-world experiments. Later, we introduced the notion for Intelligent Transportation System (ITS) application, i.e., vehicular platooning, where the proposed approach demonstrated remarkable gains, especially in terms of lower end-to-end delays. Part II investigates Visible Light Communication (VLC) as a potential wireless technology to complement the RF for lower communication delays and bandwidth-efficient communications. The word "*complement*" here does not necessarily mean that VLC can completely replace the RF; it is rather used in the sense that VLC technology can support the RF communications, e.g., in the overly crowded sub-6 GHz spectrum, by distributing the communication channel's load.

As VLC utilizes the visible light portion of the electromagnetic spectrum, it differs significantly from RF-based communication technologies. For instance, the high directionality of light beams results in a small collision domain and allows high spatial reuse of the modulation bandwidth for devices in close proximity. Moreover, VLC requires a Line-of-Sight (LoS) link, hence improved security, as the interception of the relatively short LoS link by adversaries cannot go unnoticed. Such intrinsic characteristics of VLC make it a viable communication technology for different application scenarios, including Vehicular-VLC (V-VLC) [110]. Vehicular-VLC (V-VLC) has gained significant attention from both the research community and in the industry as a complementary technology to existing RF-based solutions such as Dedicated Short Range Communication (DSRC) and Cellular V2X (C-V2X). As opposed to very limited bandwidths such as 75 MHz bandwidth for DSRC (which is

now shared with WiFi), allocated for vehicular communications in the RF, visible light offers a huge free and unused spectrum for the communications.

This chapter investigates outdoor-VLC for vehicular applications and introduces an IEEE 802.11 compliant V-VLC system that is in line with the upcoming IEEE 802.11 LC standard as well. In this scope, earlier works helped in introducing new simulation models to explore V-VLC capabilities, technologies, and algorithms. Yet, experimental prototypes are still in an early phase. We aim to bridge this gap with our system, which integrates a custom made driver hardware, commercial vehicle light modules, receiver optics, Photo-Detector (PD), and an open-source signal processing implementation in GNU Radio that explicitly offers rapid prototyping. The proposed system is used to experimentally study the VLC performance in outdoor scenarios where – with simple optical modifications to reduce the ambient noise, long communication distances were achieved, even in broad daylight. In an extensive series of experiments, we assessed the communication performance by looking at realistic inter-vehicle distances. Our results demonstrated high communication reliability for distances up to 75 m with the introduced system, regardless of the time of the day.

The rest of the chapter is based on the following peer-reviewed publications:

- **M. S. Amjad, C. Tebruegge, A. Memedi, S. Kruse, C. Kress, C. Scheytt, and F. Dressler, "An IEEE 802.11 Compliant SDR-based System for Vehicular Visible Light Communications," in *IEEE International Conference on Communications (ICC 2019)*, Shanghai, China: IEEE, May 2019.**

  In this conference paper, my contributions were: the Tx/Rx baseband signal processing implementation in GNU Radio framework and its integration with Commercial Off-The-Shelf (COTS) hardware; real-time physical layer performance evaluation of the presented IEEE 802.11 compliant Vehicular-VLC prototype, and the analysis of clocking offsets between transmitter and receiver.

- **M. S. Amjad, C. Tebruegge, A. Memedi, S. Kruse, C. Kress, C. Scheytt, and F. Dressler, "Towards an IEEE 802.11 Compliant System for Outdoor Vehicular Visible Light Communications," *IEEE Transactions on Vehicular Technology (TVT)*, 2021, to appear.** DOI: **10.1109/TVT.2021.3075301.**

  This Journal article is the extension of my previous paper, additionally focused on: GNU Radio-based implementation for outdoor V-VLC, which utilizes a high-power LED headlight to supports communication even in broad daylight; the investigation on limited communication bandwidth due to the low pass behavior of COTS devices, driving the performance bottlenecks in V-VLC system; the impact of optics alignment on the receiver's performance and using an external clock to remove the clocking offsets.

5.1 Motivation

The surge of white Light Emitting Diodes (LEDs) as the primary source of illumination for different setups has paved the way for a range of new applications. Technological advances in solid-state lighting designs have resulted in the production of highly efficient and robust LEDs. The superior lighting and environmental properties of the LEDs compared to traditional lighting sources, such as incandescent and fluorescent bulbs, has resulted in a wide adaptation of LED-based luminaires for indoor and outdoor illumination [111]. Besides their increasing popularity for lighting applications, LEDs are being considered for a new type of application, namely VLC [17], [26], [112]. VLC is enabled by the fast switching capability of LEDs, which allows the modulation of digital information onto the intensity of the emitted light.

Nowadays, LED-based exterior lighting modules are proliferating in the automotive industry. The energy efficiency of the LEDs has primarily gained more significance due to the increased electrification in vehicles; the robustness against vibrations that yields longer service time; and the small form factor, which allows more versatile design; are some of the benefits that have motivated this rapid adaptation of LEDs in the automotive industry. This in turn has opened a new application domain, i.e., V-VLC [64], [110], [113]–[116].

V-VLC can be considered as an economical access technology, since the potential VLC transmitter,i.e., LED-based headlight and taillight, is readily available, whereas; a receiver might already be present, i.e., the rear-view camera, or can be integrated at very low cost (e.g., photo-diode). Traditionally, vehicle headlights and taillights are designed to provide illumination and signaling for the drivers; to improve safety on roads. Additionally, with the added communication capability, the lighting modules can further facilitate Vehicle-to-Vehicle (V2V) applications, as long as the communication does not hinder the primary tasks of illumination and signaling.

There are several characteristics of VLC that can benefit vehicular networking applications [117], [118]. For example, the LoS property and directionality of visible light offer spatial reusability of the modulated-bandwidth with tractable collision-domain [119], as well as improved security because the physical blockage of the Line-of-Sight link is easy to notice and hard to carry out between driving vehicles [120]. Conversely, the mobility in vehicular traffic and the interference in the outdoor environments (e.g., strong sunlight, bad weather conditions, ambient light) impose challenges for communication [121].

A V-VLC system must provide reliable communication, regardless of the outdoor conditions. This is especially important for safety-critical applications, which usually have stringent reliability and latency requirements. For this reason, a V-VLC system must have a carefully designed physical layer, particularly concerning the choice of efficient and robust Modulation and Coding Scheme (MCS) [122], [123]. In

this regard, Orthogonal Frequency Division Multiplexing (OFDM) has emerged as a viable modulation technique, essentially because of its resilience towards narrowband noise, and it has been widely adopted by many standards, including IEEE 802.11. The different baseband modulation schemes such as BPSK, and higher-order QAM, together with OFDM, provide an efficient yet resilient physical layer implementation. Besides that, an appropriate lighting module (e.g., high beam or low beam) and a linear front-end design are also required [124] for communications.

This chapter presents a complete IEEE 802.11 compliant V-VLC transmitter-receiver system build upon COTS components and an SDR-based implementation using the GNU Radio framework[3] for baseband signal processing. By means of extensive outdoor measurements under different ambient light conditions, including strong sunlight, we are able to evaluate the real-time experimental performance of the introduced V-VLC system. Limited by the headlight's low pass behavior, for realistic scenarios, the introduced prototype currently achieves a data rate of 1.35 Mbit/s with 64—QAM 3/4 for distances up to 40 m even in bright sunlight. If we trade data rate for distance, our prototype can achieve ranges beyond 75 m with lower-order MCS. Additionally, by choosing higher sample rates, thus operating in the headlight's low-pass region, a maximum data rate of 8.8 Mbit/s is measured at a fixed smallest practically possible inter-vehicle distance of 5 m. The introduced prototype can be seen as a first step towards the design of more sophisticated hardware and physical layer solutions for outdoor-V-VLC.

The core contributions of this chapter can be summarized as follows:

- We present a flexible GNU Radio-based IEEE 802.11 compliant implementation for outdoor Vehicular-VLC, which utilizes a high-power LED headlight – driven by a highly linear driver circuit that couples it with the SDR, and supports communication distances beyond 75 m, even in broad daylight.

- We confirm that limited bandwidth due to the headlight's low-pass behavior is the main performance bottlenecks in the introduced systems; and highlights that minor system adjustments (i.e., introducing simple optics on the receiving side) can largely improve the system performance.

- We investigate the outdoor performance of our V-VLC system even in bright sunlight and show that the sunlight does have a strong impact on the PD noise floor, but it can be eliminated completely with minor modifications.

- We also investigate the impact of optics alignment on the receiver's performance and analyze the daylight's impact on the PD noise floor in both baseband and passband for different design settings.

[3] www.gnuradio.org

5.2 Related Studies

VLC has been investigated in substantial depth and even successfully applied for many indoor use cases [26]. There are, however, many open challenges for outdoor operations. We focus on Vehicular-VLC, for which research primarily focuses on physical layer aspects of this technology [113], [123], [125].

Depending on the receiver design, the literature on experimental V-VLC can be split into two categories,which can be a camera image sensor [115], [117] or PD based [114], [121], [123], [126], [127]. The two different realizations for V-VLC (and VLC, in general) have peculiar properties. However, we considered Photo-Detector (PD)-based receiver design, which is rather inexpensive, and captures higher switching frequencies, thus, higher bandwidth.

Some of the key challenges in V-VLC exist due to the hardware limitations (for example, the low pass behavior of high-power headlight's LEDs) and the challenging outdoor conditions (e.g., high mobility, background noise from sunlight, and other light sources). Many designs in the literature have addressed these PHY-layer challenges as follows.

Liu et al. [114] conducted a comprehensive V-VLC study, including empirical measurements, where they investigated the impact of daytime and nighttime noise sources (i.e., sunlight and artificial light sources) on the Packet Delivery Ratio (PDR). Their results demonstrated that when the sun is not in the transmitter's Field of View (FoV), a 100 % PDR can be achieved for up to 100 m distances. The use of an optical lens in the implementation helped in reducing the receiver's FoV, and In the absence of this lens, direct sunlight saturated the receiver resulting in the reduction of PDR to 0 %. Despite the broadness of this study, the authors did not consider an actual vehicle lighting module; instead, they utilized an LED matrix, which does not emulate the radiation characteristic of a real automotive lighting module, which makes a great difference, especially for the driver circuit design in V-VLC. Additionally, the presented system achieved a 100 kbit/s data rate using the basic On-Off Keying (OOK) scheme.

Gavrincea et al. [125] introduced an IEEE 802.15.7 standard [128]-based VLC prototype. Their setup relied on COTS devices and GNU Radio-based SDR implementations for signal processing. Although the IEEE 802.15.7 standard specifies three Physical Layers (PHYs) and modulation schemes, the presented prototype only implements PHY 1, which uses OOK and Variable Pulse Position Modulation (VPPM). Kumar et al. [129] presented an FPGA-based VLC prototype for infrastructure-to-vehicle communication. A VLC-capable LED array is retrofitted into a traffic light case. The system utilized Direct-Sequence Spread Spectrum (DSSS) to modulate the transmitted signal. Simulation results showed that DSSS has better error performance

than OOK and Pulse Position Modulation (PPM). Experiments also demonstrated that the system could perform reliably up to 40 m distance.

To further improve the spectral efficiency of V-VLC systems, multi-carrier modulation schemes, OFDM in particular, have also been considered. Shen et al. [126], for the first time, conducted V-VLC measurements in real-world driving scenarios. They use OFDM instead of OOK to improve the spectral efficiency in V-VLC. The authors limited the number of subcarriers to 16 to obtain a better Signal-to-Noise Ratio (SNR) for each subcarrier. The system achieved the targeted communication distance of 45 m with a 70 % symbol reception rate using taillight; the authors used an optical lens to improve the SNR.

Narmanlioglu et al. [123] used multiple OFDM modulated taillights for direct and multi-hop V-VLC. The signal transmission is performed via four different taillight combinations using Direct Current-Biased Optical OFDM (DCO-OFDM). In contrast, Repetition Coding (RC) and Spatial Multiplexing (SM) techniques are used to realize Multiple-Input Multiple-Output (MIMO). Bit Error Ratio (BER) evaluation revealed that SM MIMO should be chosen over RC because it has better spectral efficiency and achieves the same throughput with lower-order modulation. Best BER performance is achieved when only the taillights closest to the PD are used for transmission, and the third brake light (centrally high mounted light) is not used. The third light only consumed power and reduced transmission power on all transmitters without contributing towards the system's performance.

Turan et al. [121] do time and frequency domain characterization of the V-VLC channel, conducting experiments in a static outdoor scenario during different times of the day. In order to account for the effects of background lighting noise on the channel, they do not utilize an optical filter in their setup. In turn, this allows the saturation of the PD when exposed to direct sunlight. Their results show that the sunlight not only impacts the system's effective usable bandwidth but also reduces the channel gain, compared to sunset and nighttime measurements.

The prototype presented in this chapter includes a highly linear VLC driver circuit with a bandwidth of 20 MHz to realize DCO-OFDM [124]. Additionally, we introduced GNU Radio-based IEEE 802.11 compliant implementation to investigate in detail the performance of different OFDM MCS for V-VLC. The proposed prototype is fully capable of performing in the outdoors, even in broad daylight, and it is in line with the goals of the upcoming IEEE 802.11 Light Communication (LC) standard.

5.3 V-VLC System Design and Implementations

Our V-VLC prototype design for outdoor communications is depicted in Figure 5.1. The prototype design has two main parts: the digital signal processing part, which

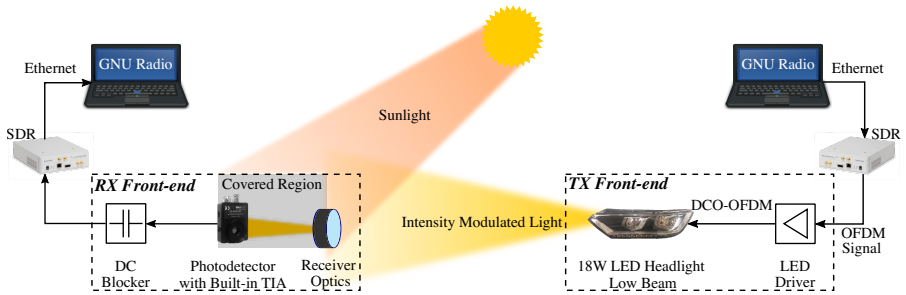

FIGURE 5.1 – A high-level description of our extended Vehicular-VLC transmitter-receiver system for outdoor measurements.

requires laptop PCs running GNU Radio, and SDRs (we use two N210 Universal Software Radio Peripheral (USRP) from Ettus Research), and the VLC enabling front-ends that includes a VLC driver circuit (which is available as open hardware[4]), a headlight, some receiver optics, and a photo-detector with DC blocker.

5.3.1 Baseband Signal Processing

In our V-VLC system, the baseband signal processing is performed in the GNU Radio framework. The related studies have also considered FPGA-based SDRs such as the WARP Mango board, which do offer deterministic timing, but they are rather inflexible, and it is often challenging to implement complex signal processing algorithms. In contrast, the GNU Radio framework is General Purpose Processor (GPP)-based, which allows signal processing using high-level programming languages C++ and Python, and it is easily accessible, thus, making it particularly easy to use, modify, and debug.

For the baseband transmitter/receiver implementation, we modified the GNU Radio-based Open Source stack for IEEE 802.11a/g/p developed by Bloessl et al. [89]. The core of this framework is a modular OFDM transceiver, which is fully interoperable with commercially available Vehicular Ad Hoc Networks (VANETs) prototypes and has been thoroughly evaluated in [90]. One of the key reasons for building upon this implementation is to later test and possibly evaluate the performance of our V-VLC system with commercial prototypes.

A detailed block diagram of the GNU Radio-based OFDM transmitter and receiver modules is illustrated in Figure 5.2. Compared to the receiver, the transmitter implementation is rather straightforward as the signal is fully specified in the IEEE 802.11 standard and has to be produced accordingly. Also, the transmitter side does not pose high computational demands, as the whole data frame can be precomputed before it is forwarded to the radio chain. Additionally, a 2x interpolation filter is employed on the raw OFDM samples to improve the spectral image and shape of

[4] https://www.hni.uni-paderborn.de/sct/projekte/vlc-projekt/

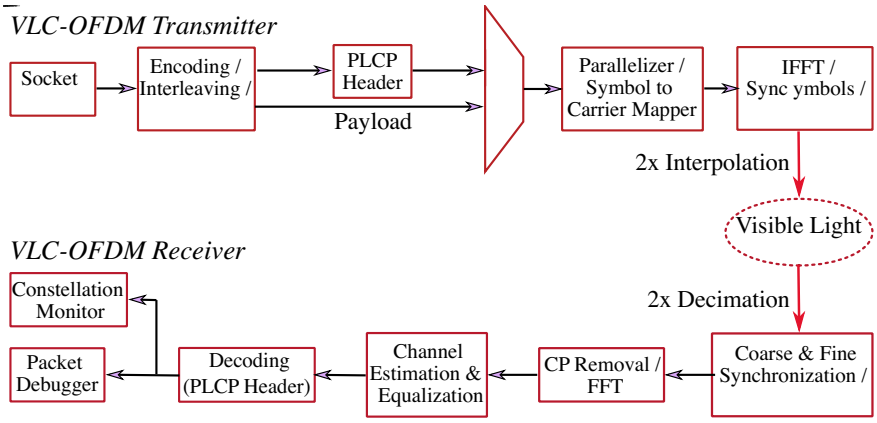

FIGURE 5.2 – Detailed baseband level block diagram of the OFDM implementation in GNU Radio.

the transmitted signal. The transmitter supports all packet sizes and IEEE 802.11 compliant MCS as listed in Table 3.1.

In contrast, the receiver implementation is a design decision, and it is generally a trade-off between complexity and performance. The most crucial stages in the receiver design include frame detection/synchronization and channel estimation/equalization. The receiver implementation of the presented V-VLC system supports four channel estimation techniques listed in Table 5.1. In an earlier work [122], we have already evaluated their performances and found LS to be the best estimator in terms of performance and complexity.

We used N210 USRP SDRs equipped with LFTX and LFRX daughterboards for the measurements. The operational-bandwidth of these daughterboards is in the range of 0 MHz to 30 MHz, which is well suited for VLC. The transmitting SDR is connected with a PC through an Ethernet port to communicate the OFDM samples from GNU Radio to the SDR. The SDR converts these samples into an analog signal and up-converts the resultant baseband signal to a carrier frequency of 2.3 MHz. The reason for this up-conversion is to avoid flickering and to prevent the interference from the ambient light sources that exist in the low frequencies and can then be easily removed at the receiver via a high-pass filter. Alternatively, more complex

Table 5.1 – Key physical layer parameters of the GNU Radio OFDM implementation, © 2019 IEEE [116].

Modulations	BPSK, QPSK, 16-QAM & 64-QAM
Code rates	1/2, 3/4, 2/3
Channel equalization	LS, LMS, STA, Linear Combiner
Interpolation factor	2x
FFT/IFFT size	64 points
PLCP (preamble + header)	(4 + 1) OFDM symbols

receiving optics could be used to suppress interference and thus provide a larger usable bandwidth [130]. It is worth mentioning here that the SDR's resultant output is a bipolar signal and preserves all the IEEE 802.11 adaptations.

5.3.2 VLC Front-Ends

As opposed to RF communications, where a modulated voltage signal is converted into electromagnetic radiation by an antenna; to realize data transmission, VLC uses Intensity Modulation (IM) to modulate a certain waveform onto the instantaneous optical power of the transmitting LED, and Direct Detection (DD) is used to recover the original signal on the receiving end, where photo-sensitive devices are used.

The current LED-based car headlights are designed to solely illuminate the streets. Since communication is not the intended goal, naturally, the LEDs' switching speed, which basically defines the bandwidth of a VLC system, has never been a major concern. As a result, the available headlights have low operational bandwidth. This bottleneck has been compensated to some extent through efficient spectral usage, i.e., improved bit/s/Hz, which our OFDM implementation inherently provides by supporting 8 different MCS based on the received SNR. Additionally, as a future direction, Adaptive Modulation and Coding (AMC) can be employed, such that each OFDM subcarrier can adopt an MCS dynamically based on its received SNR. With this, the optimal data rate per subcarrier may potentially be achieved, which can indeed lead to an overall improved link capacity.

5.3.2.1 Headlight Driver Circuit

Since the light intensity cannot be negative, the transmitted OFDM signal has to be non-negative unipolar with real values. The conversion of the bipolar signals from

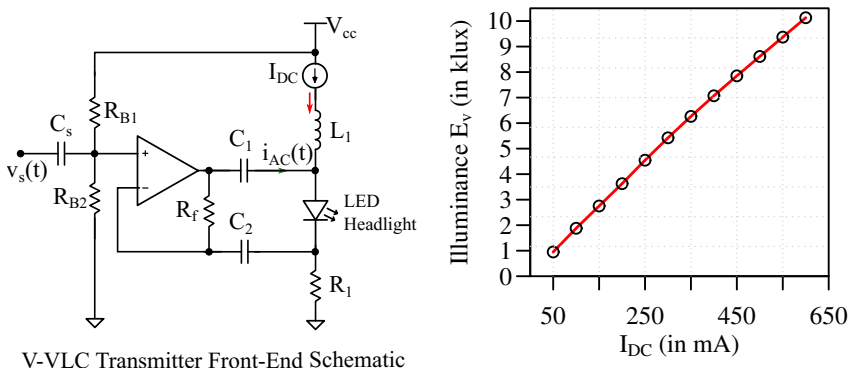

V-VLC Transmitter Front-End Schematic

(a) Headlight driver circuitry

(b) Illuminance vs. DC current

FIGURE 5.3 – Headlight driver circuitry and transmission chain linearity [124].

the SDR to a unipolar current signal, is done by the VLC driver circuit. This driver contains a bias tee, which creates an offset that shifts the signal into the positive range to achieve Direct Current-Biased Optical OFDM (DCO-OFDM). Due to the current biasing, the full span of the bipolar signal has to be mapped onto the positive range, which leads to a smaller amplitude and, therefore, makes DCO-OFDM less efficient in terms of average optical power.

The SDR generates a voltage signal for the payload to be sent. However, the luminous flux of the headlight is linear to the current only for a given range. Therefore, a linear Transconductance Amplifier (TCA) is required that translates the voltage signal into the current. Additionally, OFDM suffers from high Peak-to-Average Power Ratios (PAPRs), which only worsen with higher-order MCS. Thus, the headlight driving circuitry is designed to be linear for a wide range of input signal amplitude. Furthermore, an appropriate bias point is also critical for the optimal functionality of the front-end; otherwise, some parts of the input signal may experience clipping, which can cause distortions, and consequently, performance losses. Hence, a driving circuitry that efficiently combines an AC signal current-path with an adjustable DC current biasing is required. The driver circuit used in the prototype (shown in Figure 5.3a) is highly linear, with the capacity to effectively drive the COTS headlight. The circuit includes an internal bias tee, which provides a DC bias (I_{DC}) to the AC current signal ($i_{\mathrm{AC}}(t)$) within the linear region of the LEDs. The bias current and the amplitude is adjusted to operate in the largest possible linear range in [124], resulting in a Total Harmonic Distortion (THD) of less than 5%. As shown in Figure 5.3b, the current-to-illuminance ratio already provides a large linear range.

5.3.2.2 Photo-Detector

For the detection of an intensity-modulated light signal (through headlight), we used a Thorlabs photo-detector PDA100A-EC with a built-in variable gain amplifier; and connected it directly to the receiving SDR. The photo-diode inside PD translates the incident light to photo-current, which is then converted into a voltage signal by means of a built-in linear Transimpedance Amplifier (TIA). The resulting voltage signal is forwarded to SDR for baseband signal processing through GNU Radio in order to retrieve the transmitted payload.

5.3.2.3 Receiver Optics

The Photo-Detector used already has a large aperture area that offers high sensitivity. We have further utilized simple optics in our V-VLC prototype to converge the light intensity at the PD's aperture. As shown in Figure 5.4, the employed optic consists of two biconvex lenses with adjustable distance to fine-tune the focus. The optics are placed in front of the PD to focus the (gathered) incident light onto the PD's aperture.

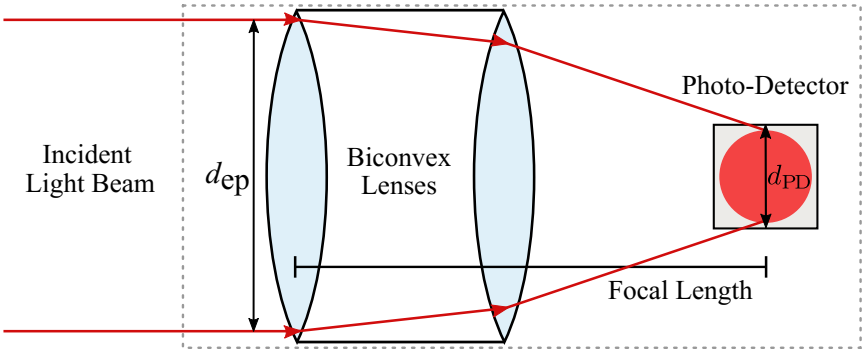

FIGURE 5.4 – Schematic explaining the receiver optics.

In this setup, the achievable gain through the optics G_{optic} can be calculated as

$$G_{optic} = \frac{\Phi_L}{\Phi_{PD}} = \frac{A_L}{A_{PD}} = \frac{\pi \frac{d_L^2}{4}}{d_{PD}^2}, \tag{5.1}$$

where Φ_L and Φ_{PD} are the radiant fluxes incident at the first lens and at the PD (without any optics), respectively, A_L and A_{PD} are the areas of the first lens and PD, and d_L and d_{PD} are the diameters of the lens and the PD, respectively. With 100 mm^2 area of our PD and 1452 mm^2 area of our first lens, the achieved optical gain is around 11.6 dB. It is important to mention here that the optic design placement in the V-VLC prototype is specific for this experiment scenario only. For on the road applications, the Field of View (FoV) may need to be changed by a factor of focal length.

5.3.3 V-VLC Operation in Bright Daylight

To enable VLC in outdoor environments, especially during the daytime with bright sunlight, additional design adjustments are required. On a clear day, the sunlight intensity is normally quite high and rather consistent compared to the intensity-modulated signal such that it can be filtered out through a high pass filter. However, from our experimental findings, the PD saturates when strong sunlight directly hits the PD. Figure 5.5 illustrates the behavior of PDA100A-EC PD for increasing levels of illuminance under different settings. The PD can only handle 24 klux, even in the simplest setting with no optics and TIA gain. The addition of optics further focuses the incident light on the PD aperture, which reduces the input illuminance capacity of the PD below 2 klux. This saturation of TIA, however, only happens when the light is directly incident on the PD aperture. In such situations, it is impossible to receive the optical signal from the headlight, and therefore, communication is not possible.

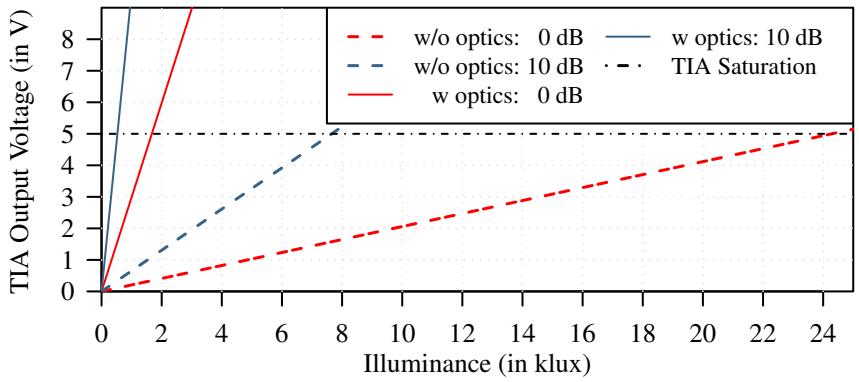

FIGURE 5.5 – Impact of incident light saturating the used PDA100A-EC Photo-Detector with and without the optics.

We solved this PD saturation problem in two steps: First, we optimized the FoV. It is worth mentioning here that the selection of FoV is usually a trade-off between the possible angle of reception and noise reduction. In addition to that, we covered the complete path, i.e., from the lens to the PD, in the optic design, to block the light from unwanted angles, as illustrated in Figure 5.1. Secondly, by using a DC blocker before the USRP, we filtered the strong DC-component at an earlier stage. During nighttime operations, these adjustments are not strictly required. Nevertheless, for a fair comparison, we used the same design settings throughout our measurement campaign.

5.3.3.1 Received Noise Behavior in Broad Daylight

To further analyze the impact of sunlight on the optical receiver's performance, we performed a series of noise measurements in broad daylight. We measured the noise values in both baseband and passband for three different design settings for a deeper understanding. Here, we only included the most relevant measurements in Figure 5.6.

First Setup:

The first noise measurement setting is the basic setup without the covered region and DC blocker. As expected, the strong daylight in this setup led to the total saturation of the PD and appeared to be useless for outdoor measurement during the day time.

Second Setup:

In the second measurement setting, to block the strong daylight, we covered the region from the lens to the PD (as illustrated in Figure 5.1) with a thick blanket.

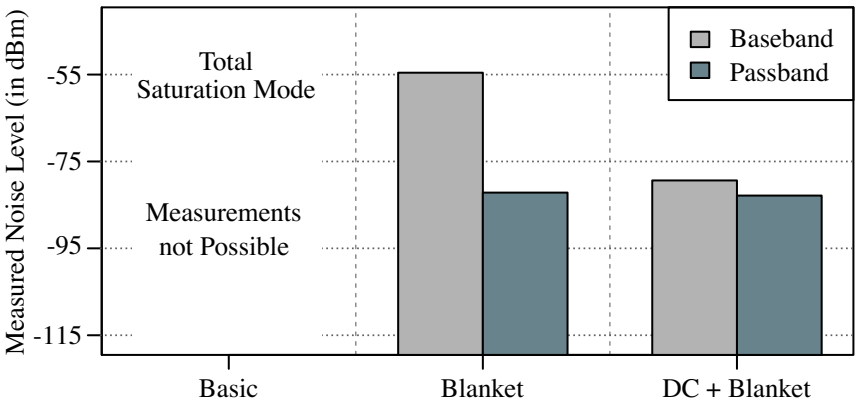

FIGURE 5.6 – Impact of our different design modifications on the receiver's noise levels in broad daylight.

As opposed to the basic setup (with total saturation), the USRP was able to record the actual noise samples this time. The averaged noise measured at both baseband and passband levels is illustrated in Figure 5.6, where the noise in the baseband around DC is approximately 30 dB higher than the passband. Additionally, the exact received noise samples in baseband and passband are shown in Figure 5.7a. The measured passband noise is merely the quantization noise due to the Analog-to-Digital Converter (ADC) in the received signal processing path, whereas the baseband noise (due to the daylight) is somewhat periodic and much stronger close to -55 dBm.

Third Setup:

The third measurement setup, which completes our proposed design (Figure 5.1), additionally includes a DC blocker between the PD and USRP. Figure 5.6 shows that the baseband noise is substantially reduced with the addition of a DC blocker in the receiving path. However, it is still approx. 5 dB higher than passband noise. Figure 5.7b presents the received noise samples in the third setting, where, due to the DC blocker, the baseband noise is now close to the quantization noise of the ADC.

These results basically characterized daylight's behavior close to DC that resides in the baseband and can be substantially reduced with a simple DC blocker. Moreover, the determined baseband noise behavior evidently supports the idea of up-conversion of the baseband signal before intensity modulation, as it essentially bypasses the interference from low-frequency ambient noise sources, which maintained a higher noise level in the baseband. To conclude, as significant it may sound at the first guess, the impact of daylight is not that extreme in reality and can be managed with rather simple design adjustments.

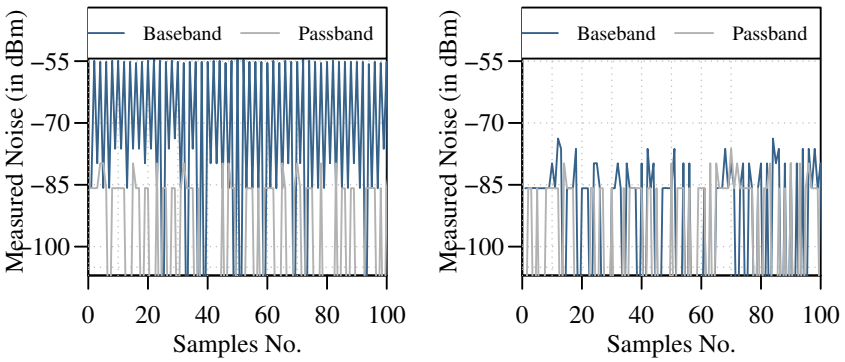

(a) With blanket only

(b) With blanket and DC blocker

FIGURE 5.7 – Received samples at baseband and passband levels in broad daylight.

5.4 Experimental Evaluation

This section presents selected results focusing on outdoor experiments from the measurement campaigns we conducted using our prototype.

5.4.1 Impact of Clock Offset

During the initial trial sessions of our measurement setup in a controlled lab environment, we observed a periodic distortive behavior in the received constellation. This behavior appeared to be more severe in higher-order MCS, where the Euclidean distance between constellation points is smaller, which makes symbol decoding decisions more error-prone. The reason for this periodic distortion is intuitive, and it typically exists due to the drift between transmitter and receiver SDRs' clocks, which causes a periodic sampling frequency offset. To further study the phenomenon, we computed the BER of our VLC system, first with the SDRs' internal clocks and then through a common external clock source. In both experiments, we placed the transmitter and receiver 2 m apart. For every MCS, we transmitted 20 000 packets, each containing 250 B payload, and computed the BER of each packet at the receiver.

Figure 5.8 shows the per-packet BER performance of 64-QAM in both experimental scenarios. For lower order MCS up-to 16—QAM, there were no bits in error at 2 m separation distance with both internal and external clocks. Therefore, the BER results for these MCS are not shown here. However, a per-packet BER of around 50 % was measured for 64—QAM over periodic intervals with unsynchronized internal clocks of the SDRs. The most interesting fact in Figure 5.8 is the repetitive burst error behavior with 64—QAM.

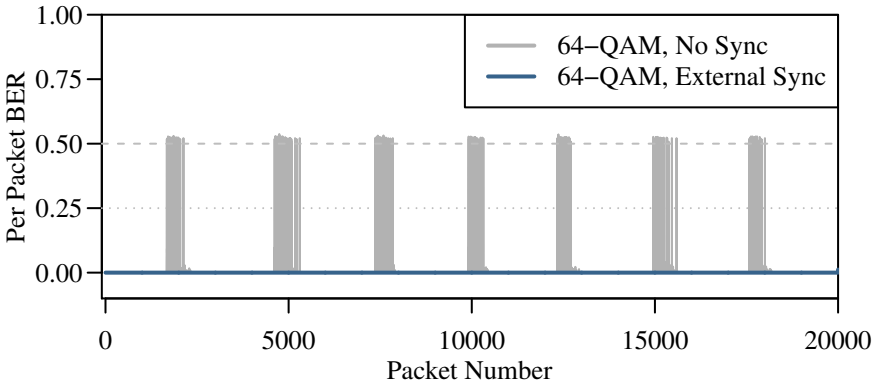

FIGURE 5.8 – Impact of unsynchronized and externally synchronized clocks of the used SDRs on the BER of VLC receiver in a controlled lab setup.

For such higher-order MCS, these experiments provided us some very useful insights. First of all, we observed that if the clocks of both transmitter and receiver SDRs are completely synchronized, these periodic error bursts can be eliminated completely. Secondly, the repetitive burst error behavior with internal clocks occurs approx. after every 2000 packets, specifically for 64–QAM.

5.4.1.1 PDR over Distance without External Sync

To evaluate the impact of clocking offset on our V-VLC prototype's performance, we conducted measurements in the basement of a parking lot [116]. Figure 5.9 shows the PDR plot for each MCS with increasing distance between the transmitter and receiver for an indoor setup without external clock sync. In the plot, a PDR of 100 % means that all packets have been correctly detected and decoded, and the horizontal

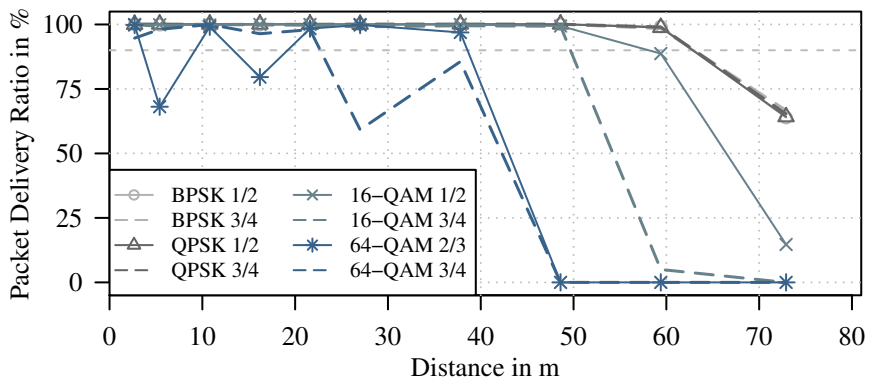

FIGURE 5.9 – Experimentally measured PDR performance for every MCS, with 1000 packets sent per transmission, © 2019 IEEE [116].

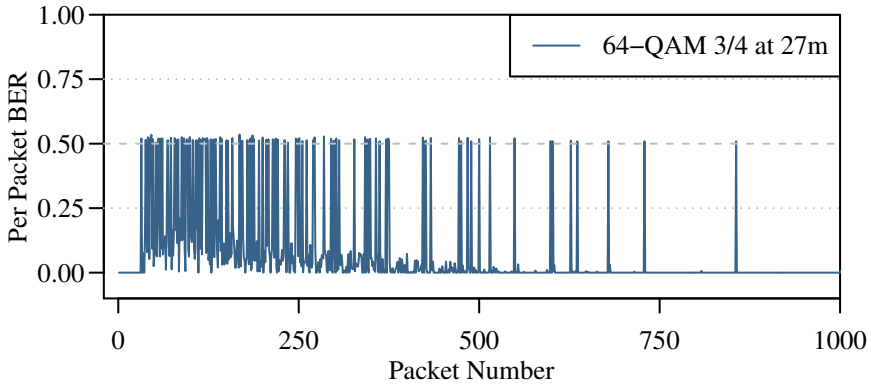

FIGURE 5.10 – Experimental per packet BER performance with 64—QAM 3/4 at a distance of 27 m, © 2019 IEEE [116].

dashed line marks 90 % PDR. As can be seen, we measured over 90 % PDR at a distance of 60 m with lower-order MCS (BPSK and QPSK). Even the 16—QAM 3/4 MCS offers a smooth – close to 90 % – PDR performance at a distance of approx. 50 m.

Nevertheless, with 64—QAM, we see some deep drops in PDR performance irrespective of the distance. This performance drop is due to the sampling frequency offset between transmitting and receiving SDRs, which we already discussed previously. The per-packet BER performance of 64—QAM 3/4 shown in Figure 5.10 further demonstrates the impact of clock drift. It can be seen that the granular burst error behavior, which starts appearing in the initial packets, gradually fades away in a similar manner as observed previously in the controlled lab measurements (Figure 5.8).

In order to evaluate the full capacity of our V-VLC prototype, we, therefore, decided to use an external clock synchronizer in the outdoor measurement campaign.

5.4.2 Outdoor Measurement Setup

To evaluate the performance of our V-VLC prototype, we conducted live-measurements in an open-air car parking facility. Our experimental setup is shown in Figure 5.11. Our location for the measurement campaign provided reasonable space for large transmitter-to-receiver separation distances without interruption. In the measurement campaign, we fixed the headlight – coupled with the driving circuitry; and other transmission chain hardware on one end of the parking facility. We placed the PD and corresponding devices in the reception chain on a mobile cart and incrementally increased the distance between transmitter and receiver in a straight line. The 2.5 m equidistant marks on the parking lot's ground assisted in the cart stationing at incremental distances.

FIGURE 5.11 – Measurement facility and the transmitter-receiver setup.

For every measurement point, we transmitted 1000 OFDM packets of size 250 B (2×10^6 bit per transmission) with each MCS listed in Table 3.1 and obtained the PDR and the Received Signal Strength (RSS) values at the receiver. The TIA gain (within the PD) is also varied from 0 dB to 70 dB during different measurement campaigns. Additionally, a receiver gain of roughly 11.6 dB is obtained exclusively through the optics. A maximum separation distance of 75 m between the transmitter and receiver is only possible due to the space constraints of the facility. Table 5.2 lists the most relevant parameters of our measurement setup.

5.4.2.1 Frequency Response and Achievable Data Rates

We have used a center frequency of 2.3 MHz for the up-conversion of our baseband signal. While the translation to center frequency attenuates our baseband signal by a reasonably small factor due to the LEDs' low pass behavior, this makes our system robust against ambient light interference. The low-pass behavior of the considered headlight is demonstrated in Figure 5.12a, where the signal power is reduced by 10 dB per 1 MHz on average. This behavior is consistent with the measurements of the high-power LEDs in [121]. For a 1 MHz sampling frequency and 2x interpolation rate, the resultant OFDM signal spectrum is shown in Figure 5.12b, where approx./ 5 dB power difference can be observed between the lowest and highest sub-carrier

Table 5.2 – Hardware specific parameters for the measurements.

Headlight	VW Passat 18 W LED-based low beam
Headlight's 3 dB bandwidth	1.3 MHz
PD	Thorlabs PDA100A
PD's 3 dB bandwidth	2.4 MHz
PD gain	0 dB–70 dB
Relative height RX/TX	63 cm
Distance between RX/TX	2.4 m–75 m
Optics gain (G_{optic})	11.6 dB
Center frequency	2.3 MHz
Sampling frequency	1 MHz
Data rates	0.15 Mbit/s–1.35 Mbit/s

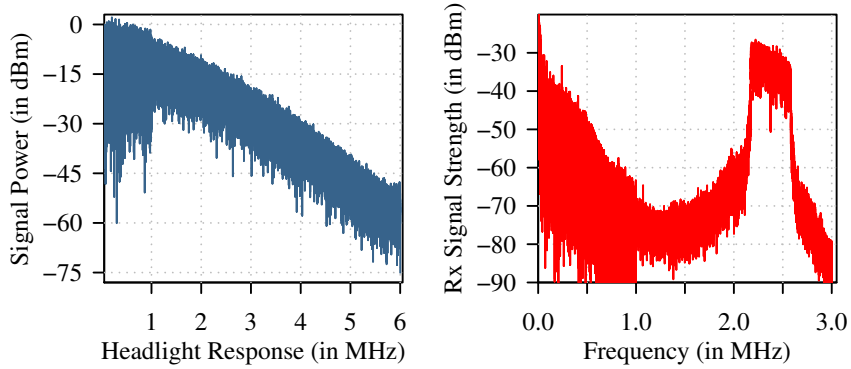

(a) Headlight frequency response **(b)** Detected OFDM signal

FIGURE 5.12 – Impact of low-pass behavior of the headlight on the transmitted OFDM signal.

frequency. For an effective bandwidth of 500 kHz, our prototype achieves a maximum data rate of 1.35 Mbit/s reliably for up to 40 m. Compared to the ones reported in the literature for typical indoor VLC [131], the achieved data rates can be considered relatively low. However, this is only due to the slow switching frequency of the high brightness LEDs used in an average design of automotive lighting modules, which limited us to use a lower sampling frequency, i.e., 1 MHz. Notice that higher sample rates can also be employed to obtain better data rates, at least for shorter distances, where the headlight's low-pass behavior can be compensated by high received SNR.

To further investigate this notion, we considered the shortest practically possible inter-vehicle distance of 5 m between Tx (headlight) – Rx (PD) and increased the sample rates from 1 Msps to 10 Msps; providing an effective bandwidth of 0.5 MHz–

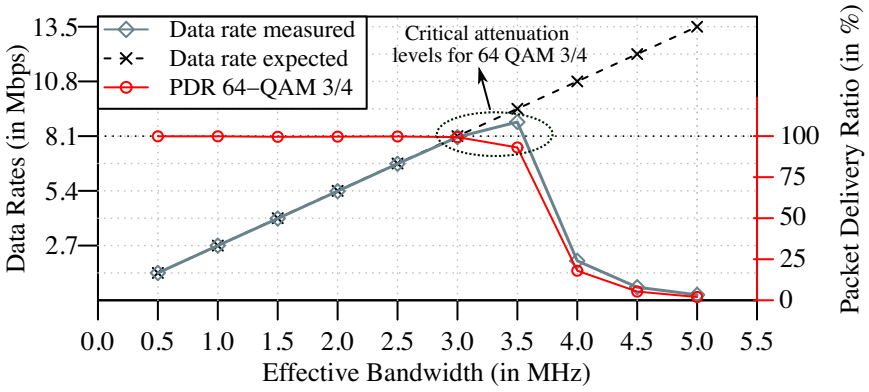

FIGURE 5.13 – Measured data rates together with the PDR at the smallest practically possible distance of 5 m with increasing sample rates.

5 MHz. The resulting data rates are shown in Figure 5.13. The plot shows that for bandwidths higher than 3 MHz, the PDR starts to drop rapidly, and so does the data rate. The curve starts to deviate from the expected maximum data rate and drops sharply after 3.5 MHz bandwidth. Although the data rate increases from 8.1 Mbit/s–8.8 Mbit/s in the range between 3 MHz–3.5 MHz bandwidth, it is still lower than the expected 9.45 Mbit/s data rate. For the bandwidths over 3 MHz–3.5 MHz, the received SNR reaches critical levels due to the headlight low-pass behavior, particularly affecting the higher OFDM carriers. At this point, the system needs to opt for lower-order MCS, i.e., QPSK and BPSK, in order to maintain 100 % PDR for higher bandwidths. However, none of these modulation schemes could beat the maximum achieved 8.8 Mbit/s data rate, even for bandwidths as high as 5 MHz. The measured data rates and PDR results in Figure 5.13 are in line with the headlight frequency response presented in Figure 5.12, with RSS dropping 10 dB per 1 MHz, and suggest the maximum usable bandwidth of 3 MHz–3.5 MHz at the smallest practically possible inter-vehicle distance of 5 m.

5.4.2.2 Illuminance Levels

To analyze the behavior of ambient light and to study its impact on the system's performance, we also recorded the illuminance levels throughout the measurement campaign. The measured illuminance values and the corresponding noise strength at different times of the day are illustrated in Figure 5.14. The measurements have been conducted on a summer day, with back-and-forth changes in the sky conditions, i.e., from bright sunny to partly cloudy and vice versa. In the case of strong and direct sunlight hitting the lux meter, the highest luminance recorded was around 100 klux, whereas during the deepest night hours, the luminance value dropped down to 10 lux. For accurate illuminance measurement, the lux meter was always placed

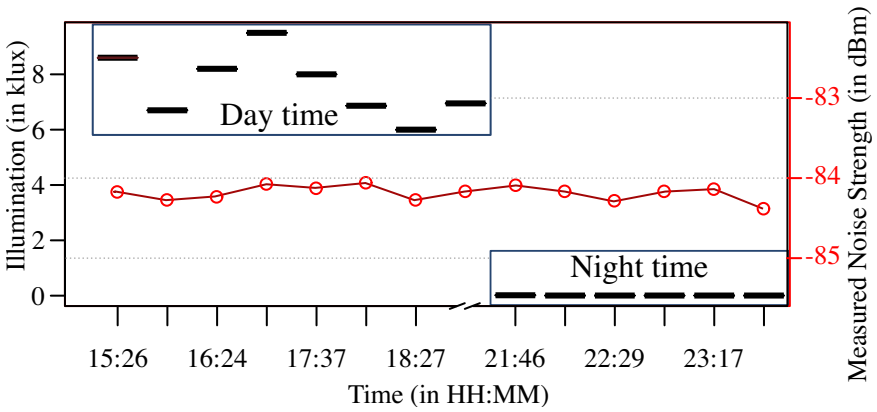

FIGURE 5.14 – Illuminance levels recorded during different times of the measurement campaign in our outdoor setup.

in parallel to the photo-detector, such that the incident light is the same on both. The day time measurements were conducted in the afternoon; from 15:30 to 16:30, with ambient illuminance fluctuating between 6 klux to 10 klux (cf. Figure 5.14). The night time measurements have been performed after 21:00 in the presence of only dim streetlights with illuminance values below 15 lux, which is roughly one-thousandth of the illuminance during day time. The most stimulating finding in the plot is that the noise measured against each luminance level is roughly similar (below −84 dBm) regardless of the time of the day, which particularly indicates our prototype's robustness towards ambient light.

5.4.3 Received Signal Strength (RSS) over Distance

Figure 5.15 presents the obtained signal and noise strengths at the receiver for increasing distance in the outdoor experiments. For these measurements, we fixed the internal gain of 10 dB for the PD. It is important to mention here that without the design adjustments proposed for the outdoors, the receiving PD remains in total saturation mode and detects nothing, as discussed in 5.3.3. The major sources of noise in VLC systems are; interference noise by ambient light, shot noise introduced by the PN-junctions of diodes, thermal noise produced by electrical components, and the quantization noise due to ADCs. As shown in Figure 5.15, the measured noise power in our experimental scenario stays almost constant at around −85 dBm, regardless of the distance and time of the day. The similar noise behavior in both daytime and nighttime clearly demonstrates the close to the negligible impact of the sun on noise levels. The measured noise strength is also in-line with our initial noise measurement (Section 5.3.3) in broad daylight.

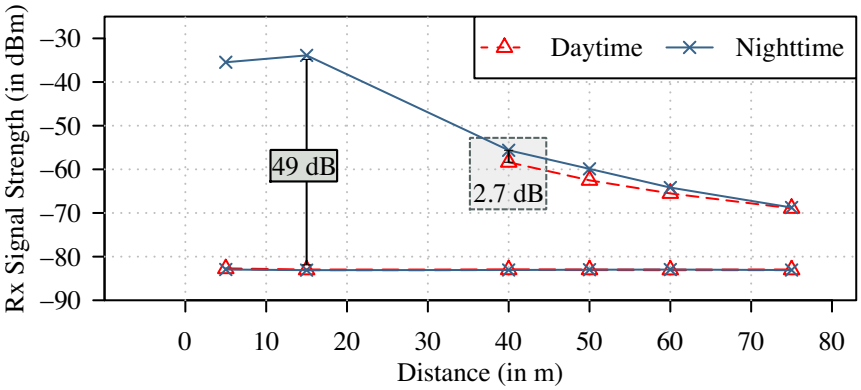

FIGURE 5.15 – Experimentally measured and analytically calculated RSS and noise levels at both day and night times in our outdoor setup.

On the other hand, the received signal strength first improves with increasing distance (i.e., up to 15 m) and then decreases rapidly with further increasing distances. The initial improvement in the RSS is because of the optimal FoV of the PD around 15 m. This optimal FoV point mainly depends on the relative height between headlight and PD. The signal degradation in VLC is essentially due to inverse square law, heterogeneous distribution of light, which results in strong spatial dependency [110], and the propagation medium, e.g., particles in the air.

In Figure 5.15, it is worth noticing that the RSS during daytime is 2.7 dB lower than at nighttime (at 40 m), and this RSS difference reduces with distance. This deviation in RSS can possibly be due to the measurement errors; such as: (i) misalignment in the optics design, (ii) misalignment of the cart carrying the receiver setup, and (iii) headlight displacement while measuring at different times of the day. This RSS difference could also be because of some other natural variable, e.g., the density of particles in the air. Moreover, with a higher intensity of ambient light (during the daytime), the PD's operation point certainly changes, which could result in a lower RSS as well. In any case, more measurements are required to model the error cause accurately. Besides, this difference is relatively small and cannot overshadow the interesting results of outdoor V-VLC.

5.4.4 Packet Delivery Ratio (PDR) over Distance

The PDR measured with each MCS for the increasing distance between the transmitter and receiver during the daytime and nighttime is presented in Figure 5.16, respectively. In the plot, a PDR of 100 % means that all packets have been correctly detected and decoded, and the horizontal dashed line marks 90 % PDR. These PDRs are measured with a fixed PD gain of 10 dB. Firstly, our prototype achieved 100 % PDR to the very end of the measurement facility, i.e., a distance of 75 m, for lower-order MCS (BPSK and QPSK) as well as for 16—QAM 1/2 regardless of the time of the day. Compared to the practical results presented in the V-VLC literature [129], such a high PDR performance over a 75 m distance in the outdoors is truly impressive. Even 16-QAM 3/4 is demonstrating close to 90 % PDR performance at a distance of approx. 70 m.

Furthermore, the external clock synchronization has eliminated the irregular drops in the PDR with 64-QAM that we observed in the indoor measurement Section 5.4.1.1. Even with 64-QAM 3/4, an over 90 % PDR is measured at distances of 50 m and 55 m at daytime and nighttime. The lower PDR performance during the daytime is essentially because of the lower RSS levels measured during this time – we already discussed the reasons in Section 5.4.3.

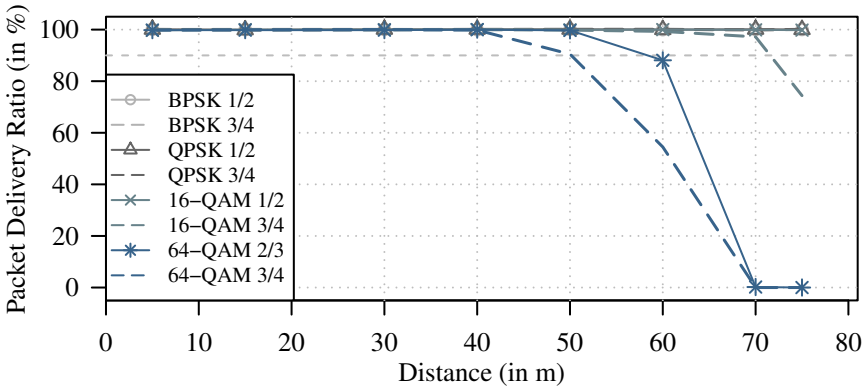

(a) PDR during daytime.

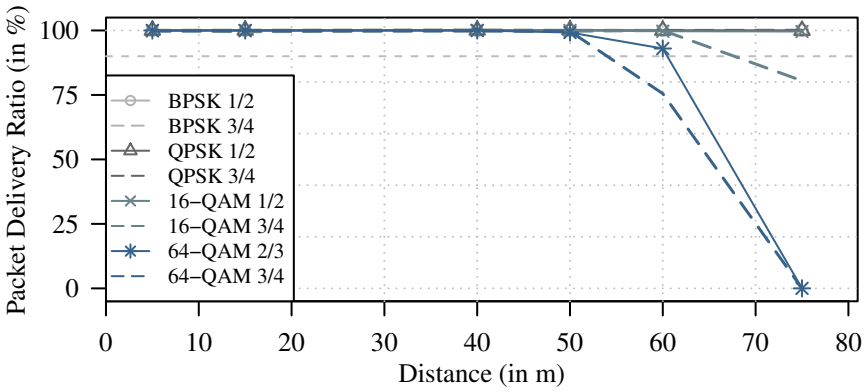

(b) PDR during nighttime.

FIGURE 5.16 – PDR performance for every MCS obtained experimentally for 1000 packets sent per transmission.

5.4.5 Packet Delivery Ratio (PDR) over Received SNR

The PDR performances of 64—QAM 3/4 and 64—QAM 2/3 against received SNR levels are shown in Figure 5.17. Both MCS achieved 100 % PDR roughly at similar SNR levels regardless of the illuminance intensity; and time of the day. The SNR required for 64—QAM 3/4 is approx. 26 dB, whereas for 64—QAM 2/3, the requirement is roughly 25 dB. The small difference between the measured SNR values is most certainly due to the measurement errors, which resulted in the deviation of RSS, as already discussed in Section 5.4.3. These SNR results help in evaluating the employed communication schemes in terms of minimum SNR requirements and assert our findings with the introduced V-VLC implementation, even in a realistic outdoor environment.

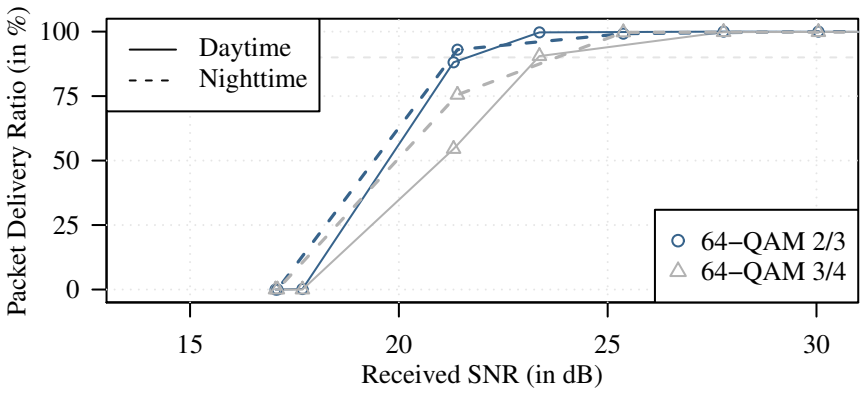

FIGURE 5.17 – PDR performance of 64–QAM at two different times of the day against received SNR, for 1000 packets sent per transmission.

5.4.6 Impact of Optics Misalignment

In the outdoor measurement campaign, we also investigated the impact of optic misalignment on the receiver's performance. Figure 5.18 depicts the impact of optics misalignment during the daytime, in terms of PDR and RSS at a distance of 40 m. It can be seen that when the misalignment angle is increased from 0° to 20°, the PDR starts to drop sharply, and the impact is much worse on higher-order MCS. Similarly, with 20° of misalignment, the RSS is dropped down by 21 dB. These results clearly underline the significance of optics misalignment and the degree to which the results can vary in the case of possible human error while doing measurements over different iterations. To reduce this sensitivity towards alignment, possible solutions

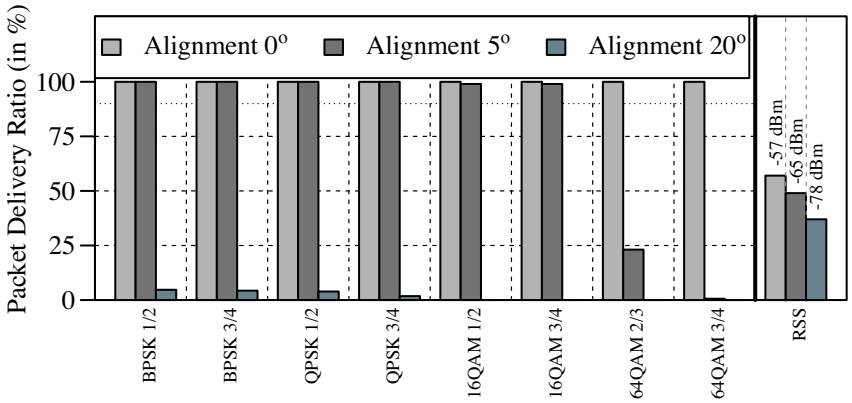

FIGURE 5.18 – Impact of optic design misalignment on PDR and RSS. The measurements are obtained during the daytime at a 40 m distance with three different alignment angles.

include the use of optics with an optimized FoV or to use multiple photo-diodes and spatial diversity techniques [130], [132], [133] to improve the received RSS.

Regardless of the sensitivity on optics alignment, the presented V-VLC prototype performed extremely well. The results clearly showed the system's capability to communicate error-free (even in bright sunlight) for over 75 m with lower-order MCS and up to 40 m with higher-order MCS. These very optimistic PDR results, especially with-lower order MCS, particularly highlight the potential of V-VLC as a complementary wireless set-up to support V2V communications.

5.4.7 Spectral Efficiency

The achievable spectral efficiency with our V-VLC prototype against the increasing distance between the transmitter and receiver for daytime and nighttime is demonstrated in Figure 5.19. Maximum spectral efficiency of 1.35 bit/s/Hz is observed with a sampling frequency of 1 MHz for up to 40 m distance. This translates to a data rate of 1.35 Mbit/s. On the other hand, the smallest observed spectral capacity is 0.6 bit/s/Hz, i.e., a bit rate of 600 kbit/s, with a sampling frequency of 1 MHz. As discussed before, this limitation of 1 MHz sampling frequency is only because of the low switching rate of the LEDs in the considered headlight. We already showed data rates as high as 8.8 Mbit/s (Figure 5.13) while operating the headlight in the low-pass region and taking advantage of high received SNR at shorter distances. Quite certainly, with high switching frequency headlights, these bit rates can be improved by a great deal. Still, compared to the V-VLC literature (e.g., [127]), the presented prototype offered at least a 6-folds increase in the achievable bit rate for considerably large distances in the outdoor conditions, regardless of the time of the day.

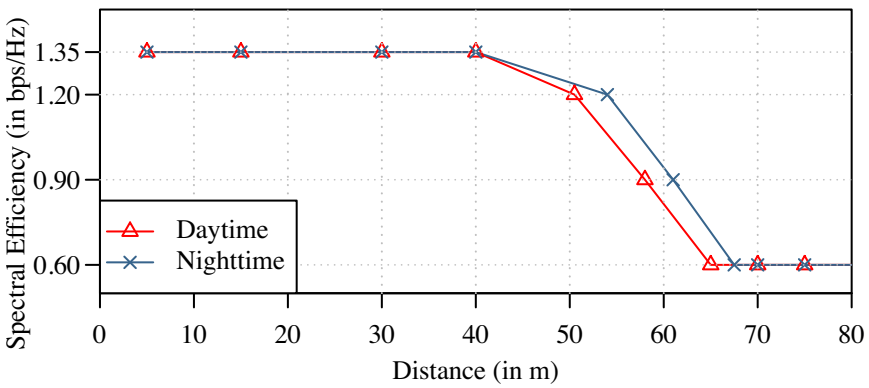

FIGURE 5.19 – Achievable spectral efficiency over increasing distance.

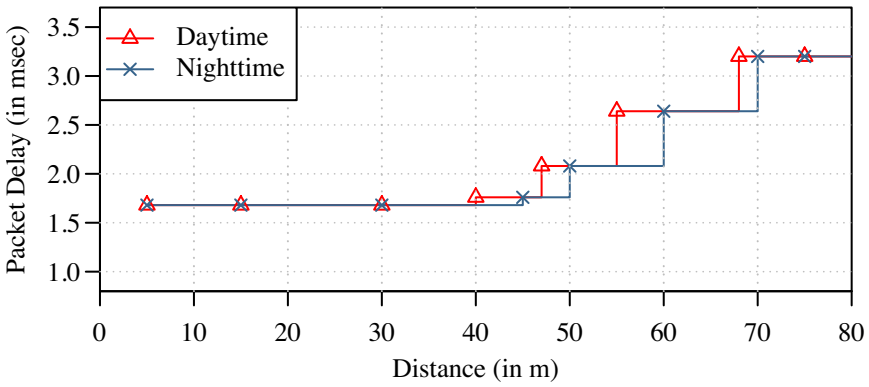

FIGURE 5.20 – PLL for increasing distances between the transmitter and receiver.

5.4.8 Physical Layer Latency (PLL)

The Physical Layer Latency (PLL) of the prototype with increasing is presented in Figure 5.20. These results are obtained for a payload of size 250 B, which is sent over the channel with different MCS. PLL is the time duration a payload engages a channel as it transverses from the transmitter to the receiver. From the figure, it can be gathered that the payload consumes a minimum channel duration of 1.7 ms for up to 40 m. Afterward, this duration increases sharply for further distances. This high PLL is due to the fact that a larger separation distance between the transmitter and receiver results in lower Received Signal Strength; consequently, a lower-order Modulation and Coding Scheme is employed to ensure the correct decoding at the receiver. A lower-order MCS needs more time-domain samples to send the same information as compared to a higher-order MCS. Intuitively, more samples imply additional channel occupation for over-the-air transmissions, and as a result, we observed higher PLL at farther distances.

5.5 Concluding Remarks

Visible Light Communication (VLC) is emerging as a potential wireless technology to complement the existing Radio Frequency (RF) technologies such as Cellular V2X (C-V2X) and Dedicated Short Range Communication (DSRC). The rapid adaptation of the Light Emitting Diodes (LEDs)-based lighting modules by the automotive industry has certainly paved the way for Vehicular-VLC (V-VLC). With the potential transmitter (head and tail light) readily available, V-VLC can be considered as cheap technology, with access to a huge, free, and unlicensed spectrum. Nevertheless, mobility and outdoor environment (e.g., ambient noise) pose challenges for V-VLC. Especially for time-critical applications with strict latency requirements, V-VLC has to

provide reliable communication, regardless of the outdoor conditions, and therefore, demands a carefully designed physical layer.

In the scope of VLC, this chapter introduced a complete V-VLC system for outdoor experimental research. Our prototype's sender side utilizes a car lighting module driven by a highly linear driver circuit; and Universal Software Radio Peripheral (USRP) configured with GNU Radio framework, which is used for baseband signal processing. The receiver side relies on simple optics, a Photo-Detector (PD) followed by a DC blocker and a USRP. The presented prototype supports OFDM with a variety of Modulation and Coding Schemes (MCSs), and it is compliant with the IEEE 802.11 standard. We showed that this setup is already quite suitable for outdoor V-VLC, even during the daytime with bright sunlight. By means of extensive outdoor measurements during the daytime, we demonstrated the system's capacity to achieve; 8.8 Mbit/s data rate for a short inter-vehicle distance of 5 m, 1.3 Mbit/s data rate for up to 40 m distances, and 600 kbit/s data rates for distances over 75 m.

In conclusion, the presented prototype can easily be used for standard-compliant V-VLC communication for typical outdoor driving scenarios. We anticipate a broad range of experiments in the field of cooperative automated driving, which can be performed on this basis. Given the flexibility of the used software and hardware components, the framework can easily be extended for further studies.

Chapter 6

Visible Light for Integrated Sensing and Communications

VISIBLE light can be used to provide illumination and to carry information, and it can be adopted for both outdoor and indoor communications. In the previous chapter, we experimentally investigated outdoor Visible Light Communication (VLC) as a potential access technology for vehicular communications that has advanced at a relatively slower pace, primarily because of more challenging environments and other constraints such as mobility and daylight. In contrast, indoor VLC has gained more attention and much faster growth, which was essentially fueled by the success of the LiFi concept. Indoor VLC has emerged as a viable complementary technology and has significant commercial potential. The recent advances in Light Emitting Diodes (LEDs) technology and its widespread usage for illumination have essentially paved the way for the realization of indoor VLC. The Line-of-Sight (LoS) communication requirement of VLC can support high precision indoor positioning, which essentially opens up a wide range of Internet of Things (IoT) applications. With the proliferating LED usage in indoors, high-density wireless *downlinks* for a large number of IoT elements can now be realized, which can reduce the traffic on the Radio Frequency (RF) spectrum. Additionally, VLC can improve communication reliability by complementing RF-based communications, especially in safety-critical and radio-hostile industrial environments.

Industrial automation is becoming a core component of the futuristic smart industries and manufacturing systems. One of the main building blocks here is the continuous health monitoring of the working machinery. At the same time, vision-based techniques for advanced sensing applications in industrial systems have gained significant attention very recently. A good example is the use of cheap low frame rate cameras combined with strobing light to non-intrusively measure the high-frequency vibrations of a machine. In this chapter, we bridge the gap between

these two concepts and propose an integrated communication and sensing system based on strobing light. We combine the sensing task with data communication using the same LED light source, which produces a low-frequency strobing signal for sensing and high-frequency pulses for communications. The combined Visible Light Communication and Sensing (VLCS) system is incredibly viable, especially for industrial automation. The main challenge in the joint system, however, is to maintain a constant energy envelope of the strobing signal for accurate camera-based frequency detection. Our system can reproduce the same signal envelope while VLC is in operation, thus, hiding communications from the camera-based sensing. We further explore the capability of our system and consider spatial diversity techniques using multiple Photo-Detector (PD) receivers to improve both the communication reliability and the energy footprints at the receiver. Finally, we go one step further and integrate the idea of preamble-less communication proposed as mSync with spatial diversity to further minimize the transmission energy. We investigate the fully-featured combined system's performance using a GNU Radio implementation. Our results demonstrate the huge potentials of the proposed VLCS system for the application, e.g., in industrial environments.

The rest of the chapter is based on the following peer-reviewed publications:

- **M. Nabeel, M. S. Amjad, and F. Dressler, "Preamble-Less Diversity Combining: Improved Energy-Efficiency in Sensor Networks," in *IEEE Global Communications Conference (GLOBECOM 2018)*, Abu Dhabi, United Arab Emirates: IEEE, Dec. 2018.**

  In this conference paper, my contributions were: the successful integration of the preamble-less communication with the receive diversity in a distributed antenna system; implementation of the complete system in GNU Radio framework; extensive real-time simulative and experimental evaluation with Software-Defined Radios (SDRs) supporting the concept, the achievable performance gain, and possible energy conservation.

- **M. S. Amjad and F. Dressler, "Integrated Communications and Non-Invasive Vibrations Sensing using Strobing Light," in *IEEE International Conference on Communications (ICC 2020)*, Virtual Conference: IEEE, Jun. 2020.**

  In this conference paper, my contributions were: the analytical study of the proposed novel idea of the integrated system for simultaneous communications and non-invasive vibrations sensing for potential fault/failure detection; the simulative evaluation of both communication and sensing performance; exploring the spatial diversity techniques for improved performance.

- **M. S. Amjad and F. Dressler, "Using Visible Light for Joint Communications and Vibration Sensing in Industrial IoT Applications," in *IEEE International Conference on Communications (ICC 2021)*, to appear, Montreal Canada: IEEE, 2021.**

  This conference paper extended the previous work with the following contributions: the evaluation of the VLCS system as a potential candidate for industrial IoT applications, performing communications and vibrations sensing for structural health monitoring; the utilization of dark-period of the LEDs to further improve the communication throughput; the comparison of joint VLCS system with the individual VLC and Visible Light Sensing (VLS) systems for performance evaluation.

6.1 Motivation

Vision-based monitoring of objects such as structures, machines, etc., for safety purposes, has gained significant attention [134]. Such monitoring is not only needed to detect anomalous behavior that can result in potential breakdowns but also for the continuous optimization of the operating parameters (e.g., machinery in an industrial operation) for maximum performance throughput. These indicators can provide a comprehensive picture of a machine under inspection, which certainly helps during inspections to identify whether it is fully operational/functional/safe-to-use. If deterioration is detected, it requires immediate attention, and it should be replaced/resolved; any negligence can potentially lead to severe health and safety risks.

In this regard, the analysis of vibrations is extensively used as the first indicator of possible faults/failures. The spectral analysis of vibration signals from an object, e.g., a machine with rotating parts, can provide useful insights into its mechanical conditions and working [27]. This approach, in particular, can be utilized in industrial IoT for smart maintenance [135]. Nevertheless, these vibrations are typically measured using contact-based velocity or accelerometer sensors. Such sensors must be mounted on the object under investigation and thus pose operational and deployment challenges, especially in high-risk environments, such as high-temperature, high-pressure, or radioactive areas within a plant.

Recently, Roy et al. [27], [28] experimentally demonstrated an alternative vision-based technique, which utilizes a commodity low Frames Per Second (FPS) camera to measure high-frequency vibrations using strobing light. Produced from a light source, the strobing signal is a narrow width pulse with adjustable frequency in the visible light spectrum. This strobing pulse optically samples the object/machine under observation, which effectively modulates the vibration signal, and shift the frequency components (by exploiting the frequency folding phenomenon) within

the Nyquist frequency of the low FPS camera. The detection/analysis of machine vibrations in an industrial environment (illustrated in Figure 6.1) can essentially be used for smart maintenance and continuous optimization of the operating parameters in a machine, and hence, for optimal production throughput.

From the perspective of smart industries, continuous monitoring of machines for control and safety purposes has always been a key concern and gained significant attention in fully-automated environments [135]. Over the last years, there is a growing trend towards IoT technologies, which have matured significantly and have transformed many working fields in our society through the realization of smart grids, smart manufacturing, and smart cities [136]. In particular, the incorporation of Cyber-Physical Systems (CPS) for smart manufacturing in industrial automation has reshaped the production mode from digital to intelligent. In this regard, industrial IoT networks aim to connect almost everything in the automation process. As a result, the network is expected to have ubiquitous coverage connecting an increasing number of devices per unit area leading to a substantial aggregated bandwidth. Conventional communication in the highly exhausted radio frequency spectrum often experiences severe channel degradation and electromagnetic interference in radio-hostile industrial environments [137], [138]. This impedes the optimal performance of industrial IoT networks, which can potentially cause a significant reduction in manufacturing productivity or even physical and economical damages [138].

With the recent advances in LED technology and its widespread adaptation for illumination, indoor VLC has been materialized as an access technology, which can be integrated with IoT for novel networking solutions [24]. The proliferating LED usage can offer high-density wireless *downlink links* for a large number of IoT elements that

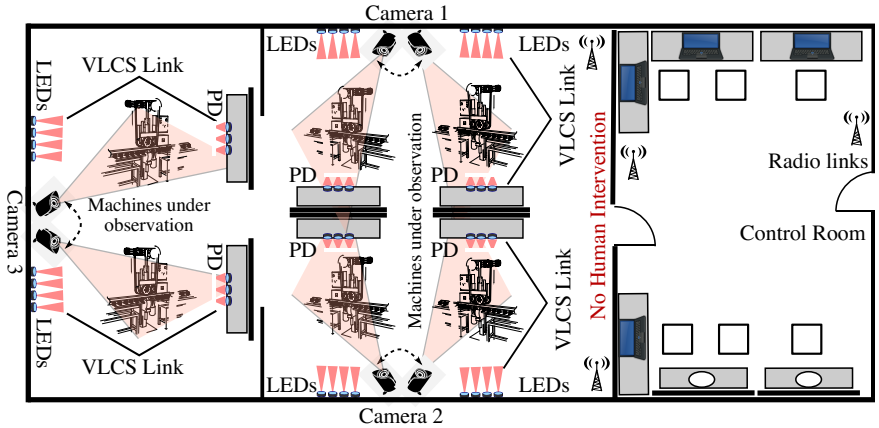

FIGURE 6.1 – Joint Visible Light Communication and Sensing (VLCS) systems in radio-hostile / high-risk environment for smart industrial IoT, where each low-FPS camera is utilized for sensing vibration measurements of multiple machines.

can reduce the traffic on the RF communication spectrum [26]. Additionally, VLC can improve communication reliability by complementing RF-based communication systems in radio-hostile industrial environments. Besides the predominant utilization of visible light for communication purposes, it can together be utilized for the non-invasive visible-light based sensing in smart industrial applications.

This capacity of visible light to perform both sensing and communications can be exploited in an integrated fashion to mutually benefit from each other, i.e., utilizing the same sensing signal for communications as well. In this chapter, we, therefore, bridge this gap between the two domains and propose an integrated system for simultaneous communications and non-invasive sensing of an object's vibrations, i.e., the VLCS system. We implement the communication part, which essentially uses BPSK modulator/demodulator, and emulate the sensing part to detect the frequencies – with and without the communication signal jointly in the GNU Radio framework. To improve the system's communication performance, we further look into spatial diversity approaches together with preamble-less communications via mSync implementation. We also explore Dark Period Communication (DPC) to fully exploit the same LEDs for communications, even during the *OFF-Time* of the strobing pulse, in order to improve the system's throughput. Using both the *ON*- and *OFF-time* substantially improves communication throughput and makes the system viable for industrial IoT applications.

The core contributions of this chapter can be summarized as follows:

- For the first time, we present and investigate an integrated Visible Light Communication and Sensing (VLCS) system as a potential candidate for industrial IoT applications, performing communications and vibrations sensing for structural health monitoring.
- We investigate the impact of the sensing signal on the communication's performance and study the error in the envelope of the resultant combined strobing signal, which is s below -50 dB. We also analyze the detected frequencies with the VLCS system, where the absolute error is below -35 dB.
- We also consider spatial diversity in the proposed system to improve the energy footprints and further incorporate preamble-less diversity combined with mSync architecture to reduce the transmission energy requirements.
- We use DPC to further improve the communication throughput and, at the same time, investigate its impact on the frequency sensing capacity of the VLCS system.
- We compare the joint VLCS system with the individual VLC and VLS systems and show that, although there is slight performance degradation in the VLCS system, the potential gains outweigh these small losses.

6.2 Related Studies

Contact-based velocity and accelerometer sensors are often the first choices for the vibration measurement of an object, e.g., structures and machinery. However, these sensors not only pose deployment and operational challenges in high-risk locations but also result in additional time and expenses for the collection of measurement data. Contact-less vibration sensing approaches such as Laser Doppler Vibrometer (LDV) [139] and Near-field Acoustic Holography (NAH) [140] either measure the pressure readings of the vibrating surface or utilize a group of highly synchronized lasers for the frequency estimation. Although these approaches offer precise vibration frequency estimates, the equipment is rather expensive, and the estimation time increases with the size of the object.

Recently, vision-based vibration estimation techniques have emerged as an attractive at-a-distance measuring alternatives [141], [142]. These contract-less approaches perform image processing on a series of frames captured by a camera and provide compelling vibration frequency estimates. Nevertheless, to precisely measure high-frequency vibrations, specialized/expensive high FPS cameras are required to avoid aliasing problems. The high-frequency vibrations through a low FPS camera have been experimentally measured by exploiting the optical strobing phenomenon [27]. The work considered a strobing light signal with adjustable frequency to optically sample the object under observation, which effectively modulates the vibration signal and shifts the frequency components within the Nyquist frequency of the low FPS camera.

In recent years, structural health monitoring of machines in smart industries is an important aspect that has received significant attention, where machine vibrations are typically used as the first indicator of a possible breakdown and, thus, fault detection [135]. The vision-based non-invasive machine analysis, together with the incorporation of IoT in CPS-based smart grids, industrial controls, and automation, can potentially provide the ultimate automation. Nevertheless, such extensive wireless networks with aggregated bandwidth demand high spectrum availability for low latency communications, i.e., less channel congestion. With widespread utilization of LEDs in indoors and the emerging Visible Light Communication technology with wide available spectrum in the visible light promises to overcome these limitations of RF resources, especially in the densely populated radio spectrum due to the huge aggregated bandwidth of the connected devices.

For the indoor VLC, an extensive fundamental analysis is provided in [143]. The work in [144] considered the input signal constraints to derive the capacity bounds of VLC in indoor channels. In [143], [145], the Asymmetrically Clipped Optical OFDM (ACO-OFDM) and the Direct Current-Biased Optical OFDM (DCO-OFDM) are evaluated for VLC, respectively. The first GNU Radio-based prototype of IEEE

802.15.7 standard for short-range VLC has been introduced in [125]. In [146], an LED-based indoor broadband wireless system has been proposed achieving a data rate as high as 1 Gbit/s. Other works, such as [24], [147], have presented an energy-efficient variant of VLC, the darkVLC, where the data is sampled with very high sampling frequency and encoded onto very brief, imperceptible light pulses for bandwidth-efficient DPC networks. In [148], [149], multiple access techniques that meet the multi-rate and delay tolerance requirements in VLC-based IoT networks have been investigated in order to address the diverse traffic characteristic in different IoT applications.

Given the fact that visible light has been utilized for non-invasive sensing and wireless communication for IoT applications, this work combines the two domains. This integration of two techniques, i.e., VLS and VLC, essentially means that the same light source performs both tasks, where the VLC is added on top of the strobing signal. This certainly changes the resultant strobing signal envelope, which is read by a camera device; however, for an effective VLS using strobing light, a steady envelope of the strobing light source is required. Thus, the degree to which a strobing signal can manage the added communication signal is a major challenge; and this is exactly what we are going to analyze in this chapter, among other performance metrics.

6.3 Optical Strobing for Sensing Applications

When a vibrating object is illuminated with some external periodically strobing light source and monitored continuously, it results in a different presentation of the motion, i.e., the visual appearance of that object to a viewer changes over time. A frame-to-frame comparison of that illuminated object (via image processing tools) provides the temporal speed of the change in presentation. This temporal speed and object position information can be further utilized to estimate the unknown vibrational frequency of that object to a great precision [27]. By exploiting this optical strobing phenomenon to measure any changes in the vibrational frequency of an object, it becomes possible to unobtrusively detect system faults/failures. Such unobtrusive detection is especially beneficial in automated and hostile industrial environments requiring the least human intervention.

6.3.1 Strobing Principle

Strobing light is a low frequency narrow-width periodic light pulse [150], and it is used for recurring illumination, as illustrated in Figure 6.2. These pulses are used to turn on LEDs panel, which illuminates the object under observation periodically for short durations, i.e., the optical sampling. The optically sampled object $m_s(t)$ can

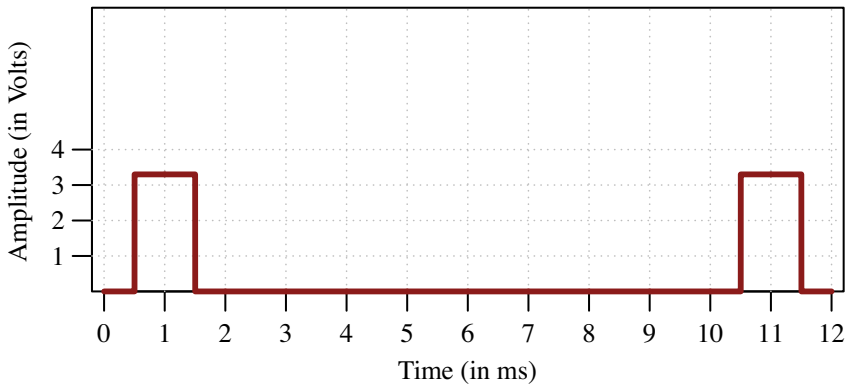

FIGURE 6.2 – Strobing pulses used to optically sample the object under observation.

be expressed mathematically as

$$m_s(t) = m(t) \times c(t), \tag{6.1}$$

where $m(t)$ is the object with unknown vibrational frequency, and $c(t)$ is the infinite strobing optical pulse train, i.e., $c(t) = \sum_{n=-\infty}^{\infty} \delta(t - nT_s)$, of known period T_s. The Fourier domain representation of Equation (6.1) can be written as

$$M_s(\omega) = \frac{1}{2\pi}[M(\omega) \circledast \frac{2\pi}{T_s} \sum_{k=-\infty}^{\infty} \delta(\omega - k\omega_s)], \tag{6.2}$$

where ω_s is the optical sampling frequency, and k is of integer nature. The optically sampled signal $G_s(\omega)$ for VLS is obtained as

$$M_s(\omega)_{\text{VLS}} = \frac{1}{T_s} \sum_{k=-\infty}^{\infty} M(\omega - k\omega_s). \tag{6.3}$$

A low FPS camera captures the resulting sampled signal with a frame rate ω_{cam} that effectively acts as a low-pass filter. The camera (aligned with the LED panel) sends the captured video of the object to *MATLAB* for image processing. The *MATLAB* performs a frame-to-frame analysis of the video to extract temporal speed and position information for further estimation of the vibrational frequency of that object.

6.3.2 Strobing Condition

Using the Nyquist sampling criterion, the condition of aliasing-free strobing can be defined as

$$2 \times |\omega - k \times \omega_s| \leq \omega_{\text{cam}}, \tag{6.4}$$

This condition certainly bounds the detectable vibrational frequency range with ω_{cam}, which, for a cheap low FPS camera, is already quite small. Nevertheless, we can deliberately alias the periodic signals by sampling them with a frequency that is very close to the fundamental frequency. The frequency folding phenomenon as a result of this intentional aliasing shifts the sampled periodic signal spectrum within the range of ω_{cam}. Thus, the aliased frequency will fall within the low-pass behavior of the camera ω_{cam} only, if the following condition is satisfied:

$$2 \times ||\omega - k \times \omega_s| - \omega_{\text{cam}}| \leq \omega_{\text{cam}}, \tag{6.5}$$

Hence, if k can be estimated, the unknown vibration frequency ω can be calculated.

6.3.3 Combined Light Strobing with VLC

For the integrated VLC and VLS, we add the communication signal on top of the strobing signal, as shown in Figure 6.4. Since the sampling frequency for the communication signal is over ten thousand times higher than the strobing signal, it is expected not to distort the optical sampling pulse. Additionally, we utilize the dark period of the strobing signal for communications as well. We study and demonstrate the impact of adding the communication signal on the strobing pulse and vice versa in the following section, both mathematically and via real-time simulation experiments.

6.4 Modeling of VLCS System

Figure 6.3 presents a detailed model with both VLC and VLCS systems in an industrial environment. The simple VLC system is used for the remote *uplink* communications, whereas the VLCS system is utilized for both remote *downlink* communications and unobtrusive vibration sensing of machines.

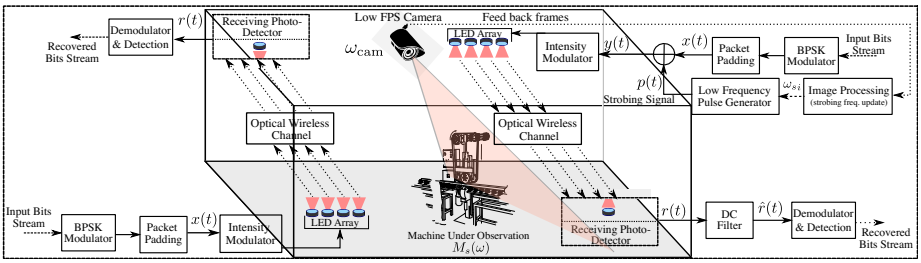

FIGURE 6.3 – Detailed model of both VLCS and VLC systems for the *downlink* and *uplink* communications in an industrial environment, respectively.

6.4.1 Communication Model

For the *downlink* communications, i.e., VLCS system (see Figure 6.3), the bit-stream to be sent is differentially BPSK modulated first $x(t)$ and then added with the sensing signal pulse $p(t)$ to obtain the resultant signal $y(t)$ as

$$y(t) = x(t) + p(t). \tag{6.6}$$

The combined signal $y(t)$ is then Direct Current-Biased Optical (DCO) modulated onto an LED panel containing an array of 10 LEDs and sent over the optical channel.

The *downlink* receiver is a PD, which translates the light intensity into an electrical signal $r(t)$ and can be mathematically expressed as

$$r(t) = \alpha(x(t) + p(t)) + n(t), \tag{6.7}$$

where α is the attenuation coefficient due to optical channel propagation losses and $n(t)$ is the Additive White Gaussian Noise (AWGN) with zero mean. To decoupled the DC bias from the received signal due to DCO modulation, a DC filter $h(t)$ is used. The resultant signal $\hat{r}(t)$ can then be expressed as

$$\hat{r}(t) = h(t) \circledast (\alpha x(t) + \alpha c(t) + n(t)). \tag{6.8}$$

The small ripple effect as a result of the strobing signal's DC filtering generates residual noise $n_{\text{dc}}(t)$ and slight distortion in $x(t)$, reducing Equation (6.8) to

$$\hat{r}(t) = \alpha\hat{x}(t) + n_{\text{dc}}(t) + n(t). \tag{6.9}$$

Here, we assumed that the distortion in $x(t)$ is close to negligible, i.e., $\hat{x}(t) \approx x(t)$. The DC filtered signal $\hat{r}(t)$ is then demodulated and decoded to recover the sent bit-stream. Notice that, in the case of the *uplink* VLC system – there is no sensing signal, i.e., $n_{\text{dc}}(t) = 0$.

From Equation (6.9), the instantaneous Signal-to-Noise Ratios (SNRs) for a VLCS system γ_{VLCS} and a VLC system γ_{VLC} for both *downlink* and *uplink* communications can be computed as

$$\gamma_{VLCS} = \frac{\alpha^2 \cdot P_s}{\sigma^2 + \sigma^2_{\text{dc}}}, \quad \text{and} \quad \gamma_{VLC} = \frac{\alpha^2 \cdot P_s}{\sigma^2}, \tag{6.10}$$

where $E\{|x(t)|^2\} \approx E\{|\hat{x}(t)|^2\} = P_s$ is the instantaneous signal power, $E\{|n_{\text{dc}}(t)|^2\} = \sigma^2_{\text{dc}}$ is the noise power due to the DC filtering of the strobing pulse, and $E\{|n(t)|^2\} = \sigma^2$ is the AWGN power. Essentially, the SNR loss Γ_{L} in VLCS because of σ^2_{dc} can be

presented as

$$\Gamma_{\mathrm{L}} = \gamma_{\mathrm{VLCS}}/\gamma_{\mathrm{VLC}} = \frac{1}{1+\sigma_{\mathrm{dc}}^2/\sigma^2}. \tag{6.11}$$

In Equation (6.11), for very small values of σ_{dc}^2, the SNR loss $\Gamma_{\mathrm{L}} \approx 0$, i.e., the communication performance of VLCS system is roughly the same as VLC system.

6.4.2 Sensing Model

The low-FPS camera capturing the illuminated object's frames performs the sensing task in the VLCS system, as depicted in Figure 6.3. The sensing model here studies the impact of communications signal on the strobing signal, and eventually on the non-invasive sensing task. The impact is specially modeled for the case when the communications signal is added to the dark period of the strobing signal. In such a VLCS system, the communication signal $x(t)$ can be expressed as a sum of $x_{\mathrm{SL}}(t)$ and $x_{\mathrm{DP}}(t)$. The $x_{\mathrm{SL}}(t)$ is the portion of $x(t)$ that is communicated only on the Strobing Light (SL) pulse, and the $x_{\mathrm{DP}}(t)$ is the remaining portion of $x(t)$ that is sent over the Dark Period (DP), i.e., communicated during the *OFF-Time* of the strobing light pulse, as depicted in Figure 6.4.

The object that is optically sampled with such a combined strobing light signal can be mathematically modeled as

$$m_s'(t) = m(t) \times (x_{\mathrm{SL}}(t) + x_{\mathrm{DP}} + p(t)). \tag{6.12}$$

The Fourier domain representation of (6.12) can be obtained as

$$M_s'(\omega) = \frac{1}{2\pi}[M(\omega) \circledast (X_{\mathrm{SL}}(\omega) + X_{\mathrm{DP}}(\omega)) + M(\omega) \circledast P(\omega)]. \tag{6.13}$$

This sampled object $M_s'(\omega)$, is captured by a low-FPS camera with a low-pass behavior, which filters out the high-frequency communication signal $x(t)$. Using Equation (6.3), the optically sampled signal in VLCS system can be written as

$$M_s'(\omega)_{VLCS} = M_s(\omega)_{VLS} + N_{\mathrm{SL}}(\omega) + N_{\mathrm{DP}}(\omega), \tag{6.14}$$

where $N_{\mathrm{SL}}(\omega)$ and $N_{\mathrm{DP}}(\omega)$ are the filtered residual noises. It is worth noticing here that when there is no communication during the dark period of the strobing signal, then the VLCS is expected to have less noise in general, and incorporating the Dark Period Communication (DPC) can have a slight negative impact on the sensing performance of the VLCS system.

The resulting error in the optically sampled object due to the added communication signal can be computed as

$$||e_{err}||^2 = ||M_s'(\omega)_{VLCS} - M_s(\omega)_{VLS}||^2 = ||N_{\mathrm{SL}}(\omega) + N_{\mathrm{DP}}(\omega)||^2. \tag{6.15}$$

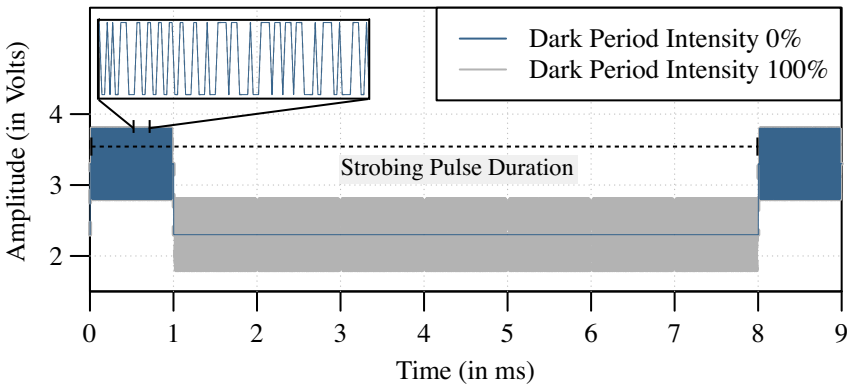

FIGURE 6.4 – The strobing light signals in the VLCS system with two different DPC intensities. DPC 0 % means $x_{\text{DP}}(t) = 0$, and DPC 100 % means communications over the entire strobing pulse duration.

Notice that when $\{N_{\text{SL}}(\omega), N_{\text{DP}}(\omega)\} \rightarrow 0$, the sensing performance of the VLCS system approaches to a typical VLS system.

6.4.3 Optical Wireless Channel

The fundamental characteristics of the optical wireless channel highly depend on the optical link design, configuration, and topology [151]. Optical wireless systems are typically classified according to the degree of directionality between the optical transmitter and receiver, the existence of a continuous line-of-sight path, the divergence angle of an optical transmitter, and the field-of-view of an optical receiver. For such a classification, the propagation in an optical wireless channel can be expressed

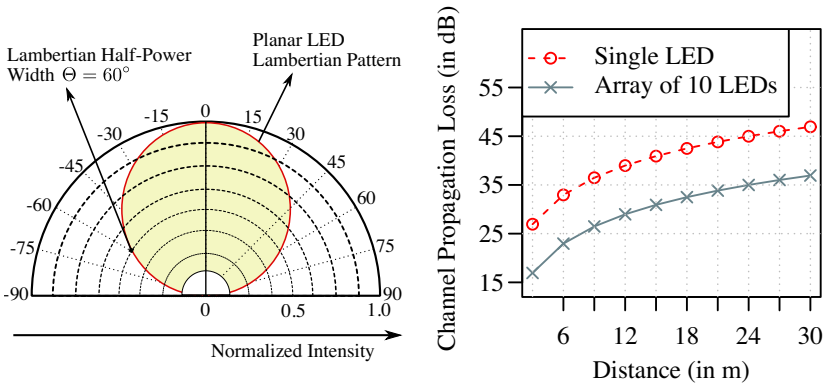

(a) Lambertian (LED) radiation pattern.

(b) Optical propagation loss.

FIGURE 6.5 – Optical propagation loss over increasing distances in the free-space for Lambertian pattern-based single LED and an array of 10 LEDs.

as

$$P_r = P_s \cdot G_{Tx} \cdot G_d \cdot G_{Rx} \cdot A_{losses}, \tag{6.16}$$

where P_r is the received signal strength, P_s is transmitted signal power, G_{Tx} is the optical transmitter gain, G_{Rx} is the optical receiver gain, G_d is the light intensity depreciation over distance, and A_{losses} are the system-dependent losses due to the design and configuration.

The optical transmitters, such as LEDs, are typically designed to have a spatial luminous intensity that follows Lambertian beam distribution (cf. Figure 6.5a). With a Lambertian beam under-filling the transmitting aperture and a typical PD for absorbing the light, the optical transmitter-receiver gains along with propagation loss [152] can be calculated as

$$G_{Tx} = \frac{32}{\Theta^2};\;\; G_{Rx} = \left(\frac{\pi D}{\lambda}\right)^2;\;\; G_d = \left(\frac{\lambda}{4\pi \cdot d}\right)^2,$$

where Θ is the full-angle transmit beam divergence (in rad), D is the diameter of the optical receiver aperture, d is the distance between the optical transmitter-receiver system, and λ is the wavelength. After substitution of the values of the gains, Equation (6.16) can be written as

$$P_r = P_s \cdot \frac{2D^2}{\Theta^2 d^2} \cdot A_{losses}, \tag{6.17}$$

with free-space propagation loss (α) being computed as

$$\alpha = \frac{2D^2}{\Theta^2 d^2} \cdot A_{losses}, \tag{6.18}$$

In Equation (6.18), it can be seen that besides the distance between transmitter and receiver, the attenuation coefficient α also depends on the transmitter beamwidth and the receiver's aperture diameter. A wider beam divergence further increases the α, and a larger aperture reduces the attenuation coefficient as it can absorb more light.

The far-field pattern generated by an LED defines its maximum intensity region. Typical LEDs with Lambertian pattern (cf. Figure 6.5a) have an angular intensity distribution which is maximum near 0°, and reduces to 50% at an angle of 60°, thus, having a theoretical half-power beamwidth at $\Theta = 120°$. An LED with such divergence angle for transmissions and an optical receiver/detector with an aperture diameter of 0.3 m; the free-space optical propagation loss over distance is obtained as shown in Figure 6.5b. The propagation loss shown in the plot does not include system-dependent losses A_{losses}. These propagation loss values over distance are

later used in Section 6.6.1 to model the free-space optical channel for simulative evaluation purposes.

6.5 Implementation Details

For the evaluation of our VLCS system, both the communication and sensing parts are implemented in GNU Radio framework.[5] The GNU Radio signal processing platform supports both real-time and offline simulation experiments. Our VLCS system comprises of two parts:

6.5.1 Communications

The communications part of the VLCS system is further divided into three parts:

6.5.1.1 Transmitter

The system implements differential BPSK for baseband modulation/demodulation of the input bit-stream (cf. Figure 6.3). A packet padding block is used in the implementation to control the DPC intensity (ranging from 0 % to 100 %) in the integrated VLCS system. The padded stream is then added with the strobing signal, which is intensity-modulated (also simulated in GNU Radio) for the optical transmission.

6.5.1.2 Channel

For the optical wireless channel, we have used the model presented in Section 6.4.3, for a 10×1 LED panel, a beamwidth $\Theta = 120°$, and a PD aperture diameter of 30 cm. The resultant free-space propagation loss over increasing distance is plotted in Figure 6.6a to compare both a single LED and the 10×1 LED panel losses.

6.5.1.3 Receiver

In the VLCS system receiver, a DC-filter is required between the PD and the receiving chain to filter out the strobing signal $p(t)$. The non-ideal design of the DC-filter essentially causes a ripple effect, creating some remnant noise σ^2_{dc} and distortion, as discussed in Section 6.4.1. This impact of DC-filter noise is also shown in Figure 6.5b, where clearly, the SNR loss Γ_l (obtained in Equation (6.11)) increases as soon as the DC-filter noise σ^2_{dc} surpasses the AWGN noise σ^2.

Additionally, we also implemented spatial diversity at the receiver with three PDs providing receive diversity gain. The three PDs are also connected with DC-filters to decouple the DC bias due to DCO modulation. The output of the DC-filters are

[5] https://www.gnuradio.org/

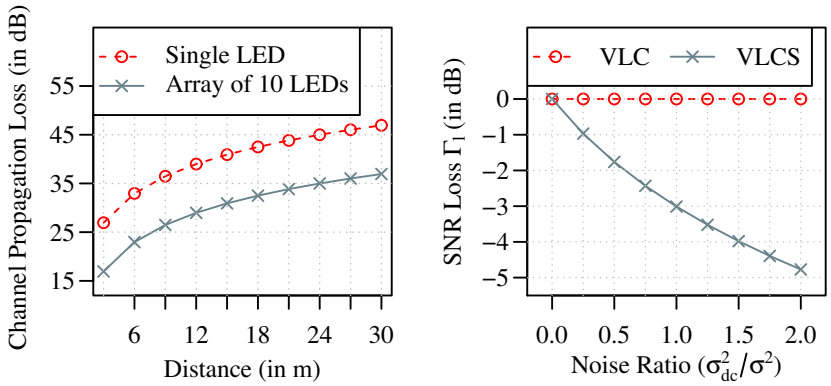

(a) Channel propagation loss in VLC.

(b) Impact of increasing DC filter noise.

FIGURE 6.6 – Optical propagation loss over increasing distances in the free-space for Lambertian pattern-based LEDs, and the SNR loss (Γ_l) due to increasing DC-filter noise.

combined using Equal Gain Combining (EGC) technique, i.e., the data from all branches is combined after co-phasing to achieve diversity gain. Next, clock recovery is required, for which we have used the GNU Radio's built-in *Mueller and Müller* block that implements a two taps feedback system to estimate the sampling clock and frequency offsets [153]. Further details of this algorithm and its impact on mSync have been discussed in [154]. Finally, decoding is performed to recover the sent bit-stream.

6.5.2 mSync with Spatial Combining

To reduce the energy requirements with the communications part of the VLCS system, we further applied the concept of mSync [154] in the proposed system.

In wireless sensing networks, the communication is usually packet-based, and the packet structure on the physical layer typically includes a preamble, a Start of Frame Delimiter (SFD), the actual data, and a Cyclic Redundancy Check (CRC). The preamble is a repeating sequence used to detect a signal at the receiver and estimate symbol timing, sampling clock offset, and frequency offset. With these estimated parameters, the receiver clock is synchronized with the transmitter to decode the received data coherently. SFD is also similar to the preamble in the structure; however, its last bit normally breaks the flow of repeating sequence to identify the start of actual data, assuming that the clocks are already synchronized.

mSync is designed to eliminate this preamble from the packet structure to reduce the overall packet-length; however, this breaks state-of-the-art receiver structure with serious implications on signal detection and further processing.

6.5.2.1 mSync

With no preamble sequence in the packet structure, mSync uses the SFD in a unique fashion to estimate clock parameters. In brief, the mSync [154] transmitter sends packets in flipped bit-order, starting from CRC and ending with SFD. On the other hand, the receiver performs a correlation of the incoming data with flipped SFD and keeps storing the samples in a buffer equivalent to the packet size. In the case of a positive detection, the stored samples are then appended at the end of the received packet in reversed (now correct) order. Thus, the clock module first receives the flipped data with back-to-back SFDs serving as a longer training sequence and then the data; in the correct order. The clock module initiates coarse timing recovery from the flipped data and then further refines it through concatenated SFDs. The receiver structure after clock recovery remains unchanged as the flipped data is discarded by the decoder.

6.5.2.2 Novel Preamble-Less Diversity Combining

Our novel concept integrating mSync and receive diversity is depicted in Figure 6.7. In essence, the transmitter structure of mSync [154] is kept, and the receiver is extended with the receive diversity combining denoted as the addition sign in the figure. In the event of signal detection at multiple receiving elements, the adder coherently combines these signal copies before appending the buffered packet in the correct order. It is important to mention here that these detections are an important part of a diversity system due to the fact that higher gain is only achieved by combining the signal copies, which are detected but not recovered at a single antenna.

Since mSync eliminates the preamble; and detections are performed with SFD only, first, we needed to assess its packet detection rate. To test this performance, we

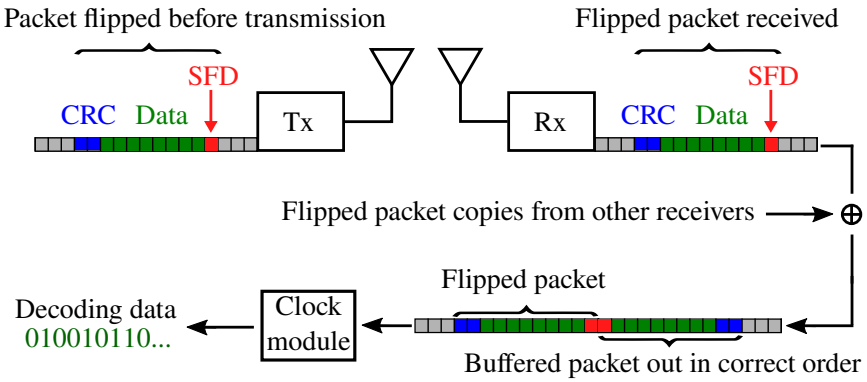

FIGURE 6.7 – Combining mSync and receive diversity, © 2018 IEEE [155].

used the BATS transceiver described in [154] and simulated the detections as well as reception quality over different SNR values in an AWGN channel. In brief, we periodically transmitted a Differential Binary Phase-Shift Keying (DBPSK) modulated packet of 12 B that contains 1 B each for preamble and SFD, 2 B of CRC, and the remaining 8 B for the actual data. This translates into 8.3 % of the preamble for the total packet length. First, we simulated the performance with normal packet structure and then with mSync based flipped packet format without preamble. The results demonstrating the number of successfully detected and correctly decoded packets with each packeting format are plotted in Figure 6.8.

As can be seen, packets can be detected at an SNR that is 4 dB less than that required for correct decoding of the packets. This was a promising result, which motivated the use of receive diversity to constructively combine the samples of detected packets from all receiving branches that can further improve their quality. Additionally, we were interested to see the effect of performing phase alignment for constructive combining of signals in the mSync packet format through SFD only.

Looking from a different perspective and considering the performance plot of correctly decoded packets, we confirmed the findings in [154] that there is no performance drop; however, there are significant energy savings. It is also interesting to note that at higher SNR values, mSync performs better than the normal packet structure. This is because of the additional coarsely grained tuning of clock parameters from flipped data samples prior to the fine timing recovery via two back to back SFDs, as discussed in [155] with more real-world experimental insights. At the same time, we can see a performance drop in signal detection with mSync, essentially because the detection is only performed with SFD, i.e., no preamble.

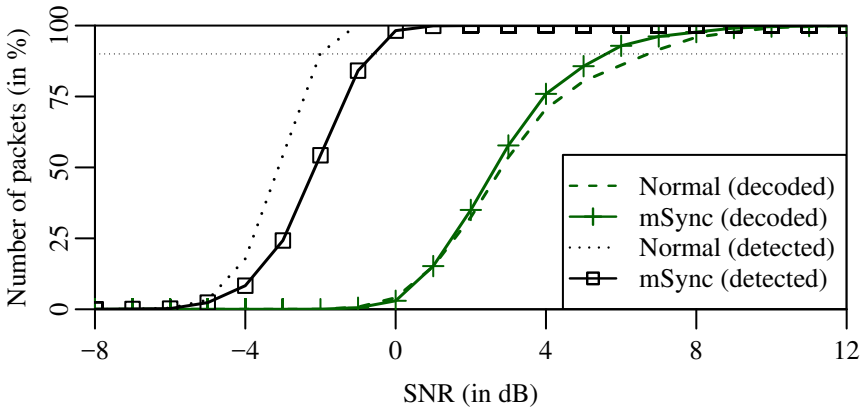

FIGURE 6.8 – Packets detected vs. correctly decoded over an AWGN channel, © 2018 IEEE [155].

6.5.2.3 Transmitter and Receiver Design Variations for mSync

The extension of our transmitter implementation for mSync only includes an encoder that first generates reversed (or mirrored) packets of 11 B and then modulates them using DBPSK. The rest of the transmitter design stays the same.

At our receiver side, after the DC filtering, the packets are first detected by correlating the received samples with the flipped SFD. In the case of successful detection, the phase offset is estimated from the available 1 B of SFD and compensated for constructive diversity combining. After phase compensation, the stored packet samples are flipped and appended at the end (as shown in Figure 4.2). With such a packet structure, the clock recovery module first performs coarse timing recovery through the flipped payload and then does fine recovery using two back to back SFDs. For the clock recovery, the GNU Radio's built-in *Mueller and Müller* block is used. Finally, the receiver performs decoding and a CRC check; to ensure successful receptions.

6.5.3 Sensing

For effective sensing of vibrations, a steady envelope of the strobing light signal is the primary requirement. Especially in DPC, where the communication is performed throughout the strobing signal duration, the impact of combined signal in VLCS on the sensing is an interesting and the first step to consider. For this reason, we first analyzed the difference in envelopes of the strobing signals in both VLCS and pure VLS systems as

$$||\mathrm{E}||^2 = ||\mathrm{Envelope} < y(t) > - \mathrm{Envelope} < p(t) > ||^2. \tag{6.19}$$

Figure 6.9 demonstrates the difference between the envelopes of the VLCS and VLC strobing signals. In the plot, the mean error value is below −50 dB, which is negligibly small and shows how little is the impact of the added communication

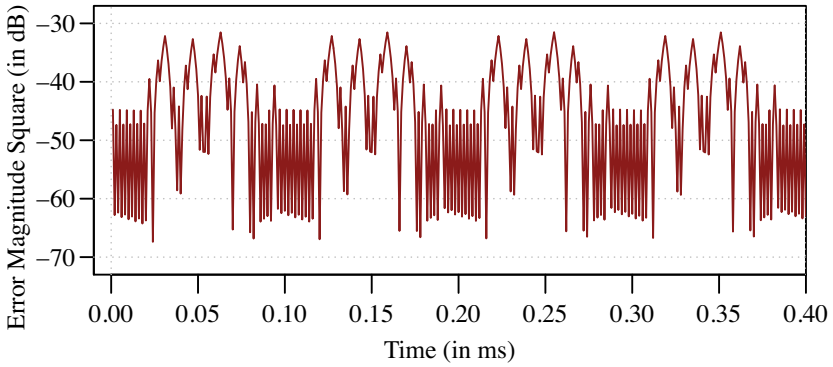

FIGURE 6.9 – Error between the envelopes of VLCS and VLS strobing signals, © 2020 IEEE [156].

signal in the VLCS system on a strobing pulse. This particularly ensures the capacity of the joint VLCS system to effectively perform both communications and sensing. With a steady envelope in VLCS even with the DPC, in the second step, we extend the sensing evaluation with an emulated low FPS camera behavior within GNU Radio.

6.6 Performance Evaluation

For the performance evaluation of the proposed combined VLCS system, we conducted extensive real-time simulation experiments. In the simulation experiments setup, we transmitted 1000 differentially modulated BPSK packets with different intensities of Dark Period Communication (DPC). The considered packet structure has a 1 B preamble, 1 B SFD, 9 B of payload, and 1 B CRC. The simulations were repeated 10 times to obtain a 95 % confidence interval. We investigated the Packet Delivery Ratio (PDR) performance with and without the incorporation of mSync for the communications part in an optical wireless propagation scenario. We also investigated the throughput performance under different DPC intensities, the achievable bit rate for the possible incorporation of the VLCS system in industrial IoT applications, and some test-frequencies detection for the sensing part of the VLCS system, especially the impact of DPC on the strobing signal. The most relevant simulation parameters are listed in Table 6.1.

6.6.1 Visible Light Communications Performance

6.6.1.1 Single Detector

Figures 6.10a and 6.10b show the PDR performances with a single PD over increasing transmit power levels for normal and mSync operation modes, respectively. The horizontal dashed line marks 90 % PDR, with 100 % indicating that all the packets have been correctly detected and decoded. Also, the continuous line-plot demonstrates

Table 6.1 – Key parameters of the joint VLCS system.

Modulation	Differential BPSK
Bytes-per-Packet	12 B
Packet Sent	1000
Samples-per-Packet	96
Preamble + SFD + Payload + CRC	1 B + 1 B + 9 B + 1 B
Sampling Frequency	2 MHz
Interpolation Rate	3×
Noise Floor (14-bit DAC)	−84.3 dB or −54.3 dBm
Photo-Detector Aperture (D)	0.3 m
Emulated Low FPS Camera Cut-off	100 Hz
LED Array Panel	10 × 1

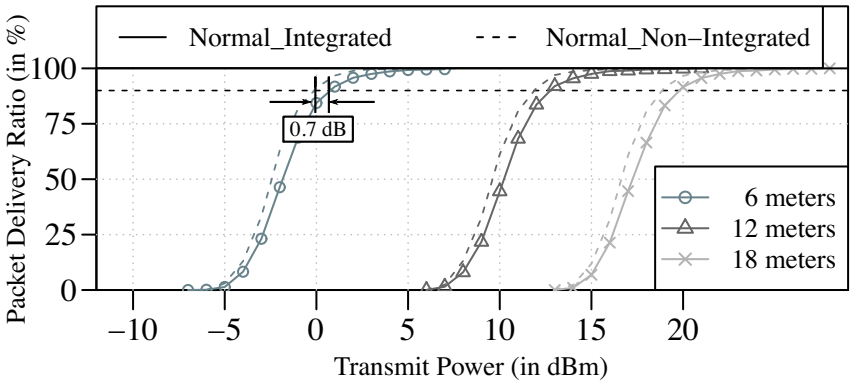

(a) Measured Packet Delivery Ratio (PDR) with a single Photo-Detector (PD) in normal mode.

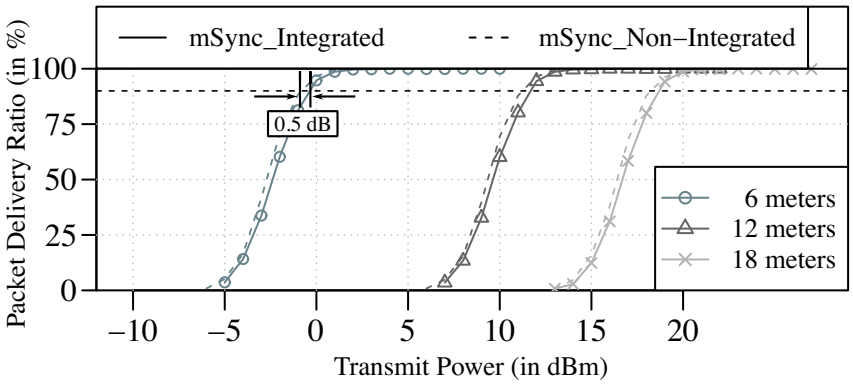

(b) Measured Packet Delivery Ratio (PDR) with a single Photo-Detector (PD) in mSync mode.

FIGURE 6.10 – Measured Packet Delivery Ratio (PDR) with a single Photo-Detector (PD) for different distances and increasing transmit power levels.

the PDR performance with the integrated VLCS system, i.e., combined sensing and communications. Whereas the dashed line non-integrated VLC only plots present the PDR performance without the sensing signal. Clearly, the addition of a sensing signal does have an impact on the PDR performance, which is dropped down by approx. 0.7 dB in the case of the integrated system with normal mode, and by approx. 0.4 dB in the case of the integrated system with mSync mode. This performance drop is certainly because of the DC blocker's high-pass behavior producing the resultant noise distortions σ^2_{dc} due to the strobing signal, as modeled in Section 6.4.1. Nevertheless, given the gains of the integrated system, this small performance degradation is negligible. Additionally, the PDR performance of the integrated system in mSync mode is roughly 1 dB better than normal mode, which agrees with the findings in [154]. Thus, mSync mode is not just improving the performance but also reducing the packet size, and hence the energy requirements from the transmitter.

6.6.1.2 Multiple Detector

Figures 6.11a and 6.11b present the PDR performances with a group of three PDs for normal and mSync operation modes, respectively. At the receiver, receive-diversity is applied to combine the signal received at each detector via the Equal Gain Combining (EGC) technique. As the detectors are right next to each other and absorb roughly similar light intensity [157], a simple micro-diversity approach with co-phasing of the received signal at each detector is used to accomplishes EGC diversity. Firstly, the multiple detectors are demonstrating roughly similar performance trends between normal and mSync modes as we have already seen with a single detector, i.e., a close to 1.1 dB degraded performance with normal mode. Here, the mSync with spatial diversity is still demonstrating better performance over normal mode, and these results are in line with our finding in [155].

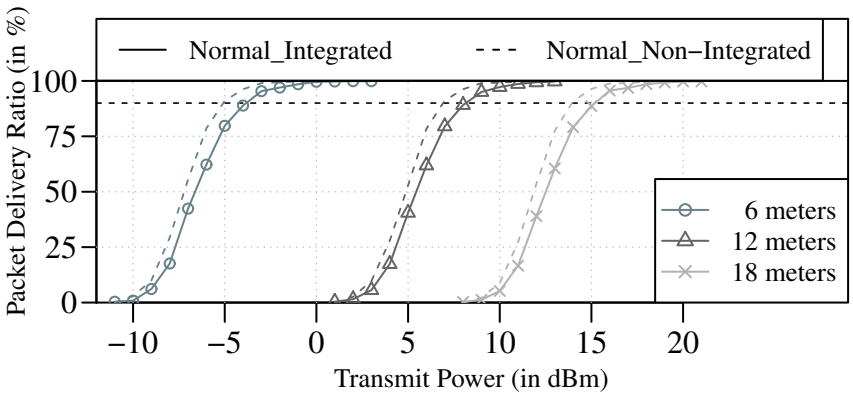

(a) Measured Packet Delivery Ratio (PDR) with three Photo-Detectors (PDs) in normal mode.

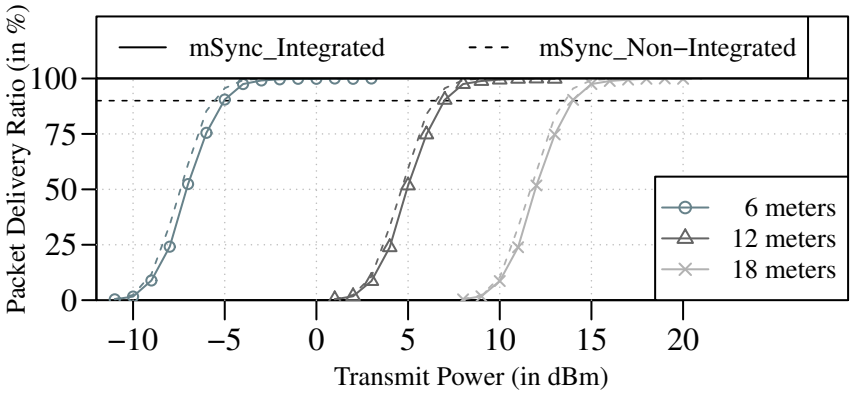

(b) Measured Packet Delivery Ratio (PDR) with three Photo-Detectors (PDs) in mSync mode.

FIGURE 6.11 – Measured Packet Delivery Ratio (PDR) with three Photo-Detectors (PDs) employing EGC diversity combining. The PDR is computed with increasing transmit power levels over multiple distances.

Secondly, the normal integrated, i.e., VLCS, system performance with three PDs is close to 1.3 dB more degraded than non-integrated (only VLC), which is a bit higher as compared to single-detector case. Finally, from the PDR comparison in Figures 6.10 and 6.11, a performance gain of close to 4.5 dB is measured with the three PDs over a single PD. A similar performance gain is also reported for three branch diversity in [133]. The deployment of multiple detectors can certainly improve the overall system's performance without too much additional cost and hardware under both modes, i.e., normal or mSync. Nevertheless, mSync is not just improving the performance here but also reducing the packet size by 8.3 %. Overall, even less power is required from the transmitter to obtain similar performance with three-detectors, especially in mSync operation mode.

6.6.1.3 Throughput Gain

Figure 6.12 presents the achievable throughput levels by exploiting different fix-percentages of the strobing signal's dark period for communication purposes. The Dark Period Communication (DPC) 100 % means that the data is transmitted for the complete strobing signal duration, whereas the DPC intensity 0 % indicates that the data is only transmitted during the *ON-Time* of the strobing signal. The resultant time-domain waveforms in both cases are presented in Figure 6.4. For a fair comparison, the same transmit power is used to measure these throughput-levels in VLCS and VLC systems. Clearly, the utilization of DPC improves magnitudes of the throughput capacity compared to the basic VLCS system, i.e., with 0 % DPC. Additionally, it can be noticed that for the same transmit power, the throughput performance of the VLCS system is comparatively lower than the simple VLC system. This is essentially because of the added noise and signal distortion due to the DC filtering of the strobing signal, as discussed in Section 6.4.1. Nevertheless, the gains

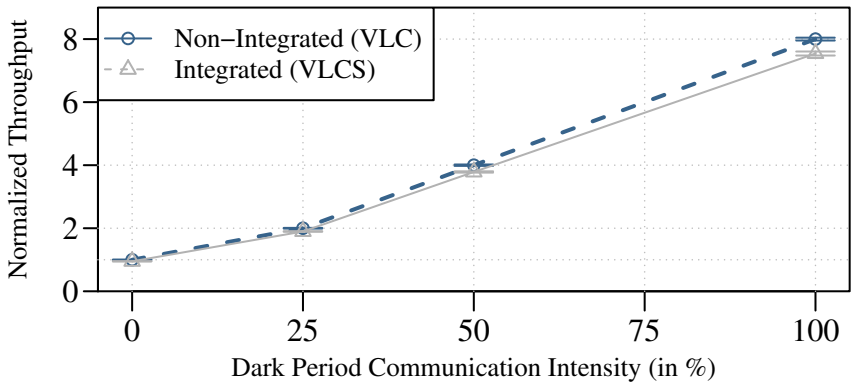

FIGURE 6.12 – Achievable throughput levels with different percentages of dark period utilized for communications in joint VLCS and simple VLC systems.

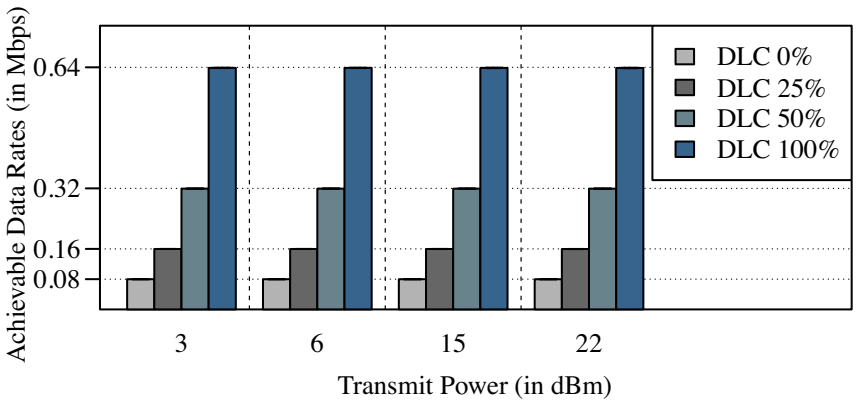

FIGURE 6.13 – The measured data rates with the VLCS system utilizing different percentages of the dark period for communications at various distances. The required transmit powers correspond to the distances in order to achieve optimal data rates.

with the VLCS system to perform both non-invasive sensing and communications certainly outweighs the small degradation in the performance.

6.6.1.4 Achievable Data Rates

Figure 6.13 shows the measured data rates with the proposed VLCS system at different distances. The maximum data rate achieved with the presented system is 640 kbit/s with 100 % DPC intensity. In the case of no DPC, i.e., 0 % DPC intensity, the maximum data rate recorded is 80 kbit/s. These measured data rates are strictly bounded by the used sampling frequency, which in these simulation experiments, is chosen as 2 MHz. These link rates can certainly be increased by adopting a higher sampling frequency and efficient modulation techniques. Additionally, in the figure, it can be noticed that these data rates are for up-to a simulated distance of 18 m with a transmit power of 22 dBm. These measured data rates and the communication distances certainly provide valuable performance insights, and they are especially very interesting if the combined VLCS system is to be considered in industrial IoT for smart automation and safety applications.

6.6.2 Visible Light Sensing Performance

To gain some insights on the impact of communication signal on the sensing pulse, we sampled some known low frequencies (10 Hz and 70 Hz) with the strobing signal of both VLCS system with 100 % DPC and simple VLS system in the emulated environment. As can be observed in Figure 6.14a, the frequency detection results are remarkably similar with both VLCS and VLS strobing signals. Such close frequency detection results are rather expected as we have already seen a quite small

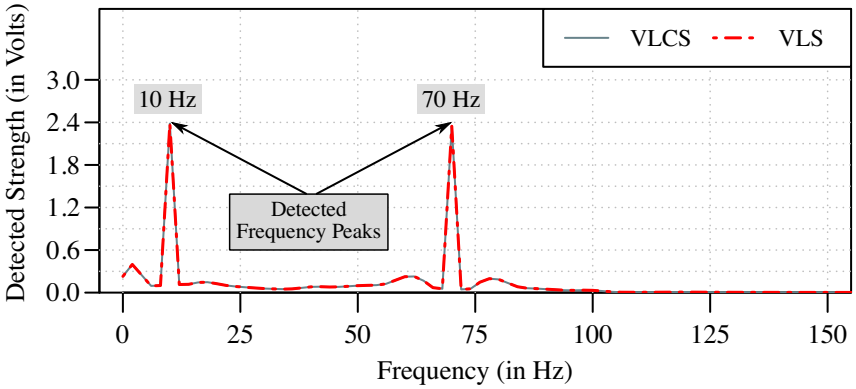

(a) Detected frequency, VLS vs. VLCS with 100 % DPC.

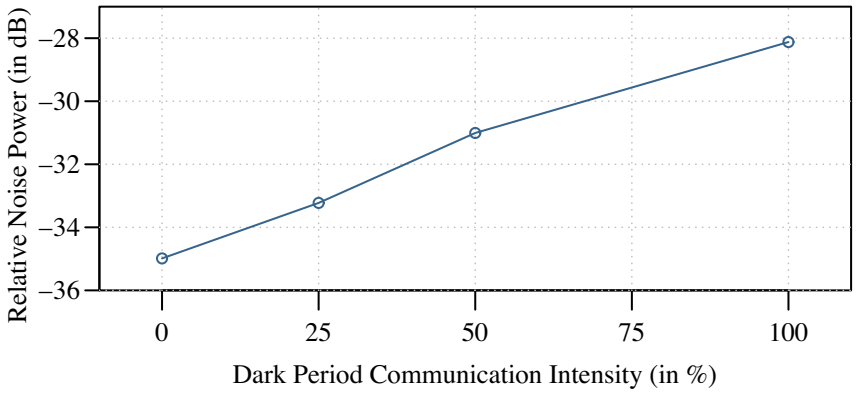

(b) Noise power with increasing intensity of DPC.

FIGURE 6.14 – The detected frequencies in VLS and VLCS emulated environments with 100 % DPC and the relative noise power with different DPC intensities.

error magnitude between the envelopes of two pulses in the earlier section (cf. Figure 3.18).

Additionally, it can be seen in Figure 6.14b that the noise level is raised by 7 dB as the DPC intensity is increased from 0 % to 100 %. This higher relative noise is anticipated at stronger DPC intensities due to the additional background noise factor $N_{\mathrm{DL}}(\omega)$, as discussed in Section 6.4.2. These results evidently indicated that DPC has a negative impact on the sensing performance; however, it has not introduced any considerable error while detecting the frequencies, and at the same time, DPC supported much higher throughput, which is certainly beneficial in industrial IoT applications, connecting everything for smart automation.

At this point, it is worth mentioning that once the vibrational frequency of a machine is approximated, it remains the same unless there is a fault. Thus, the same low FPS camera can be time-shared among multiple machines for sensing

the vibration and logging the data. In addition to that, the same cameras can also perform security tasks effectively as well, as illustrated in Figure 6.1.

6.7 Concluding Remarks

The smart monitoring of the structural health of machines, together with the industrial Internet of Things (IoT), is becoming a core component of futuristic smart automation of industries. However, novel communication technologies need to be investigated to overcome the limitations of the very crowded Radio Frequency (RF) spectrum. Indoor Visible Light Communication (VLC) has emerged as a viable technology with significant commercial potential. With the widespread Light Emitting Diode (LED) usage in the indoors, high-density wireless *downlinks* for a large number of IoT elements can potentially be realized, which can reduce the traffic on the RF spectrum and improve communication performance, especially in safety-critical and radio-hostile industrial environments. Besides the facilitation of visible light in wireless communications, it has also demonstrated non-invasive sensing capabilities to monitor an object's vibrations. VLC is considered a promising alternative.

In this chapter, for the first time, we introduced a complete Visible Light Communication and Sensing (VLCS) system for the application in smart industries. The proposed system combines an indoor VLC system for industrial-IoT applications, with an optical sensing approach monitoring the health of machines and other industrial installations. In particular, we used a strobing light-based frequency detection to determine the vibration frequency of a machine under observation; and added the VLC modulated signal on top of the sensing signal. The key challenge was to maintain a constant energy envelope of the light signal for the frequency detection. We have demonstrated here that the overall performance of our VLCS system is close to a VLC-only system, which now integrates the sensing mechanism in the same light spectrum even with Dark Period Communication (DPC). Using simulations, we showed that the Packet Delivery Ratio (PDR) performance of the proposed system only drops by 0.5 dB to 1 dB, when combined with the strobing signal, for a distance of 6 m to 18 m. We further reduced the VLC transmission power requirements by adopting the spatial diversity technique and mSync architecture. Our proposed VLCS system additionally demonstrated that the error between the envelopes of the sensing signals in integrated and non-integrated modes is below -50 dB, and the resultant error in the sensed frequencies is around -35 dB. The obtained results have shown that combining the sensing and communications signal only incurs a small drop in the performance. Such an integrated system can be deployed in remote locations such as high-temperature/pressure or radioactive areas, in fully automated industries with hostile radio environments, and for industrial-IoT applications.

Chapter 7

Conclusion

In the context of this PhD thesis, we focused on *low latency and bandwidth efficient wireless communications*. We first investigated the in-band Full-Duplex Relaying (FDR) approach to reduce the end-to-end delays of existing Half-Duplex Relaying (HDR) architecture and; to efficiently utilize the sub-6 GHz spectrum while offering better coverage. We presented the first IEEE 802.11 a/g/p standard-compliant FDR system in the GNU Radio framework and; evaluated its performance with real-time simulations and Software-Defined Radio (SDR)-based real-world experiments. The core of the presented system is the real-time Looped Self-Interference (LSI) cancellation module, which allows the simultaneous reception and forwarding of the information. As opposed to HDR, where multiple spatial and temporal resources are required, our standard-compliant FDR implementation requires a single time and frequency resource to relay the information, thus making the communications bandwidth-efficient with lower delays. Our experimental and simulative evaluation of FDR showed a considerable reduction in physical layer latency compared to HDR. From the results, we further realized the critical requirement of LSI suppression to the noise floor for optimal performance and that the presented system can benefit from more sophisticated RF isolation approaches for LSI suppression.

Further focusing on the scalability of low latency communications in Intelligent Transportation Systems (ITS) context with time-critical applications, we extended the applicability of the proposed FDR system, and for the first time, highlighted its potential in platooning application for both sub-6 GHz and 77 GHz mmWave channels. For the 77 GHz channel, we observed that the higher propagation losses and directivity of mmWaves offered better LSI isolation than sub-6 GHz, and they are not feasible for the currently practiced Direct Transmission (DT) approach. Additionally, the DT approach required significantly high transmission powers even in the sub-6 GHz band for reliable transmissions of beacons to all the platoon members compared to FDR, which eventually generates a higher interference domain for

neighboring vehicles. In a five-vehicle multi-hop platoon scenario, we showed that the FDR incorporation in platooning substantially lowered the end-to-end delays as compared to classical HDR in both sub-6 GHz and mmWave channels.

From these findings, the implications of FDR, such as in vehicular communication, are very promising and open up a wide spectrum of its novel utilization, especially in time-critical applications. However, the key requirement of LSI suppression is still a critical benchmark for optimal performance, and the presented system can certainly benefit from the better LSI suppression. Additionally, the FDR implementation proposed here is based on an open-source framework and can be extended for different Medium Access Control (MAC) layer implementations supporting Full-Duplex (FD) relaying within GNU Radio and can be coupled with Wireshark for analyzing the network protocol at a microscopic level. We believe that our system provides the basis for a much-needed toolchain for a complete evaluation of FD relaying from packet-level to physical layer.

As a follow up on low latency and bandwidth-efficient communications, this thesis also explored the higher frequencies adaptation for wireless communications; in particular, we investigated VLC with a huge unused spectrum for outdoor and indoor applications. For outdoor experimental research, we introduced a complete Vehicular-VLC (V-VLC) prototype that supports OFDM with a variety of Modulation and Coding Schemes (MCSs), and it is compliant with the IEEE 802.11 standard. We studied different receiver configurations in the outdoors to minimize the impact of ambient daylight on the Photo-Detector (PD) and demonstrated that the proposed system can prevent the strong sunlight effect. Our extensive outdoor measurements during the daytime; revealed the system's capacity to reliably communicate beyond a 75 m distance. Additionally, from the prototype's evaluation, we established that higher data rates are essentially bottlenecked by the headlight's low-pass behavior and can be improved with lighting modules having faster response times, or; we adapt spectral-efficient modulation such as Adaptive Modulation and Coding (AMC). We anticipate a broad range of further experiments in the field of cooperative automated driving, e.g. platooning application, which can be performed on this basis and; given the flexibility of the used software and hardware components, the framework can easily be extended for further studies.

Finally, given the widespread LED usage in the indoors, we followed up on the VLC technology and proposed an indoor Visible Light Communication and Sensing (VLCS) system. The presented VLCS system is primarily designed for smart and non-invasive monitoring of machines' structural health, together with the VLC for IoT solutions in the smart automation of industries. Since a steady envelope of the strobing pulse is a crucial requirement for sensing; therefore, we first analyzed the error in the envelopes of the strobing signal due to the added communication signal, which we determined to be negligibly small and essentially substantiated the

proof-of-concept. In our detailed findings, the overall communication performance with the combined VLCS system is close to a VLC-only system, a degradation of 0.5 dB to 1 dB is measured. We also employed the spatial diversity technique and mSync architecture to reduce the VLC transmission power requirements and improved over-the-air data rates by utilizing the dark period of the strobing signal for communications as well. Interestingly, the sensing capability of the VLCS system demonstrated strong resilience towards the added VLC signal with small incremental error for increasing Dark Period Communication (DPC) intensities. We believe that the proposed integrated system can be particularly beneficial in remote locations such as high-temperature/pressure or radioactive areas; in fully automated industries with radio-hostile environments; and for industrial-IoT applications, where a large number of VLC-based IoT elements can potentially be realized to relax the traffic load on the RF spectrum.

Putting everything together, the future of wireless communications cannot be bound to a single technology or a spectrum, especially when targeting ubiquitous connectivity. The work presented in this PhD thesis highlights the techniques and opportunities that can be considered for bandwidth-efficient and low latency communications. We believe that our work showed the potential of wireless communications in spectrums other than purely RF and the possibility of air-interfaces cooperation, which brings us closer to wireless ubiquity. Specifically, we believe that a collaboration of these technologies will eventually melt together and behave like a heterogeneous unit to provide high-speed connectivity and; offer an improved user experience with minimum access delays.

List of Abbreviations

3GPP	3rd Generation Partnership Project
ACO-OFDM	Asymmetrically Clipped Optical OFDM
ADC	Analog-to-Digital Converter
AF	Amplify and Forward
AMC	Adaptive Modulation and Coding
AWGN	Additive White Gaussian Noise
BER	Bit Error Ratio
C-V2X	Cellular V2X
CACC	Cooperative Adaptive Cruise Control
CF	Construct and Forward
CIR	Channel Impulse Response
COTS	Commercial Off-The-Shelf
CP	Cyclic Prefix
CPS	Cyber-Physical Systems
CRC	Cyclic Redundancy Check
CSI	Channel State Information
D2D	Device to Device
DBPSK	Differential Binary Phase-Shift Keying
DC	Direct Current
DCO	Direct Current-Biased Optical
DCO-OFDM	Direct Current-Biased Optical OFDM
DD	Direct Detection
DF	Decode and Forward
DPC	Dark Period Communication
DSRC	Dedicated Short Range Communication
DSSS	Direct-Sequence Spread Spectrum
DT	Direct Transmission
DynB	Dynamic Beaconing
EGC	Equal Gain Combining
FD	Full-Duplex

FDD	Frequency Division Duplex
FDR	Full-Duplex Relaying
FFT	Fast Fourier Transform
FoV	Field of View
FPGA	Field-Programmable Gate Arrays
FPS	Frames Per Second
GPP	General Purpose Processor
GRC	GNU Radio Companion
HD	Half-Duplex
HDR	Half-Duplex Relaying
HetNet	Heterogeneous Network
HPBW	Half Power Beam-Width
IFFT	Inverse Fast Fourier Transform
IM	Intensity Modulation
IoT	Internet of Things
ITS	Intelligent Transportation System
IVC	Inter Vehicular Communication
LDV	Laser Doppler Vibrometer
LED	Light Emitting Diode
LMS	Least Mean Square
LoS	Line-of-Sight
LS	Least Square
LSI	Looped Self-Interference
LTE	Long Term Evolution
LTS	Long Training Sequence
MAC	Medium Access Control
MCS	Modulation and Coding Scheme
MIMO	Multiple-Input Multiple-Output
MPC	Multi Path Component
NAH	Near-field Acoustic Holography
NLoS	Nonline-of-Sight
OFDM	Orthogonal Frequency Division Multiplexing
OOK	On-Off Keying
PAPR	Peak-to-Average Power Ratio
PD	Photo-Detector
PDP	Power Delay Profile
PDR	Packet Delivery Ratio
PDU	Protocol Data Unit
PHY	Physical Layer
PLL	Physical Layer Latency

PPM	Pulse Position Modulation
RADCOM	RADar based COMmunication
RC	Repetition Coding
RF	Radio Frequency
RMa	rural macrocell
RSS	Received Signal Strength
SDR	Software-Defined Radio
SFD	Start of Frame Delimiter
SI	Self-Interference
SM	Spatial Multiplexing
SNR	Signal-to-Noise Ratio
SoI	Signal-of-Interest
SoP	Start-of-Packet
STS	Short Training Sequence
TCA	Transconductance Amplifier
TCSL	time cluster spatial lobe
TDD	Time Division Duplexing
TDMA	Time Division Multiple Access
THD	Total Harmonic Distortion
TIA	Transimpedance Amplifier
TPC	Transmit Power Control
UMa	urban macrocell
UMi	urban microcell
USRP	Universal Software Radio Peripheral
V-VLC	Vehicular-VLC
V2I	Vehicle-to-Infrastructure
V2V	Vehicle-to-Vehicle
V2X	Vehicle-to-anything
VANET	Vehicular Ad Hoc Network
VLC	Visible Light Communication
VLCS	Visible Light Communication and Sensing
VLS	Visible Light Sensing
VPPM	Variable Pulse Position Modulation
WAVE	Wireless Access in Vehicular Environments
WLAN	Wireless Local Area Network

List of Figures

List of Tables

Bibliography

[1] Cisco annual internet report (2018–2023) white paper, https://www.cisco.com/c/en/us/solutions/collateral/executive-perspectives/annual-internet-report/white-paper-c11-741490.html, [online] Available, Mar. 2020.

[2] Ericsson mobility Report on mobile data traffic outlook, https://www.ericsson.com/en/mobility-report/reports/june-2020/mobile-data-traffic-outlook, [online] Available.

[3] M. Dohler, R. W. Heath, A. Lozano, C. B. Papadias, and R. A. Valenzuela, "Is the PHY layer dead?" *IEEE Communications Magazine*, vol. 49, no. 4, pp. 159–165, 2011.

[4] R. Prasad and S. Dixit, Wireless World in 2050 and Beyond: A Window Into the Future! Springer, 2016.

[5] "Further advancements for E-UTRA physical layer aspects," 3rd Generation Partnership Project, Sophia Antipolis, France, TR 36.814 V9.0.0 (2010-03), Mar. 2010.

[6] "Local and metropolitan area networks," IEEE, Standard P802.16j-06/026r4, May 2007.

[7] Z. Zhang, K. Long, A. V. Vasilakos, and L. Hanzo, "Full-duplex wireless communications: Challenges, solutions, and future research directions," *Proceedings of the IEEE*, vol. 104, no. 7, pp. 1369–1409, 2016.

[8] D. Bharadia, E. McMilin, and S. Katti, "Full Duplex Radios," *ACM SIGCOMM Computer Communication Review (CCR)*, vol. 43, no. 4, pp. 375–386, Oct. 2013.

[9] E. Ahmed and A. M. Eltawil, "All-digital self-interference cancellation technique for full-duplex systems," *IEEE Transactions on Wireless Communications (TWC)*, vol. 14, no. 7, pp. 3519–3532, Jul. 2015.

[10] M. S. Amjad, H. Nawaz, K. Ozsoy, O. Gurbuz, and I. Tekin, "A Low-Complexity Full-Duplex Radio Implementation With a Single Antenna," *IEEE Transactions on Vehicular Technology (TVT)*, vol. 67, no. 3, pp. 2206–2218, Mar. 2018.

[11] J. Zhou, N. Reiskarimian, J. Diakonikolas, T. Dinc, T. Chen, G. Zussman, and H. Krishnaswamy, "Integrated Full Duplex Radios," *IEEE Communications Magazine (COMMAG)*, vol. 55, no. 4, pp. 142–151, 2017.

[12] R. Doost-Mohammady, N. Rahman, N. M Yousof, and K. R. Chowdhury, "Performance analysis of CSMA/CA based medium access in full duplex wireless communications," *IEEE Transactions on Mobile Computing (TMC)*, pp. 1457–1470, 2015.

[13] M. Amjad, F. Akhtar, M. R. Husain, M. Reisslein, and T. Umer, "Full-Duplex Communication in Cognitive Radio Networks: A Survey," *IEEE Communications Surveys & Tutorials*, pp. 2158–2191, 2017.

[14] F. Dressler, F. Klingler, M. Segata, and R. Lo Cigno, "Cooperative Driving and the Tactile Internet," *Proceedings of the IEEE*, vol. 107, no. 2, pp. 436–446, Feb. 2019.

[15] M. S. Amjad, T. Hardes, M. Schettler, C. Sommer, and F. Dressler, "Using Full Duplex Relaying to Reduce Physical Layer Latency in Platooning," in *11th IEEE Vehicular Networking Conference (VNC 2019)*, Los Angeles, CA: IEEE, Dec. 2019, pp. 236–239.

[16] C. Campolo, A. Molinaro, A. O. Berthet, and A. Vinel, "Full-duplex radios for vehicular communications," *IEEE Communications Magazine*, pp. 182–189, 2017.

[17] L. E. M. Matheus, A. B. Vieira, L. F. M. Vieira, M. A. M. Vieira, and O. Gnawali, "Visible Light Communication: Concepts, Applications and Challenges," *IEEE Communications Surveys & Tutorials*, vol. 21, no. 4, pp. 3204–3237, 2019.

[18] R. Zhang, "Localisation, communication and networking with VLC: Challenges and opportunities," *arXiv preprint arXiv:1709.01899*, 2017.

[19] A. Memedi and F. Dressler, "Vehicular Visible Light Communications: A Survey," *IEEE Communications Surveys & Tutorials*, 2020, to appear.

[20] I. S. Association et al., "IEEE standard for local and metropolitan area networks-Part 15.7: short-range wireless optical communication using visible light," *IEEE: Piscataway, NZ, USA*, pp. 1–309, 2011.

[21] D. C. O'brien, L. Zeng, H. Le-Minh, G. Faulkner, J. W. Walewski, and S. Randel, "Visible light communications: Challenges and possibilities," in *2008 IEEE 19th International Symposium on Personal, Indoor and Mobile Radio Communications*, IEEE, 2008, pp. 1–5.

[22] H. Haas, L. Yin, Y. Wang, and C. Chen, "What is lifi?" *Journal of lightwave technology*, vol. 34, no. 6, pp. 1533–1544, 2015.

[23] A.-M. Căilean and M. Dimian, "Current challenges for visible light communications usage in vehicle applications: A survey," *IEEE Communications Surveys & Tutorials*, vol. 19, no. 4, pp. 2681–2703, 2017.

[24] K. Kadam and M. R. Dhage, "Visible light communication for IoT," in *iCATccT 2016*, Bengaluru, India, Jul. 2016, pp. 275–278.

[25] H. Yang, W.-D. Zhong, C. Chen, A. Alphones, and P. Du, "QoS-Driven Optimized Design-Based Integrated Visible Light Communication and Positioning for Indoor IoT Networks," *IEEE Internet of Things Journal*, vol. 7, no. 1, pp. 269–283, 2019.

[26] D. Karunatilaka, F. Zafar, V. Kalavally, and R. Parthiban, "LED Based Indoor Visible Light Communications: State of the Art," *IEEE Communication Surveys & Tutorials*, vol. 17, no. 3, pp. 1649–1678, Mar. 2015.

[27] D. Roy, A. Ghose, T. Chakravarty, S. Mukherjee, A. Pal, and A. Misra, "Analysing Multi-Point Multi-Frequency Machine Vibrations using Optical Sampling," in *IoPARTS 2018*, Munich, Germany, Jun. 2018, pp. 55–59.

[28] D. Roy, S. Mukherjee, B. Bhowmik, A. Sinharay, R. Dasgupta, and A. Pal, "An autonomous, non-invesive vibration measurement system using stroboscope," in *ICST 2016*, Chinandega, Nicaragua, Nov. 2016, pp. 1–6.

[29] M. S. Amjad and F. Dressler, "Experimental Insights on Software-based Real-Time SI Cancellation for In-Band Full Duplex DF Relays," in *IEEE International Conference on Communications (ICC 2019)*, Shanghai, China: IEEE, May 2019.

[30] ——, "Software-based Real-time Full-duplex Relaying: An Experimental Study," *IEEE Transactions on Green Communications and Networking (TGCN)*, vol. 4, no. 3, pp. 647–656, Sep. 2020.

[31] ——, "Performance Insights on IEEE 802.11a/g Compliant Software-based In-Band Full Duplex Relay Systems," in *IEEE Wireless Communications and Networking Conference (WCNC 2019)*, Marrakesh, Morocco: IEEE, Apr. 2019.

[32] ——, "Software-based In-Band Full Duplex Relays for IEEE 802.11a/g/p: An Experimental Study," in *IEEE Wireless Communications and Networking Conference (WCNC 2021)*, Nanjing, China: IEEE, Mar. 2021.

[33] M. S. Amjad, T. Hardes, M. Schettler, C. Sommer, and F. Dressler, "Using Full Duplex Relaying to Reduce Physical Layer Latency in Platooning," in *11th IEEE Vehicular Networking Conference (VNC 2019)*, Los Angeles, CA: IEEE, Dec. 2019, pp. 236–239.

[34] M. S. Amjad, M. Schettler, S. Dimce, and F. Dressler, "Inband Full-Duplex Relaying for RADCOM-based Cooperative Driving," in *12th IEEE Vehicular Networking Conference (VNC 2020)*, Virtual Conference: IEEE, Dec. 2020.

[35] M. S. Amjad, C. Tebruegge, A. Memedi, S. Kruse, C. Kress, C. Scheytt, and F. Dressler, "An IEEE 802.11 Compliant SDR-based System for Vehicular Visible Light Communications," in *IEEE International Conference on Communications (ICC 2019)*, Shanghai, China: IEEE, May 2019.

[36] ——, "Towards an IEEE 802.11 Compliant System for Outdoor Vehicular Visible Light Communications," *IEEE Transactions on Vehicular Technology (TVT)*, 2021, to appear. DOI: 10.1109/TVT.2021.3075301.

[37] M. Nabeel, M. S. Amjad, and F. Dressler, "Preamble-Less Diversity Combining: Improved Energy-Efficiency in Sensor Networks," in *IEEE Global Communications Conference (GLOBECOM 2018)*, Abu Dhabi, United Arab Emirates: IEEE, Dec. 2018.

[38] M. S. Amjad and F. Dressler, "Integrated Communications and Non-Invasive Vibrations Sensing using Strobing Light," in *IEEE International Conference on Communications (ICC 2020)*, Virtual Conference: IEEE, Jun. 2020.

[39] ——, "Using Visible Light for Joint Communications and Vibration Sensing in Industrial IoT Applications," in *IEEE International Conference on Communications (ICC 2021)*, to appear, Montreal Canada: IEEE, 2021.

[40] M. S. Amjad, G. S. Pannu, A. Memedi, M. Nabeel, J. Blobel, F. Missbrenner, and F. Dressler, "A Flexible Real-Time Software-based Multi-Band Channel Sounder," in *31st IEEE Annual International Symposium on Personal, Indoor and Mobile Radio Communications (PIMRC 2020)*, Virtual Conference: IEEE, Aug. 2020.

[41] M. S. Amjad, H. Nawaz, K. Ozsoy, O. Gurbuz, and I. Tekin, "A Low-Complexity Full-Duplex Radio Implementation With a Single Antenna," *IEEE Transactions on Vehicular Technology (TVT)*, vol. 67, no. 3, pp. 2206–2218, Mar. 2018.

[42] S. Kruse, C. Kress, A. Memedi, C. Tebruegge, M. S. Amjad, C. Scheytt, and F. Dressler, "Design of an Automotive Visible Light Communications Link using an Off-The-Shelf LED Headlight," in *16th GMM/ITG-Symposium ANALOG 2018*, Munich, Germany: VDE, Sep. 2018.

[43] J. Koepe, C. Kaltschmidt, M. Illian, R. Puknat, P. Kneuper, S. Wittemeier, A. Memedi, C. Tebruegge, M. S. Amjad, S. Kruse, et al., "First Performance Insights on Our Novel OFDM-based Vehicular VLC Prototype," in *10th IEEE Vehicular Networking Conference (VNC 2018), Poster Session*, Taipei, Taiwan: IEEE, Dec. 2018.

[44] A. G. Bell, "On selenium and the photophone," *Electrician*, vol. 5, pp. 214–220, 1880.

[45] A. F. Molisch, Wireless communications. John Wiley & Sons, 2012, vol. 34.

[46] M. S. Amjad, "Digital self-interference cancellation in full-duplex wireless systems," Master's Thesis, Faculty of Engineering and Natural Sciences, Aug. 2016.

[47] M. Jain, J. I. Choi, T. Kim, D. Bharadia, S. Seth, K. Srinivasan, P. Levis, S. Katti, and P. Sinha, "Practical, Real-time, Full Duplex Wireless," in *17th ACM International Conference on Mobile Computing and Networking (MobiCom 2011)*, Las Vegas, NV: ACM, Sep. 2011, pp. 301–312.

[48] M. Duarte and A. Sabharwal, "Full-duplex wireless communications using off-the-shelf radios: Feasibility and first results," in *2010 Conference Record of the Forty Fourth Asilomar Conference on Signals, Systems and Computers*, IEEE, 2010, pp. 1558–1562.

[49] E. Everett, A. Sahai, and A. Sabharwal, "Passive self-interference suppression for full-duplex infrastructure nodes," *IEEE Transactions on Wireless Communications (TWC)*, vol. 13, no. 2, pp. 680–694, 2014.

[50] B. Radunovic, D. Gunawardena, P. Key, A. Proutiere, N. Singh, V. Balan, and G. Dejean, "Rethinking indoor wireless mesh design: Low power, low frequency, full-duplex," in *Wireless Mesh Networks (WIMESH 2010), 2010 Fifth IEEE Workshop on*, IEEE, 2010, pp. 1–6.

[51] E. Ahmed, A. M. Eltawil, and A. Sabharwal, "Self-interference cancellation with nonlinear distortion suppression for full-duplex systems," in *2013 Asilomar Conference on Signals, Systems and Computers*, IEEE, 2013, pp. 1199–1203.

[52] J. I. Choi, M. Jain, K. Srinivasan, P. Levis, and S. Katti, "Achieving Single Channel, Full Duplex Wireless Communication," in *16th ACM International Conference on Mobile Computing and Networking (MobiCom 2010)*, Chicago, IL: ACM, Sep. 2010, pp. 1–12.

[53] E. Ahmed, A. Eltawil, and A. Sabharwal, "Simultaneous transmit and sense for cognitive radios using full-duplex: A first study," in *Proceedings of the 2012 IEEE International Symposium on Antennas and Propagation*, IEEE, 2012, pp. 1–2.

[54] M. Duarte, C. Dick, and A. Sabharwal, "Experiment-driven characterization of full-duplex wireless systems," *IEEE Transactions on Wireless Communications*, vol. 11, no. 12, pp. 4296–4307, 2012.

[55] E. Ahmed, A. M. Eltawil, and A. Sabharwal, "Self-interference cancellation with phase noise induced ICI suppression for full-duplex systems," in *2013 IEEE Global Communications Conference (GLOBECOM)*, IEEE, 2013, pp. 3384–3388.

[56] A. Sahai, G. Patel, and A. Sabharwal, "Pushing the limits of full-duplex: Design and real-time implementation," *arXiv preprint arXiv:1107.0607*, 2011.

[57] A. Goldsmith, Wireless communications. Cambridge university press, 2005.

[58] Z. Wang, X. Ma, and G. B. Giannakis, "OFDM or single-carrier block transmissions?" *IEEE transactions on communications*, vol. 52, no. 3, pp. 380–394, 2004.

[59] J. W. Cooley and J. W. Tukey, "An algorithm for the machine calculation of complex Fourier series," *Mathematics of computation*, vol. 19, no. 90, pp. 297–301, 1965.

[60] "IEEE 802.11a/g, Vocal Technologies, voice and data communications," 2012.

[61] W.-Y. Lin, M.-W. Li, K.-c. Lan, and C.-H. Hsu, "A Comparison of 802.11 a and 802.11 p for V-to-I Communication: A Measurement Study," in *International Conference on Heterogeneous Networking for Quality, Reliability, Security and Robustness*, Springer, 2010, pp. 559–570.

[62] t. W. W. G. o. t. I. C. Architecture, "IEEE P1609.0/D0.7 Draft Standard," Jan. 2009.

[63] G. David and P. Kavita, "An overview of LED applications for general illumination," in *SPIE*, vol. 3781, 2003, pp. 15–26.

[64] S.-H. Yu, O. Shih, H.-M. Tsai, N. Wisitpongphan, and R. Roberts, "Smart automotive lighting for vehicle safety," *IEEE Communications Magazine (COMMAG)*, vol. 51, no. 12, pp. 50–59, Dec. 2013.

[65] S. Dimitrov and H. Haas, Principles of LED Light Communications: Towards Networked Li-Fi. Cambridge University Press, 2015.

[66] M. Zhang and Z. Zhang, "An optimum DC-biasing for DCO-OFDM system," *IEEE Communications Letters*, vol. 18, no. 8, pp. 1351–1354, 2014.

[67] J. Armstrong and B. J. Schmidt, "Comparison of asymmetrically clipped optical OFDM and DC-biased optical OFDM in AWGN," *IEEE Communications Letters*, vol. 12, no. 5, pp. 343–345, 2008.

[68] S. D. Dissanayake and J. Armstrong, "Comparison of aco-ofdm, dco-ofdm and ado-ofdm in im/dd systems," *Journal of lightwave technology*, vol. 31, no. 7, pp. 1063–1072, 2013.

[69] W. Xu, M. Wu, H. Zhang, X. You, and C. Zhao, "ACO-OFDM-specified recoverable upper clipping with efficient detection for optical wireless communications," *IEEE Photonics Journal*, vol. 6, no. 5, pp. 1–17, 2014.

[70] Y. Xiao, Y.-J. Zhu, Y.-Y. Zhang, and Z.-G. Sun, "Linear optimal signal designs for multi-color MISO-VLC systems adapted to CCT requirement," *IEEE Access*, vol. 6, pp. 75 519–75 530, 2018.

[71] D.-R. Kim, S.-H. Yang, H.-S. Kim, Y.-H. Son, and S.-K. Han, "Outdoor visible light communication for inter-vehicle communication using controller area network," in *2012 Fourth International Conference on Communications and Electronics (ICCE)*, IEEE, 2012, pp. 31–34.

[72] K. E. Kolodziej, B. T. Perry, and J. S. Herd, "In-band full-duplex technology: Techniques and systems survey," *IEEE Transactions on Microwave Theory and Techniques*, vol. 67, no. 7, pp. 3025–3041, 2019.

[73] J. Laneman, D. Tse, and G. Wornell, "Cooperative Diversity in Wireless Networks: Efficient Protocols and Outage Behavior," *IEEE Transactions on Information Theory*, vol. 50, no. 12, pp. 3062–3080, Dec. 2004.

[74] B. Rankov and A. Wittneben, "Spectral efficient protocols for half-duplex fading relay channels," *IEEE Journal on Selected Areas in Communications (JSAC)*, vol. 25, no. 2, pp. 379–389, Feb. 2007.

[75] J. Jiao, X. Jia, M. Zhou, M. Xie, and Q. Cao, "Full-duplex massive MIMO AF relaying system with low-resolution ADCs under ZFT/ZFR scheme," in *IEEE IAEAC 2017*, Chongqing, China: IEEE, Mar. 2017, pp. 2024–2028.

[76] Q. Li, S. Feng, X. Ge, G. Mao, and L. Hanzo, "On the Performance of Full-Duplex Multi-Relay Channels With DF Relays," *IEEE Trans. on Vehicular Technology*, vol. 66, no. 10, pp. 9550–9554, Oct. 2017.

[77] L. Elsaid, M. Ranjbar, N. Raymondi, D. Nguyen, N. Tran, and A. Mahamadi, "Full-Duplex Decode-and-Forward Relaying: Secrecy Rates and Optimal Power Allocation," in *85th IEEE Vehicular Technology Conference (VTC 2017-Spring)*, Sydney, Australia: IEEE, Jun. 2017.

[78] F. H. Gregorio, G. J. Gonzalez, J. Cousseau, T. Riihonen, and R. Wichman, "RF Front-End Implementation Challenges of In-band Full-Duplex Relay Transceivers," in *European Wireless Conference (EW 2016)*, Oulu, Finland: IEEE, May 2016.

[79] T.-C. Chen, Y.-C. Chen, M.-K. Chang, and G.-C. Yang, "The Impact of Loopback Channel Estimation Error on Performance of Full-Duplex Two-Way AF Relaying Communication Systems," in *85th IEEE Vehicular Technology Conference (VTC 2017-Spring)*, Sydney, Australia: IEEE, Jun. 2017.

[80] Y. Liu, Y. Yue, X.-G. Xia, C. Kang, and H. Zhang, "SC-FDE based full-duplex relay communication robust to residual loop interference," *IEEE Wireless Communications Letters*, pp. 538–541, 2017.

[81] E. Antonio-Rodriguez and R. López-Valcarce, "Cancelling self-interference in full-duplex relays without angle-of-arrival information," in *IEEE International Conference on Acoustics, Speech and Signal Processing (ICASSP 2013)*, Vancouver, Canada: IEEE, May 2013, pp. 4731–4735.

[82] T. Riihonen, S. Werner, and R. Wichman, "Hybrid full-duplex/half-duplex relaying with transmit power adaptation," *IEEE Transactions on Wireless Communications (TWC)*, vol. 10, no. 9, pp. 3074–3085, 2011.

[83] D. Bharadia and S. Katti, "Fastforward: Fast and constructive full duplex relays," *ACM SIGCOMM Computer Communication Review (CCR)*, vol. 44, no. 4, pp. 199–210, 2015.

[84] D. Korpi, M. Heino, C. Icheln, K. Haneda, and M. Valkama, "Compact inband full-duplex relays with beyond 100 dB self-interference suppression: Enabling techniques and field measurements," *IEEE Transactions on Antennas and Propagation*, vol. 65, no. 2, pp. 960–965, 2016.

[85] S. Mohammad, Z. Ammar, and Hussein, Alnuweiri amd Mohamed-Slim, Alouini, "Maximizing Expected Achievable Rates for Block-Fading Buffer-Aided Relay Channels," *IEEE Transactions on Wireless Communications*, vol. 15, no. 9, pp. 5919–5931, Sep. 2016.

[86] Q. Deli, "Effective Capacity of Buffer-Aided Full-Duplex Relay Systems With Selection Relaying," *IEEE Transactions on Communications*, vol. 64, no. 1, pp. 117–129, Jan. 2016.

[87] M. R. Mohsen and Z. Nikola, "Buffer-aided relaying for the two-hop full-duplex relay channel with self-interference," *IEEE Transactions on Wireless Communications*, vol. 17, no. 1, pp. 477–491, Jan. 2018.

[88] M. S. Amjad and F. Dressler, "Performance Insights on IEEE 802.11a/g Compliant Software-based In-Band Full Duplex Relay Systems," in *IEEE WCNC 2019*, Marrakesh, Morocco: IEEE, Apr. 2019.

[89] B. Bloessl, M. Segata, C. Sommer, and F. Dressler, "An IEEE 802.11a/g/p OFDM Receiver for GNU Radio," in *ACM SIGCOMM 2013, SRIF Workshop*, Hong Kong, China: ACM, Aug. 2013, pp. 9–16.

[90] ——, "Performance Assessment of IEEE 802.11p with an Open Source SDR-based Prototype," *IEEE Trans. on Mobile Computing*, vol. 17, no. 5, pp. 1162–1175, May 2018.

[91] H. Nawaz and I. Tekin, "Three dual polarized 2.4GHz microstrip patch antennas for active antenna and in-band full duplex applications," in *16th Mediterranean Microwave Symposium (MMS 2016)*, Abu Dhabi, United Arab Emirates: IEEE, Nov. 2016.

[92] R. Akeela and B. Dezfouli, "Software-defined Radios: Architecture, state-of-the-art, and challenges," *Elsevier Computer Communications*, pp. 106–125, 2018.

[93] N. Hemsoth, "Latest FPGAs Show Big Gains in Floating Point Performance," *HPCWire*, Apr. 2012.

[94] C. Bergenhem, H. Pettersson, E. Coelingh, C. Englund, S. Shladover, and S. Tsugawa, "Overview of Platooning Systems," in *ITS 2012*, Vienna, Austria: Transportation Research Board, Oct. 2012.

[95] M. Segata, B. Bloessl, S. Joerer, C. Sommer, M. Gerla, R. Lo Cigno, and F. Dressler, "Towards Communication Strategies for Platooning: Simulative and Experimental Evaluation," *IEEE Trans. on Vehicular Technology*, vol. 64, no. 12, pp. 5411–5423, Dec. 2015.

[96] J. Ploeg, B. Scheepers, E. van Nunen, N. van de Wouw, and H. Nijmeijer, "Design and Experimental Evaluation of Cooperative Adaptive Cruise Control," in *IEEE ITSC 2011*, Washington, D.C.: IEEE, Oct. 2011, pp. 260–265.

[97] L. Han and K. Wu, "Multifunctional Transceiver for Future Intelligent Transportation Systems," *IEEE Transactions on Microwave Theory and Techniques*, vol. 59, no. 7, pp. 1879–1892, 2011.

[98] S. Sun, G. R. MacCartney, and T. S. Rappaport, "A novel millimeter-wave channel simulator and applications for 5G wireless communications," in *IEEE International Conference on Communications (ICC 2017)*, Paris, France: IEEE, May 2017.

[99] P. Fernandes and U. Nunes, "Platooning With IVC-Enabled Autonomous Vehicles: Strategies to Mitigate Communication Delays, Improve Safety and Traffic Flow," *IEEE Trans. on Intelligent Transportation Systems*, vol. 13, no. 1, pp. 91–106, Mar. 2012.

[100] S. Santini, A. Salvi, A. S. Valente, A. Pescapè, M. Segata, and R. Lo Cigno, "A Consensus-based Approach for Platooning with Inter-Vehicular Communications and its Validation in Realistic Scenarios," *IEEE Transactions on Vehicular Technology (TVT)*, vol. 66, no. 3, pp. 1985–1999, Mar. 2017.

[101] C. Campolo, A. Molinaro, G. Araniti, and A. Berthet, "Better Platooning Control Toward Autonomous Driving: An LTE Device-to-Device Communications Strategy That Meets Ultralow Latency Requirements," *IEEE Vehicular Technology Magazine (VTMag)*, vol. 12, no. 1, pp. 30–38, Mar. 2017.

[102] C. Campolo, A. Molinaro, and A. O. Berthet, "Full-duplex communications to improve platooning control in multi-channel VANETs," in *2017 IEEE International Conference on Communications Workshops (ICC Workshops)*, Paris, France: IEEE, May 2017.

[103] S. Dwivedi, A. N. Barreto, P. Sen, and G. P. Fettweis, "Target Detection in Joint Frequency Modulated Continuous Wave (FMCW) Radar-Communication System," in *16th IEEE International Symposium on Wireless Communication Systems (ISWCS 2019)*, Oulu, Finland, Oct. 2019, pp. 277–282.

[104] C. D. Ozkaptan, E. Ekici, and O. Altintas, "Enabling Communication via Automotive Radars: An Adaptive Joint Waveform Design Approach," in *39th IEEE International Conference on Computer Communications (INFOCOM 2020)*, Virtual Conference: IEEE, Jul. 2020.

[105] B. Lee, J.-B. Lim, C. Lim, B. Kim, and J.-y. Seol, "Reflected self-interference channel measurement for mmWave beamformed full-duplex system," in *IEEE Global Communications Conference (GLOBECOM 2015), Workshops*, San Diego, CA, Dec. 2015, pp. 1–6.

[106] R. López-Valcarce and N. González-Prelcic, "Beamformer design for Full-Duplex Amplify-and-Forward millimeter wave relays," in *16th IEEE International Symposium on Wireless Communication Systems (ISWCS 2019)*, Oulu, Finland, Oct. 2019, pp. 86–90.

[107] B. Ma, H. Shah-Mansouri, and V. W. Wong, "Full-duplex relaying for D2D communication in millimeter wave-based 5G networks," *IEEE Transactions on Wireless Communications (TWC)*, vol. 17, no. 7, pp. 4417–4431, 2018.

[108] M. S. Amjad and F. Dressler, "Software-based Real-time Full-duplex Relaying: An Experimental Study," *IEEE Transactions on Green Communications and Networking (TGCN)*, 2020, online: 10.1109/TGCN.2020.2966140.

[109] S. Ju, O. Kanhere, Y. Xing, and T. S. Rappaport, "A millimeter-wave channel simulator NYUSIM with spatial consistency and human blockage," in *IEEE Global Communications Conference (GLOBECOM 2019)*, Waikoloa, HI, Dec. 2019, pp. 1–6.

[110] A. Memedi, H.-M. Tsai, and F. Dressler, "Impact of Realistic Light Radiation Pattern on Vehicular Visible Light Communication," in *IEEE GLOBECOM 2017*, Singapore, Singapore: IEEE, Dec. 2017.

[111] J. Gancarz, H. Elgala, and T. D. C. Little, "Impact of lighting requirements on VLC systems," *IEEE Communications Magazine*, vol. 51, no. 12, pp. 34–41, Dec. 2013.

[112] P. H. Pathak, X. Feng, P. Hu, and P. Mohapatra, "Visible Light Communication, Networking, and Sensing: A Survey, Potential and Challenges," *IEEE Communications Surveys & Tutorials*, vol. 17, no. 4, pp. 2047–2077, Feb. 2015.

[113] A.-M. Cailean and M. Dimian, "Current Challenges for Visible Light Communications Usage in Vehicle Applications: A Survey," *IEEE Communications Surveys & Tutorials*, vol. 4, no. 19, pp. 2681–2703, 2017.

[114] C. B. Liu, B. Sadeghi, and E. W. Knightly, "Enabling Vehicular Visible Light Communication (V2LC) Networks," in *8th ACM International Workshop on Vehicular Internetworking (VANET 2011)*, Las Vegas, NV: ACM, Sep. 2011, pp. 41–50.

[115] T. Yamazato, I. Takai, H. Okada, T. Fujii, T. Yendo, S. Arai, M. Andoh, T. Harada, K. Yasutomi, K. Kagawa, et al., "Image-Sensor-Based Visible Light Communication for Automotive Applications," *IEEE Communications Magazine (COMMAG)*, vol. 52, no. 7, pp. 88–97, Jul. 2014.

[116] M. S. Amjad, C. Tebruegge, A. Memedi, S. Kruse, C. Kress, C. Scheytt, and F. Dressler, "An IEEE 802.11 Compliant SDR-based System for Vehicular Visible Light Communications," in *IEEE ICC 2019*, Shanghai, China: IEEE, May 2019.

[117] M. Segata, R. Lo Cigno, H.-M. Tsai, and F. Dressler, "On Platooning Control using IEEE 802.11p in Conjunction with Visible Light Communications," in *12th IEEE/IFIP Conference on Wireless On demand Network Systems and Services (WONS 2016)*, Cortina d'Ampezzo, Italy: IEEE, Jan. 2016, pp. 124–127.

[118] M. Schettler, A. Memedi, and F. Dressler, "Deeply Integrating Visible Light and Radio Communication for Ultra-High Reliable Platooning," in *IEEE/IFIP WONS 2019*, Wengen, Switzerland: IEEE, Jan. 2019, pp. 36–43.

[119] C. Tebruegge, A. Memedi, and F. Dressler, "Reduced Multiuser-Interference for Vehicular VLC using SDMA and Matrix Headlights," in *IEEE Global Communications Conference (GLOBECOM 2019)*, Waikoloa, HI: IEEE, Dec. 2019.

[120] S. Ucar, S. C. Ergen, and O. Ozkasap, "IEEE 802.11p and Visible Light Hybrid Communication based Secure Autonomous Platoon," *IEEE Transactions on Vehicular Technology (TVT)*, vol. 67, no. 9, pp. 8667–8681, Sep. 2018.

[121] B. Turan, G. Gurbilek, A. Uyrus, and S. C. Ergen, "Vehicular VLC Frequency Domain Channel Sounding and Characterization," in *10th IEEE Vehicular Networking Conference (VNC 2018)*, Taipei, Taiwan: IEEE, Dec. 2018.

[122] J. Koepe, C. Kaltschmidt, M. Illian, R. Puknat, P. Kneuper, S. Wittemeier, A. Memedi, C. Tebruegge, M. S. Amjad, S. Kruse, et al., "First Performance Insights on Our Novel OFDM-based Vehicular VLC Prototype," in *10th IEEE Vehicular Networking Conference (VNC 2018), Poster Session*, Taipei, Taiwan: IEEE, Dec. 2018.

[123] O. Narmanlioglu, B. Turan, S. Coleri Ergen, and M. Uysal, "Cooperative MIMO-OFDM based inter-vehicular visible light communication using brake lights," *Elsevier Computer Communications*, vol. 120, no. C, pp. 138–146, May 2018.

[124] S. Kruse, C. Kress, A. Memedi, C. Tebruegge, M. S. Amjad, C. Scheytt, and F. Dressler, "Design of an Automotive Visible Light Communications Link using an Off-The-Shelf LED Headlight," in *16th GMM/ITG-Symposium ANALOG 2018*, Munich, Germany: VDE, Sep. 2018.

[125] C. G. Gavrincea, J. Baranda, and P. Henarejos, "Rapid prototyping of standard-compliant visible light communications system," *IEEE Communications Magazine*, vol. 52, no. 7, pp. 80–87, Jul. 2014.

[126] W.-H. Shen and H.-M. Tsai, "Testing Vehicle-to-Vehicle Visible Light Communications in Real-World Driving Scenarios," in *9th IEEE Vehicular Networking Conference (VNC 2017)*, Turin, Italy: IEEE, Nov. 2017, pp. 187–194.

[127] B. Béchadergue, W.-H. Shen, and H.-M. Tsai, "Comparison of OFDM and OOK modulations for vehicle-to-vehicle visible light communication in real-world driving scenarios," *Elsevier Ad Hoc Networks*, vol. 94, Nov. 2019.

[128] "IEEE Standard for Local and metropolitan area networks – Part 15.7: Short-Range Wireless Optical Communication Using Visible Light," IEEE, Std 802.15.7-2011, Sep. 2011.

[129] N. Kumar, N. Lourenço, D. Terra, L. N. Alves, and R. L. Aguiar, "Visible Light Communications in Intelligent Transportation Systems," in *IEEE Intelligent Vehicles Symposium (IV 2012)*, Alcalá de Henares, Spain: IEEE, Jun. 2012.

[130] C. Tebruegge, Q. Zhang, and F. Dressler, "Optical Interference Reduction with Spatial Filtering Receiver for Vehicular Visible Light Communication," in *22nd IEEE International Conference on Intelligent Transportation Systems (ITSC 2019)*, Auckland, New Zealand: IEEE, Oct. 2019.

[131] Y. Wang, L. Tao, X. Huang, J. Shi, and N. Chi, "8-Gb/s RGBY LED-Based WDM VLC System Employing High-Order CAP Modulation and Hybrid Post Equalizer," *IEEE Photonics Journal*, vol. 7, no. 6, Oct. 2015.

[132] A. Tsiatmas, F. M. J. Willems, and S. Baggen, "Optimum diversity combining techniques for visible light communication systems," in *IEEE Global Telecommunications Conference (GLOBECOM 2014), 5th IEEE Workshop on Optical Wireless Communications (OWC 2014)*, Austin, TX: IEEE, Dec. 2014.

[133] M. Nabeel, B. Bloessl, and F. Dressler, "Efficient Receive Diversity in Distributed Sensor Networks using Selective Sample Forwarding," *IEEE Transactions on Green Communications and Networking*, vol. 2, no. 2, pp. 336–345, Jun. 2018.

[134] A. M. Wahbeh, J. P. Caffrey, and S. F. Masri, "A vision-based approach for the direct measurement of displacements in vibrating systems," *Smart materials and structures*, vol. 12, no. 5, p. 785, 2003.

[135] A. Khademi, F. Raji, and M. Sadeghi, "IoT Enabled Vibration Monitoring Toward Smart Maintenance," in *2019 3rd International Conference on Internet of Things and Applications (IoT)*, IEEE, 2019, pp. 1–6.

[136] L. Da Xu, W. He, and S. Li, "Internet of things in industries: A survey," *IEEE Transactions on Industrial Informatics*, vol. 10, no. 4, pp. 2233–2243, Nov. 2014.

[137] J. Chilo, C. Karlsson, P. Angskog, and P. Stenumgaard, "EMI disruptive effect on wireless industrial communication systems in a paper plant," in *IEEE EMC 2009*, Austin, TX, Oct. 2009, pp. 221–224.

[138] L. Wan, G. Han, L. Shu, S. Chan, and N. Feng, "PD source diagnosis and localization in industrial high-voltage insulation system via multimodal joint sparse representation," *IEEE Transactions on Industrial Electronics*, vol. 63, no. 4, pp. 2506–2516, 2016.

[139] P. Castellini, M. Martarelli, and E. Tomasini, "Laser Doppler Vibrometry: Development of advanced solutions answering to technology's needs," *Elsevier, Laser Doppler Vibrometry*, pp. 1265–1285, 2006.

[140] M. Martarelli and G. Revel, "Laser Doppler vibrometry and near-field acoustic holography: Different approaches for surface velocity distribution measurements," *Mechanical systems and signal processing*, vol. 20, no. 6, pp. 1312–1321, 2006.

[141] J. G. Chen, N. Wadhwa, Y.-J. Cha, F. Durand, W. T. Freeman, and O. Buyukozturk, "Structural modal identification through high speed camera video: Motion magnification," in *IMAC 2012*, Brescia, Italy: Springer, Jul. 2012, pp. 191–197.

[142] K.-S. Son, H.-S. Jeon, J.-H. Park, and J. W. Park, "A technique for measuring vibration displacement using camera image," *Transactions of the Korean Society for Noise and Vibration Engineering*, vol. 23, no. 9, pp. 789–796, 2013.

[143] T. Komine and M. Nakagawa, "Fundamental analysis for visible-light communication system using LED lights," *IEEE transactions on Consumer Electronics*, vol. 50, no. 1, pp. 100–107, 2004.

[144] J.-B. Wang, Q.-S. Hu, J. Wang, M. Chen, and J.-Y. Wang, "Tight bounds on channel capacity for dimmable visible light communications," *Journal of Lightwave Technology*, vol. 31, no. 23, pp. 3771–3779, 2013.

[145] C. Li, Y. Yi, and K. Lee, "Pilot self-coding applied in optical OFDM systems," *International Journal of Electronics*, vol. 102, no. 4, pp. 548–562, 2015.

[146] A. M. Khalid, G. Cossu, R. Corsini, P. Choudhury, and E. Ciaramella, "1-Gb/s Transmission Over a Phosphorescent White LED by Using Rate-Adaptive Discrete Multitone Modulation," *IEEE Photonics Journal*, vol. 4, no. 5, pp. 1465–1473, Oct. 2012.

[147] Z. Tian, K. Wright, and X. Zhou, "The DarkLight Rises: Visible Light Communication in the Dark," in *ACM MobiCom 2016*, New York City, NY: ACM, Oct. 2016.

[148] D. Chen, J. Wang, H. Lu, L. Feng, and J. Jin, "New Construction of OVSF-OZCZ Codes in Multi-Rate Quasi-Synchronous CDMA VLC Systems for IoT Applications," *IEEE Access*, vol. 8, pp. 130 888–130 895, Jan. 2020.

[149] H. Yang, W.-D. Zhong, C. Chen, and A. Alphones, "Integration of Visible Light Communication and Positioning within 5G Networks for Internet of Things," *IEEE Network*, vol. 34, no. 5, pp. 134–140, Sep. 2020.

[150] A. Veeraraghavan, D. Reddy, and R. Raskar, "Coded strobing photography: Compressive sensing of high speed periodic videos," *IEEE Transactions on Pattern Analysis and Machine Intelligence*, vol. 33, no. 4, pp. 671–686, 2010.

[151] A. Al-Kinani, C.-X. Wang, L. Zhou, and W. Zhang, "Optical wireless communication channel measurements and models," *IEEE Communications Surveys and Tutorials*, pp. 1939–1962, 2018.

[152] H. Henniger and O. Wilfert, "An Introduction to Free-space Optical Communications.," *Radioengineering*, vol. 19, no. 2, 2010.

[153] K. Mueller and M. Müller, "Timing Recovery in Digital Synchronous Data Receivers," *IEEE Transactions on Communications*, vol. 24, no. 5, pp. 516–531, May 1976.

[154] B. Bloessl and F. Dressler, "mSync: Physical Layer Frame Synchronization Without Preamble Symbols," *IEEE Transactions on Mobile Computing*, 2018, available online: http://dx.doi.org/10.1109/TMC.2018.2808968.

[155] M. Nabeel, M. S. Amjad, and F. Dressler, "Preamble-Less Diversity Combining: Improved Energy-Efficiency in Sensor Networks," in *IEEE Global Communications Conference (GLOBECOM 2018)*, Abu Dhabi, United Arab Emirates: IEEE, Dec. 2018.

[156] M. S. Amjad and F. Dressler, "Integrated Communications and Non-Invasive Vibrations Sensing using Strobing Light," in *IEEE ICC 2020*, Virtual Conference: IEEE, Jun. 2020.

[157] C. Tebruegge, A. Memedi, and F. Dressler, "Empirical Characterization of the NLOS Component for Vehicular Visible Light Communication," in *IEEE VNC 2019*, Los Angeles, CA: IEEE, Dec. 2019.